Article / Book Information

( )	
Title(English)	Development of porous carbon electrode for Li-air battery fabricated from supercritical carbon dioxide technique
( )	
Author(English)	Nattanai Kunanusont
( )	: ( ), : , : 11479 , :2020 3 26 , : , : , , , ,
Citation(English)	Degree:Doctor (Engineering), Conferring organization: Tokyo Institute of Technology, Report number: 11479 , Conferred date:2020/3/26, Degree Type:Course doctor, Examiner:,,,,
( )	
Type(English)	Doctoral Thesis
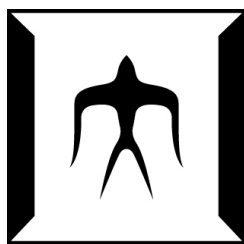
DEVELOPMENT OF
POROUS CARBON ELECTRODE
FOR LI-AIR BATTERY FABRICATED FROM
SUPERCRITICAL CARBON DIOXIDE TECHNIQUE

NATTANAI KUNANUSONT

Content

Chapter 1

Introduction

1.1 Background and motivation

Our world has now been facing many problems due to the great increment of population. One of the main problems we are now facing is energy problem caused by high demand of energy for large population. Fossil fuel is the main energy source that has been employed since 19th century. However, fossil fuel deals great impact on environment since it releases greenhouse gases like carbon dioxide after combustion process. The greenhouse gases can be the pollutant for human and simultaneously be the cause of global warming. The new sources of energy which emit zero greenhouse gas such as wind turbine, solar energy, water energy, thermal energy, biofuel and fuel cell have been developed to replace conventional oil-based energy. Those development of renewable energy urges us to improve such the high capacity energy storage. Until now, Lithium ion battery is the energy storage that has been widely applied in electrical devices. However, the capacity of state-of-the-art lithium ion battery is limited to only approximately 400 Wh kg^{-1} while the practical energy density for gasoline is 13,000 Wh kg^{-1} [1]. This implies that new energy storage with energy density much higher than today's state-of-the-art lithium ion battery is demanded to enable electric automotive vehicle. Here, Li-air battery has theoretical energy density of 11,680 Wh kg^{-1} is considered as one of the energy storages that can be replaced Li-ion battery [2]. This high value energy density is comparable to energy density of fossil fuel.

Although Li-air battery has high theoretical energy density, however, problems in practical process limit the energy density and cyclability of Li-air battery, making it unavailable for real application [3,4]. Those problems are from many prospects including dendrite in anode, decomposition of electrolyte, accumulation of discharge products in cathode, side reaction from humidity or contamination in reaction gases. Accordingly, Li-air battery is still under development to make it available and compatible comparing to Li-ion battery. Focusing on the problems in cathode, the main problem is considered on non-reactive and non-soluble lithium oxides formed on surface of cathode material which blocks the pore of the electrode and terminates the discharge reaction. Accordingly, the

high pore volume and high surface area materials for cathode with function for oxygen transportation and oxidation product storage is mainly on the research to improve performance of battery [5]. Most research have fabricated cathode by dispersing high surface area carbon material and dissolving polymer binder inorganic solvent. The solution is casted on casting material such as carbon paper or copper foam prior to drying by vacuum drying or evaporation. However, this fabrication method has three main drawbacks. Firstly, conventional vacuum drying or evaporation causes aggregation of carbon particle after solvent elimination. This reduces pore size and pore volume of cathode, limiting transportation of reaction gas and accumulation of discharge product [6]. Secondly, casting materials could cause side reaction in cathode hence discharge reaction is uncontrollable [7]. Thirdly, normal polymer binder has low conductivity for both electron and ion, void area for electrochemical reaction in cathode. Therefore, the cathode which has high porosity and free of casting material with new type of polymer binder should be developed to improve performance of Li-air battery.

Supercritical drying method can avoid pore collapse during solvent removal process because it has extremely low surface tension and no liquid-vapor interface [8,9]. Supercritical carbon dioxide (sc-CO_2) is mostly applied as supercritical fluid due to its convenient critical point, low cost, non-toxic, safety, environmentally friendly [10]. sc-CO_2 can be applied in drying of carbon dispersed organic solution because it has high affinity with non-polar compound. After it forms homogeneous phase with organic compounds, structure of carbon material can be preserved because sc-CO_2 forms homogeneous phase with organic compound. The carbon material after sc-CO_2 drying has large porosity which can be applied as cathode of Li-air battery to enhance transportation of reaction gas and accumulation of discharge product. Besides the benefit of sc-CO_2 for drying, it can impregnate ionic liquid (IL) into polymer because of polymer swelling and reduction of ionic liquid viscosity under sc-CO_2 atmosphere [11, 12]. This polymer-IL can be applied as binder between carbon particles in cathode structure, enhancing lithium ion and gas diffusion inside cathode. According to above reasons, sc-CO_2 can be applied to improve properties of cathode for Li-air battery. This development could be one of the solutions to reduce greenhouse gases emission by fossil fuel. The schematic diagram explaining advantages of sc-CO_2 on fabrication of cathode of Li-air battery is illustrated in Figure 1.1.
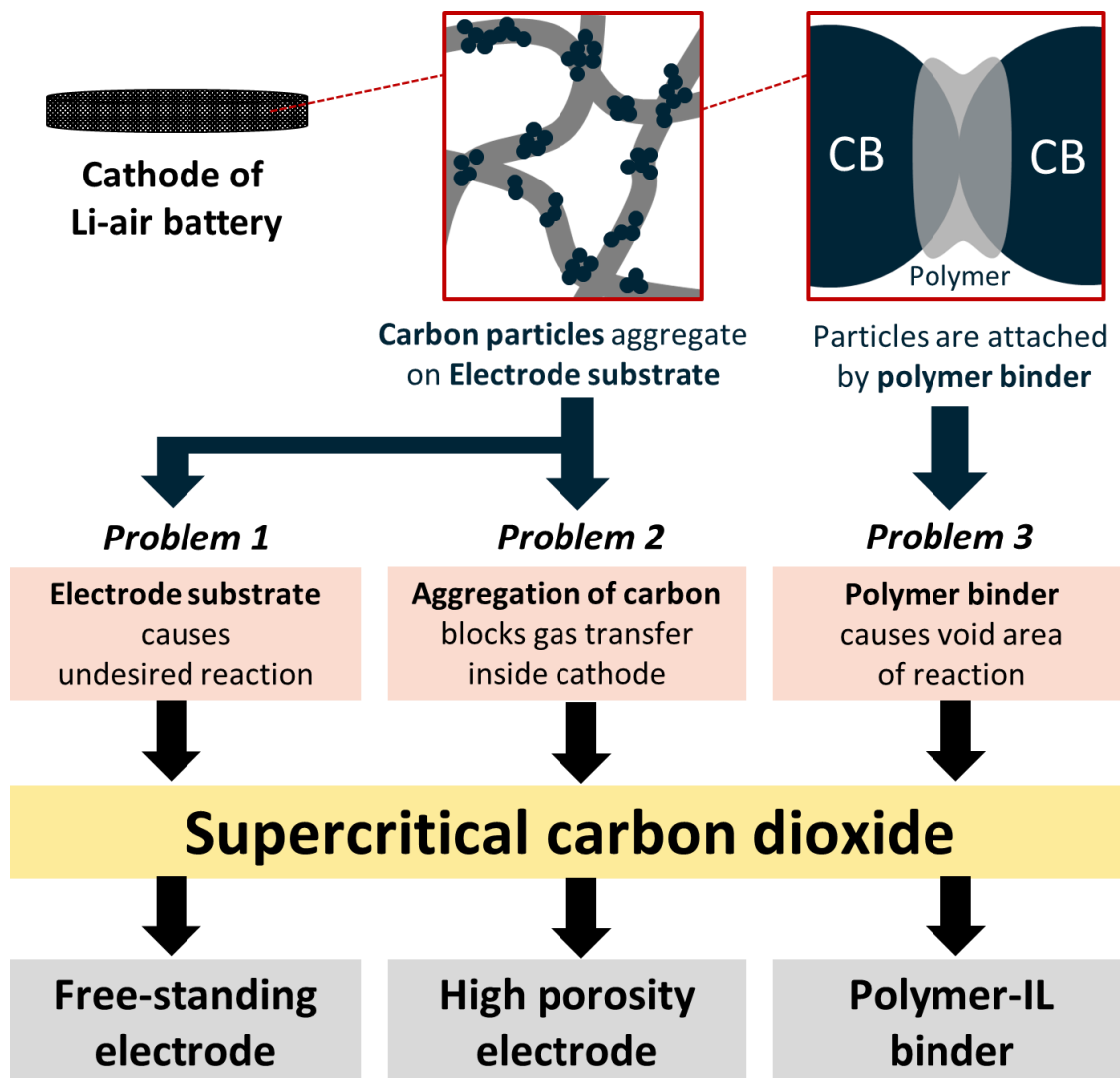
Figure 1.1 Advantages of sc-CO$_2$ on fabrication of cathode of Li-air battery.

1.2 Objective of this research

The aim to achieve in this research are stated as follows:

- Understanding of phase behavior on the phase inversion and drying using sc-CO_2
- Applying and investigating porous carbon cathode fabricated by sc-CO_2 fluid for development of Li-air battery.
- Applying and investigating ionic liquid in polymer binder of carbon porous cathode fabricated by sc-CO_2 fluid for development of Li-O_2/CO_2 battery
- Developing functionalized cathode fabricated by sc-CO_2 fluid for rechargeable Li-O_2 battery.

1.3 Literature reviews

The review of literatures in this work is dedicated to the research of Li-air battery in order to understand the previous studies and know the prospect of problems. Moreover, fabrication of porous materials from sc-CO_2 technique is reviewed as the method for fabrication of porous carbon electrode in Li-air battery.

1.3.1 Li-air battery

Lithium air battery is one type of metal-air battery that composed of lithium as the anode, electrolyte and porous material as the cathode. Its theoretical capacity based on weight of lithium anode can be calculated up to approximately 11,000 Wh kg^{-1}, which is comparable to energy density of gasoline and extremely higher capacity than normal lithium-ion battery. Lithium air battery can be divided into 4 main different architectures, which are aprotic type, aqueous type, solid state type and mixed aqueous/aprotic type [2]. Aqueous and mixed type has the advantages that discharge reaction is in water, prevent cathode from clogging and volume expansion. However, the challenge of these two types is the development of membrane to protect anode from vigorous reaction with water. The solid-state Li-air battery uses polymer-ceramic composites electrolyte to separate anode and cathode. Advantage of this type is that the solid electrolyte is its stability, non-flammability and non-leakage [13,14]. Nevertheless, the limit of this type is comparatively low ionic conductivity. Aprotic type of Li-air battery has been mostly focused and developed by many researched because of its rechargeability and high capacity. Accordingly, the main review of literatures in this chapter is focused on aprotic

type Li-air battery. Schematic of Li-air battery structure can be seen in Figure 1.2. The concept of lithium air battery was proposed in 1970s as novel power source for electric vehicles. This concept is based on the oxidation of lithium in anode side and reduction of oxygen at cathode side while lithium ion transfer between cathode and anode among electrolyte. electricity can be discharged and charged by flow of current thanks to the electrochemical reaction. However, the risks of reactive lithium and oxygen limited this technology to be practically applied and find the market demands. The first research of lithium-air battery was reported in 1996 by Abraham and Jiang, who applied polymer electrolyte in rechargeable lithium-oxygen battery [15]. Pure oxygen has been many researches have been further conducted due to the success and possibility of lithium-air battery. Nonetheless, there are many problems limited lithium air battery to reach its theoretical capacity and rechargeability comparable to lithium-ion battery. Initially, the main product after discharge, Li_2O_2, is non-conductive and non-soluble. This product is accumulated in cathode and blocks transfer of oxygen hence further electrochemical reaction is voided due to inaccessible oxygen. Moreover, the side reactions such are possibly occurred because oxygen has high reactivity. The electrochemical reaction between lithium ion with carbon dioxide and water in the air is possible, while decomposition of electrolyte is considerable. Lithium anode also has some problems due to the dendrite formation which limited the efficiency of the battery. Accordingly, research and developments of lithium-air battery has been conducted to solve those problems. The review of researches of lithium-air battery in this dissertation is divided into 5 prospects, cathodic compartment, effect of reaction gases and humidity, electrolyte, anodic compartment and battery design.
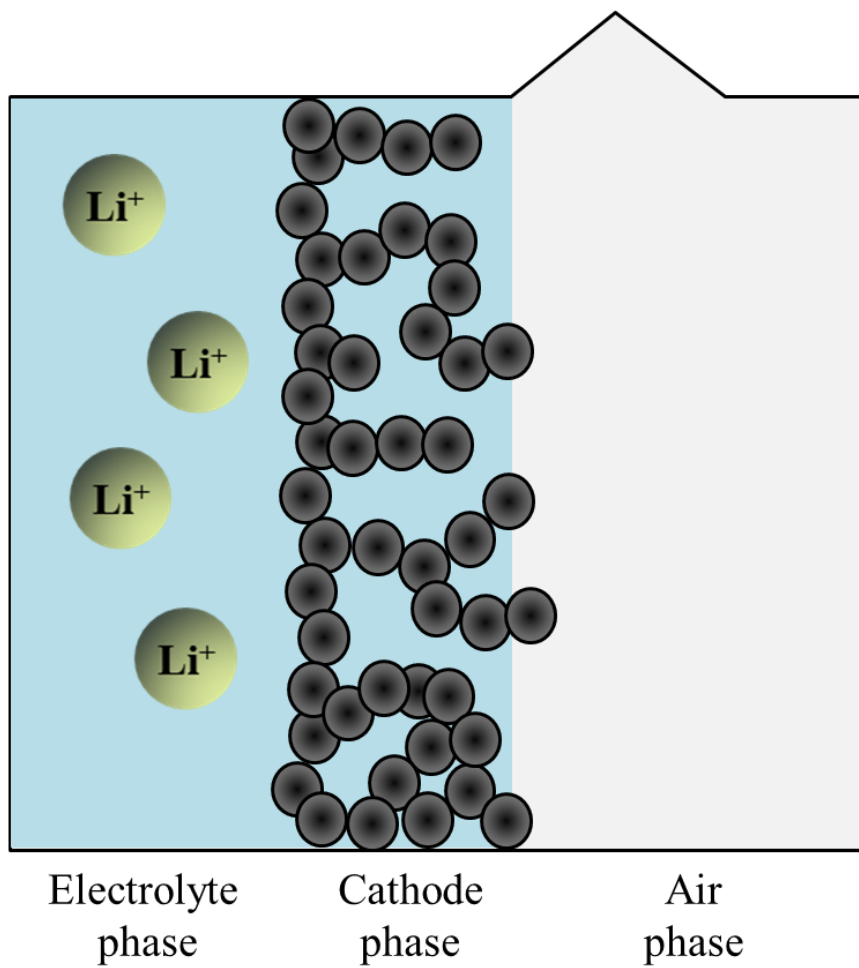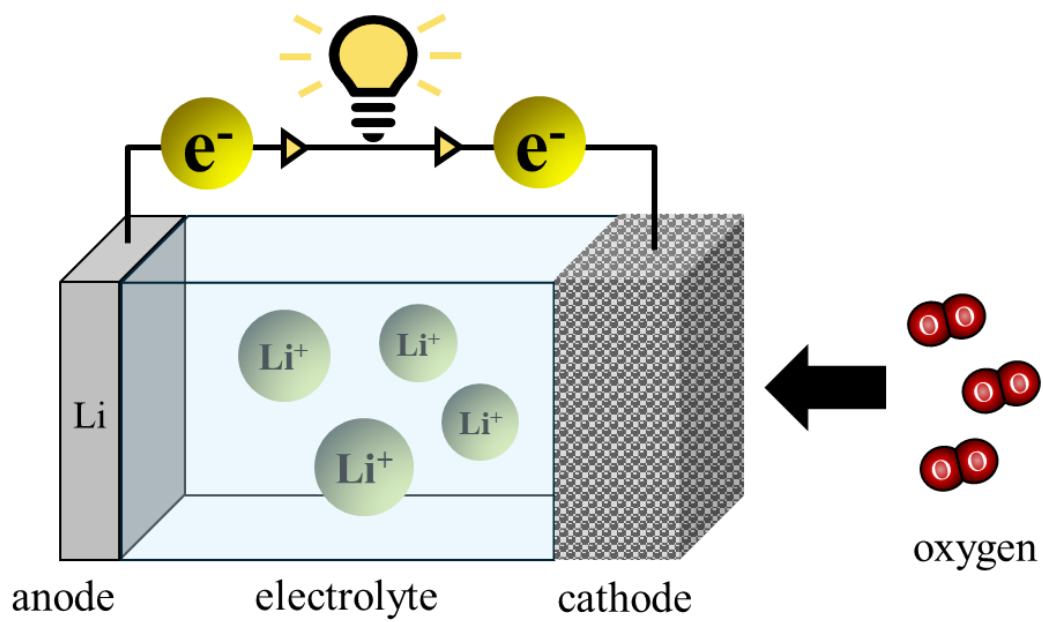
Figure 1.2 Schematic of aprotic Li-air battery structure.

1.3.1.1 Effect of reaction gases and humidity

Reaction gases and humidity are considered as one of the main prospects in designing lithium-air battery. Lithium-air battery was initially considered from the reduction of oxygen and lithium ion in the cathode, forming Li_2O_2 in the cathode. This battery is also called as lithium-oxygen battery (Li-O_2 battery). The electrochemical reaction in case of pure oxygen can be shown as follows [16],

Anodic reaction:	$Li \leftrightarrow Li^+ + e^-$	(1.1)
Cathodic reaction:	$Li^+ + O_2 + e^- \leftrightarrow LiO_2$	(1.2)
	$2LiO_2 \leftrightarrow Li_2O_2 + O_2$	(1.3)
	$LiO_2 + Li^+ + e^- \leftrightarrow Li_2O_2$	(1.4)
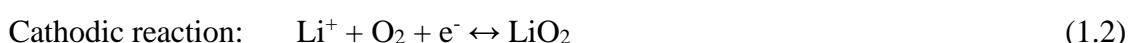
The cathodic reaction is occurred at around 2.91 V vs Li/Li^+. The reaction in cathode during discharge process can be called as oxygen reduction reaction (ORR), while reaction during charging process can be called as oxygen evolution reaction (OER). Most researches of lithium-air battery applied pure oxygen as the reaction gas to neglect the side reaction of other components in the air, such as carbon dioxide and water. However, the effect of those components cannot be neglect in the practical application.

The effect of carbon dioxide was initially introduced by research group of Takechi et al. from Toyota Central R&D Laboratories Inc [17]. They varied the gas volumetric ratio of oxygen and carbon dioxide as the reaction gases in Li-air battery. The full discharge profiles of battery in case of 30 to 70 % O_2/CO_2 ratio provide the highest discharge capacity at approximately 6750 mAh g^{-1}, which is more than 3 folds higher than full discharge capacity of battery with pure oxygen at 2000 mAh g^{-1}. This report enlightens the knowledge of lithium-air battery because carbon dioxide was previously considered as air contamination and could limit capacity of battery. Conversely, mixture of carbon dioxide and oxygen helps increase the capacity of battery rather than using only pure oxygen. The electrochemical reaction in case of O_2 and CO_2 reaction gases were proposed as follows,

Cathodic reaction: $4O_2 + 4e^- \leftrightarrow 4O_2^-$ (1.5)

$O_2^- + CO_2 \leftrightarrow CO_4^-$ (1.6)

$CO_4^- + CO_2 \leftrightarrow C_2O_6^-$ (1.7)

$C_2O_6^- + O_2^- \leftrightarrow C_2O_6^{2-} + O_2$ (1.8)

$C_2O_6^{2-} + 2O_2^- + 4Li^+ \leftrightarrow 2Li_2CO_3 + 2O_2$ (1.9)
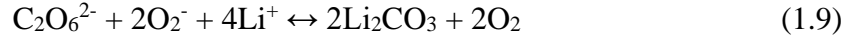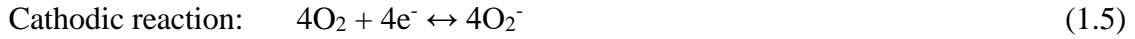
Takechi et al. explained the increment of capacity that $C_2O_6^-$ formed in reaction (1.7) is relatively stable in electrolyte, leading the Li_2CO_3 accumulation slower than formation of Li_2O_2 in lithium-oxygen battery. Due to slow accumulation, void volume of cathode is comparatively filled, resulting in enhancement of battery capacity. This lithium-oxygen and carbon dioxide battery ($Li-O_2/CO_2$ battery) broadens the utility of lithium air battery as carbon dioxide capture and utilization, which could be one of the applications to solve environmental and energy problems.

Although mixture of O_2 and CO_2 enhances the capacity than battery with pure O_2, Li-air battery used only pure CO_2 cannot be discharge according to report from Takechi et al. However, some research proposed that pure CO_2 can also be used as reaction gas in Li-air battery. This battery is called as lithium-carbon dioxide battery ($Li-CO_2$ battery). S. Xu et al. reported that $Li-CO_2$ battery could be discharged and provided 2000 mAh g^{-1} at 60 ℃ [18]. The electrochemical reaction mechanism was proposed by Yu Qiao et al. as follows [19],

Cathodic reaction: $4Li^+ + 3CO_2 + 4e^- \leftrightarrow 2Li_2CO_3 + C$ (1.10)

$4Li_+ + CO_2 + 4e^- \leftrightarrow 2Li_2O + C$ (1.11)
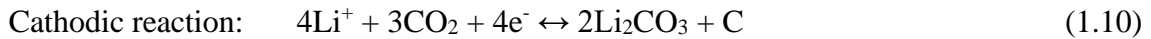
Reaction (1.10) occurs at 2.5 V vs. Li/Li+, while reaction (1.11) occurs at 1.8 V vs. Li/Li^+. In case of $Li-CO_2$ battery, amorphous carbon is accumulated in battery which cannot be decomposed in charging process unless some catalysts like RuO_2 is applied. Therefore, the development of catalyst is important to make $Li-CO_2$ battery practically.

Humidity in reaction gas can also affect the electrochemical reaction of Li-air battery. The possible reactions involving water in Li-air battery was proposed as follows [20],

Cathodic reaction: $2Li_2O_2 + 2H_2O \leftrightarrow 2LiOH + O_2$ (1.12)

$2LiOH + CO_2 \leftrightarrow Li_2CO_3 + H_2O$ (1.13)

The main discharge products by effect of humidity are LiOH and Li_2CO_3. Guo et al. reported that small amount of humidity at 15 % RH increased full discharge capacity of Li-O_2 battery, however, decreased cyclability performance comparing to Li-O_2 battery with dry and pure oxygen [21]. The increment of full discharge capacity contributed to high solubility of LiOH in electrolyte, reducing pore blocking at the cathode. However, LiOH cannot be decomposed hence cyclability of battery is comparatively poor.

1.3.1.2 Cathodic compartment

Since discharge process is occurred directly inside the porous structure of cathode, cathode compartment of Li-air battery has been widely researched to improve discharge capacity of battery. carbon materials have been applied as cathode for Lithium-air battery due to its light weight and high porosity. In aprotic Li-air battery with carbon cathode, the reaction site for oxygen is occurred on the interface of electrolyte-carbon [5] as illustrated in Figure 1.3. However, the discharge products such as lithium-oxide or lithium carbonate formed during discharge process are insoluble in organic electrolyte, therefore it is precipitated and covered the reaction side, simultaneously blocking gas transportation in cathode. As the results, capacity drops before reaching the theoretical value. Materials with large pore size considerably reduces problem of pore clogging, while materials with large pore volume helps the accumulation of discharge product. Moreover, surface area of materials also plays important role to support the reaction side during discharging and charging process.

Researches on cathodic compartments of Li-air battery are summarized in Table 1.1. Cathodes were mainly composed of carbon material as the active side for reaction, polymer as binder of carbon particles, some catalyst to promote ORR or OER and casting materials as the current collector. One-dimensional carbon materials such as carbon nanotube (CNT) [24, 29, 30, 34, 37] and carbon nanofiber (CNF) 27 were employed to promote pore volume of cathode. Two-dimensional carbon materials like graphene and graphene oxide [28, 33, 38] have gained attention due to its high surface area.
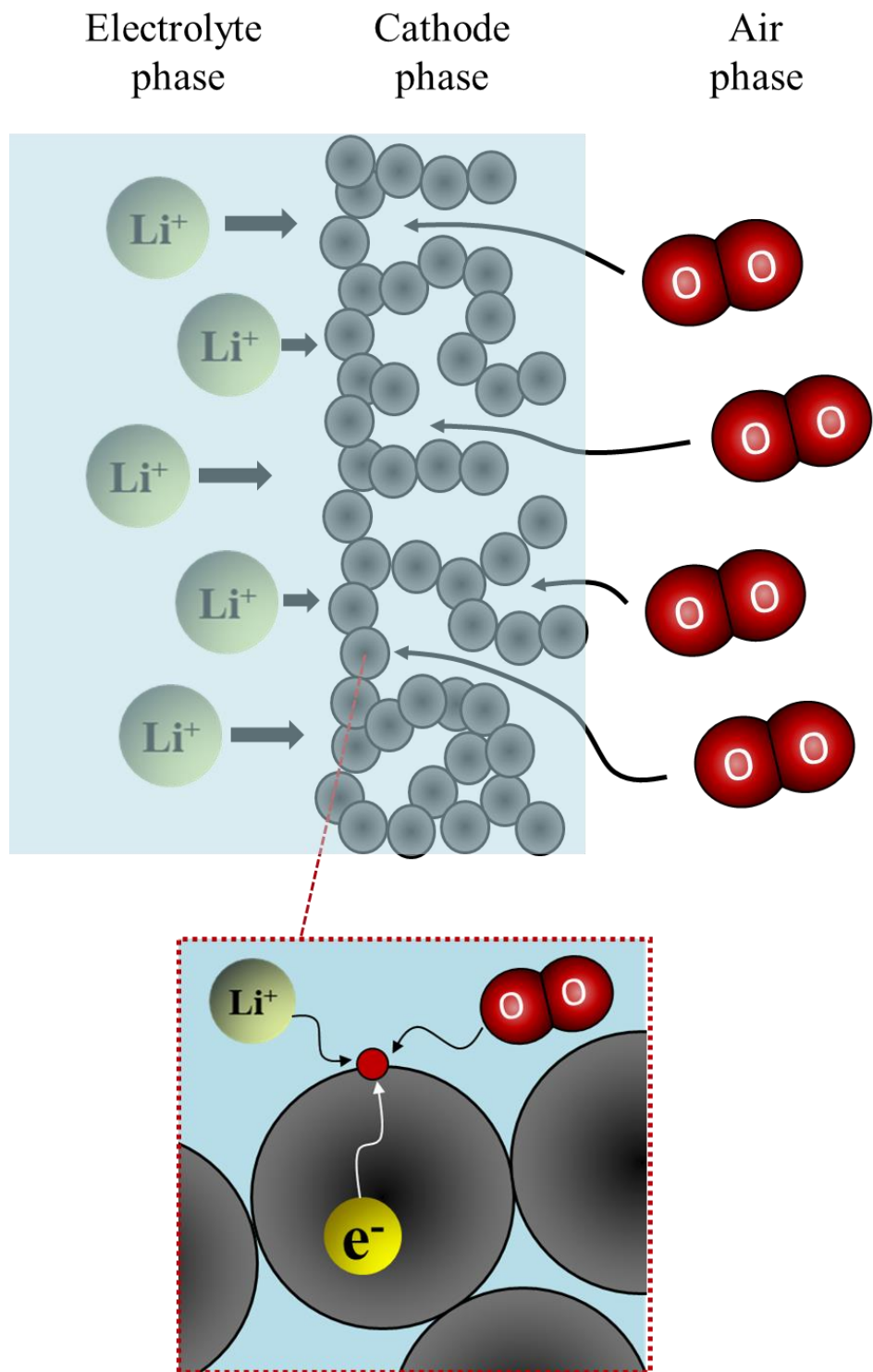
Figure 1.3 Schematic diagram of electrolyte-carbon interface in aprotic Li-air battery.

Table 1.1 Researches on cathode compartment of Li-air battery.

Cathode materials	Electrolyte	Fabrication methods	Reaction gas	Maximum capacity	Cycle number	Ref.
MCF-C/PTFE	1 M LiClO$_4$ in PC	Compressed and heated	O$_2$	2500 mAh g^{-1} at 0.1 mA cm^{-2}	N/A	[23]
Free-standing hierarchical porous CNT film	1 M LiPF6 in TEGDME	Annealing PS at 500°C	O$_2$	4683 mAh g^{-1} at 50 mA g^{-1}	40 cycles (500 mAh g^{-1})	[24]
R-F carbon aerogel/PVDF	1 M LiTFSI in sulfolane	Vacuum drying of slurry	O$_2$	12500 mAh g^{-1} at 0.1 mA cm^{-2}	112 cycles (1000 mAh g^{-1})	[25]
Carbon nano balls/PVDF	1 M LiClO$_4$ In EC/PC	Evaporation of slurry	O$_2$	3600 mAh g^{-1} at 0.1 mA	N/A	[26]
Co$_3$O$_4$/CNF composites	1 M LiCF$_3$SO$_3$ in TEGDME	Electrospunning, thermal treatments	O$_2$	760 mAh g^{-1} at 500 mA g^{-1}	20 cycles (2.3-4.5 V)	[27]
Graphene/PVDF	1 M LiTFSI in TEGDME	Slurry drying at 80°C	CO$_2$	15000 mAh g^{-1} at 50 mA g^{-1}	20 cycles (1000 mAh g^{-1})	[28]
Vertically aligned CNT grown on Ta foils	1 M LiTFSI in TEGDME	TVCD method	O$_2$	11500 mAh g^{-1} at 50 mA g^{-1}	> 60 cycles (1000 mAh g^{-1})	[29]
Well-align CNT arrays/CB/carbon paper	1 M LiTFSI in PC/EC	CVD method	O$_2$	2930 mAh g^{-1} at 50 mA g^{-1}	30 cycles (2.0-4.2 V)	[30]
Ru-graphene aerogel	LiCF$_3$SO$_3$ in TEGDME	Sc-CO$_2$ drying of hydrogel	O$_2$	12000 mAh g^{-1} at 500 mA g^{-1}	> 50 cycles (500 mAh g^{-1})	[31]
CB/P(TMA-MMA) gel polymer binder	0.5 M LiTFSI in DEGDME	Vacuum drying of slurry at 80°C	O$_2$	9200 mAh g^{-1} at 200 mA g^{-1}	> 100 cycles (500 mAh g^{-1})	[32]
PdSnCo/N-doped graphene/PVDF	1 M LiTFSI in TEGDME	Mixed and dried in vacuum oven	O$_2$	4200 mAh g^{-1} at 0.3 mA cm^{-2}	> 60 cycles (500 mAh g^{-1})	[33]
Free-standing 3D bimodal porous CNT film	1 M LiTFSI in TEGDME	Annealing PS at 450°C	O$_2$	5500 mAh g^{-1} at 500 mA g^{-1}	> 100 cycles (1000 mAh g^{-1})	[34]
Pd/Ultra-polar carbon/PVDF	1 M LiCF$_3$SO$_3$ in TEGDME	Vacuum drying of slurry at 120°C	O$_2$	N/A	231 cycles (1000 mAh g^{-1})	[35]
MoFeNi/MoC nanoparticle	1 M LiTFSI in TEGDME	FCCVD method	O$_2$	N/A	> 160 cycles (1000 mAh g^{-1})	[36]
MoFeNi/MoC nanoparticle	1 M LiTFSI in TEGDME	FCCVD method	CO$_2$	9000 mAh g^{-1} at 100 mA g^{-1}	> 90 cycles (1000 mAh g^{-1})	[36]
NiO-CNTs/PVDF	1 M LiTFSI in TEGDME	Slurry drying	CO$_2$	9000 mAh g^{-1} at 50 mA g^{-1}	> 42 cycles (1000 mAh g^{-1})	[37]
Cu/N-doped graphene/PVDF	1 M LiTFSI in TEGDME	Slurry drying at 80°C	CO$_2$	14864 mAh g^{-1} at 200 mA g^{-1}	50 cycles (1000 mAh g^{-1})	[38]
KB/PTFE	1 M LiCF$_3$SO$_3$ in TEGDME	Vacuum drying of slurry at 110°C	O$_2$/CO$_2$ (2:1)	1808 mAh g^{-1} at 30 mA g^{-1}	13 cycles (940 mAh g^{-1})	[39]
KB/PTFE	1 M LiCF$_3$SO$_3$ in TEGDME	Vacuum drying of slurry at 110°C	CO$_2$	1032 mAh g^{-1} at 30 mA g^{-1}	7 cycles (2.2 V)	[39]

However, three-dimensional materials such as ketjen black or carbon black [31, 32, 39] are considered as the good cathode materials which can provide good balancing of both benefits from one-dimension and two-dimension materials [22]. Polyvinylidene fluoride (PVDF) [25, 26, 28, 33, 35, 37, 38] and Polytetrafluoroethylene (PTFE) [23, 39] were the common polymer binder in cathode materials due to their good mechanical properties and inert to react with electrolyte or another solvent in large electrochemical windows. However, some researchers fabricated binder-free electrode [24, 27, 36] to avoid degradation of polymer binder during electrochemical reactions [40]. Precious metal and precious metal oxide such as Ru and RuO_2 [31] demonstrate overpotential reduction over charging process, supporting catalytic activity in OER. Moreover, Ru also known as the catalyst which can promote the charging reaction in Li-CO_2 battery [18]. Transition metal oxide like Co_3O_4 [27] and MnO_2 was also employed to promote the catalytic activity during Li_2O_2 decomposition [22].

As cathode fabrication methods, most researchers fabricated cathode of Li-air battery by mixing carbon nanoparticles, polymer binder and catalyst in organic solvent to form viscous slurry. The slurry was then casted on substrate and then dried by evaporation or vacuum drying at high temperature [25, 26, 28, 32, 35, 37-39]. However, surface tension due to evaporation or vacuum drying could be occurred, leading to pore collapsing of cathode structure. Some research groups applied another method to create more pore in cathode. Jiang et al. applied sc-CO_2 to fabricate Ru-graphene aerogel and used as cathode for Li-O_2 battery [31]. Liu et al. and Ren et al. annealed cathode with polystyrene at high temperature to decompose polystyrene, creating macro pore in cathode [24, 34]. Apart from creating pore in cathode, Zhang applied multi-functional gel in cathode to promote electrochemical reaction of discharge and charge in Li-O_2 battery [32]. This means that structure of cathode and fabrication method are the main keys to improve performance of Li-air battery.

1.3.1.3 Electrolyte

Electrolyte is one of the important compartments in Li-air battery because it is the medium for transportation of Li^+ ion and gases. Research of electrolyte is extremely important for designing aprotic Li-air battery. The necessary and fundamental function of electrolyte in Li-air battery is that it should be stable, non-toxic, non-flammable, non-volatile, low viscosity and have high ionic conductivity and ability to dissolve oxygen [41]. Moreover, good electrolyte for aprotic Li-air battery is expected to have high solubility of Li_2O_2 to improve charging process.

aprotic solvent in which lithium salts dissolved is employed as electrolyte in aprotic Li-air battery. Carbonate based electrolyte like ethylene carbonate and propylene carbonate is one of attractive aprotic solvent because of its high polarity and their low affinity to carbon. However, ether-based electrolytes such as tetraethylene glycol dimethyl ether (TEGDME) has better stability and less reactive against superoxide radical produced during charging and discharging process hence it is widely used as electrolyte for aprotic Li-air battery [22]. Jinqiang Zhang et. al. applied employ TEGDME in PVDF-co-HFP polymer to create gel polymer electrolytes for Li-air battery [42]. Dimethyl sulfoxide (DMSO) electrolyte is also widely employed due to its highest donor number (DN), promoting reduction of oxygen pathway comparing to another aprotic electrolytes [22].

Donor number or solvation of electrolyte also affects electrochemical pathway in $Li-O_2/CO_2$ battery. Lim et. al. stated that the dielectric constant of electrolyte mainly affects selectivity of reaction of Li^+ with either oxygen or CO_2 in case of pure dry air [43]. Li^+ is reacted with CO_4^- from reaction between O_2^- and CO_2 to form Li_2CO_3 in case of high dielectric constant solvent like DMSO. On the other hand, Li^+ is directly reacted with O_2^- to formed Li_2O_2 in electrolyte with low dielectric constant like dimethyl ether (DME). Since Li_2CO_3 is considered as more stable product than Li_2O_2, this advantage is extremely significant for designing product after discharge process. The schematic diagram explaining the effect of dielectric constant of electrolyte on electrochemical pathway is illustrated in Figure 1.4.
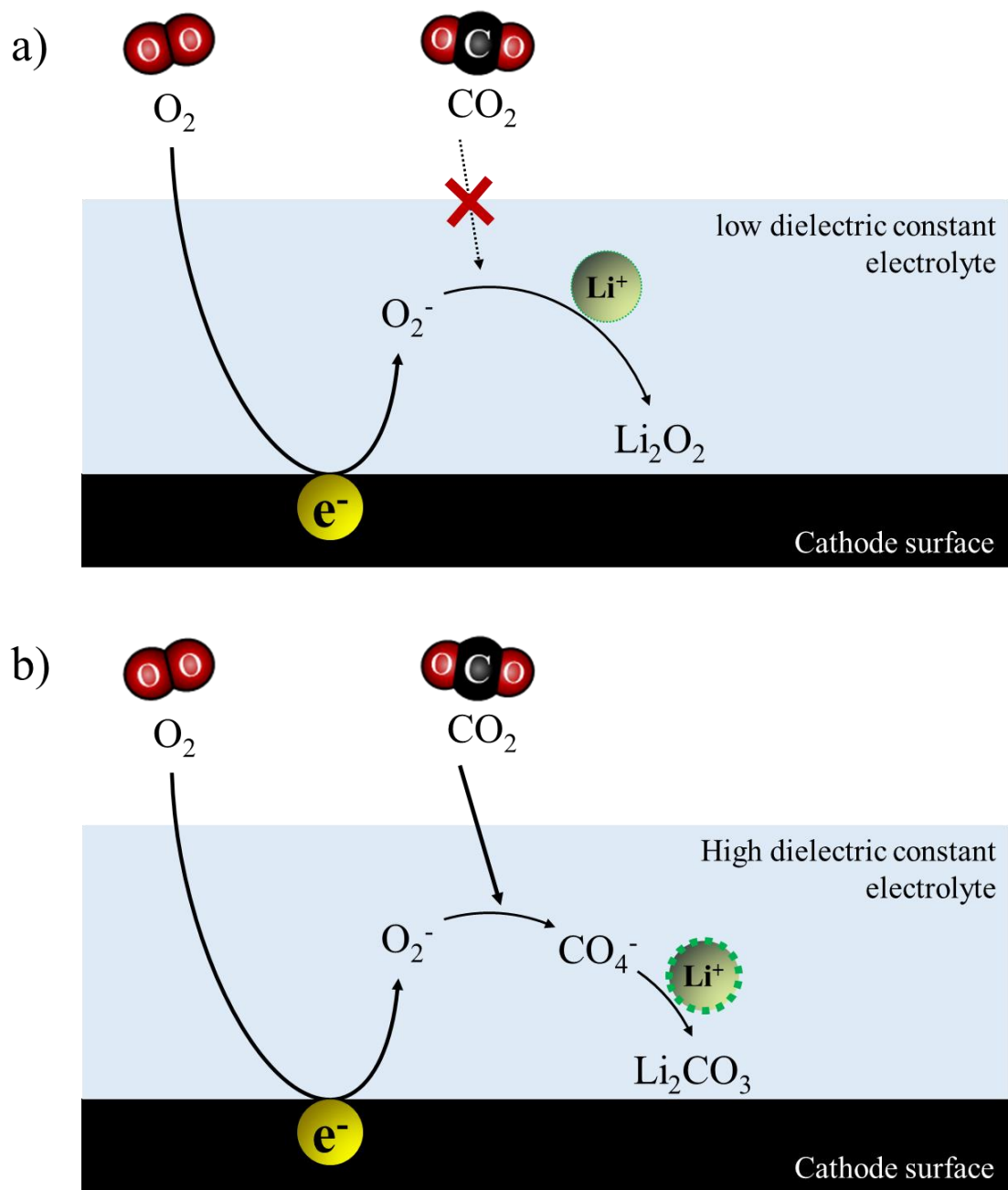
Figure 1.4 Electrochemical pathway of discharge mechanism in cathode of Li-O_2/CO_2 battery using a) electrolyte with low dielectric constant and b) electrolyte with high dielectric constant.

Room temperature ionic liquid (RTILs) is considered as one of the promising electrolytes for Li-air battery due to its hydrophobicity, non-volatile, high ionic conductivity [41]. The common IL electrolytes in Li-based battery are

imidazolium, quaternary ammonium, pyrrolidinium and piperidinium based cations, while PF_6^-, BF_4^- and $TFSI^-$ are commonly used as anions [41]. The Li-salt used in this electrolyte mostly is LITFSI. Here, Mahbuba Ara et. al. tested [bmim][Tf_2N] and [PYR_{14}][Tf_2N] electrolyte for Li-oxygen battery which is found that [bmim][Tf_2N] promises high capacity due to its high ionic conductivity (4 mS cm^{-1}) and low viscosity, while [PYR_{14}][Tf_2N] gives good cyclability from its stability [44].

It is clearly seen that type and properties of electrolyte is important for performance of Li-air battery. However, large overpotential due to sluggish kinetic of reduction of discharge product during charging process affects decomposition of electrolyte in high voltage, which limits cyclability of Li-air battery [22]. Recent researches applied some additives which can reduce charging overpotential, enhancing cyclability of battery. These additives also called as redox mediator (RM). The electrochemical pathway for decomposition of Li_2O_2 is stated as follows,

$$RM \leftrightarrow RM^+ + e^- \qquad (1.14)$$
$$RM^+ + Li_2O_2 \leftrightarrow 2Li^+ + O_2 + RM \qquad (1.15)$$

The mechanism of redox mediator is illustrated in Figure 1.5. This reaction starts from oxidation of redox mediator, followed by decomposition of Li_2O_2. Since redox mediator is soluble in electrolyte, decomposition of Li_2O_2 can be occurred on the contact between electrolyte and Li_2O_2. Hence, Li_2O_2 can be decomposed on contact surface between Li_2O_2 with electrolyte and between Li_2O_2 with cathode, reducing charging potential in OER. The recent researches on redox mediator are summarized in Table 1.2. Most researches added soluble redox mediator in lithium salt/electrolyte system to improve cyclability of Li-O_2 battery, simultaneously reduce potential during oxygen evolution reaction. These redox mediators could be halogen ion like iodide and bromide or some organic compound or organic compound with radical which can be oxidized. The advantages of redox mediator are expected for future development of rechargeable Li-air battery.
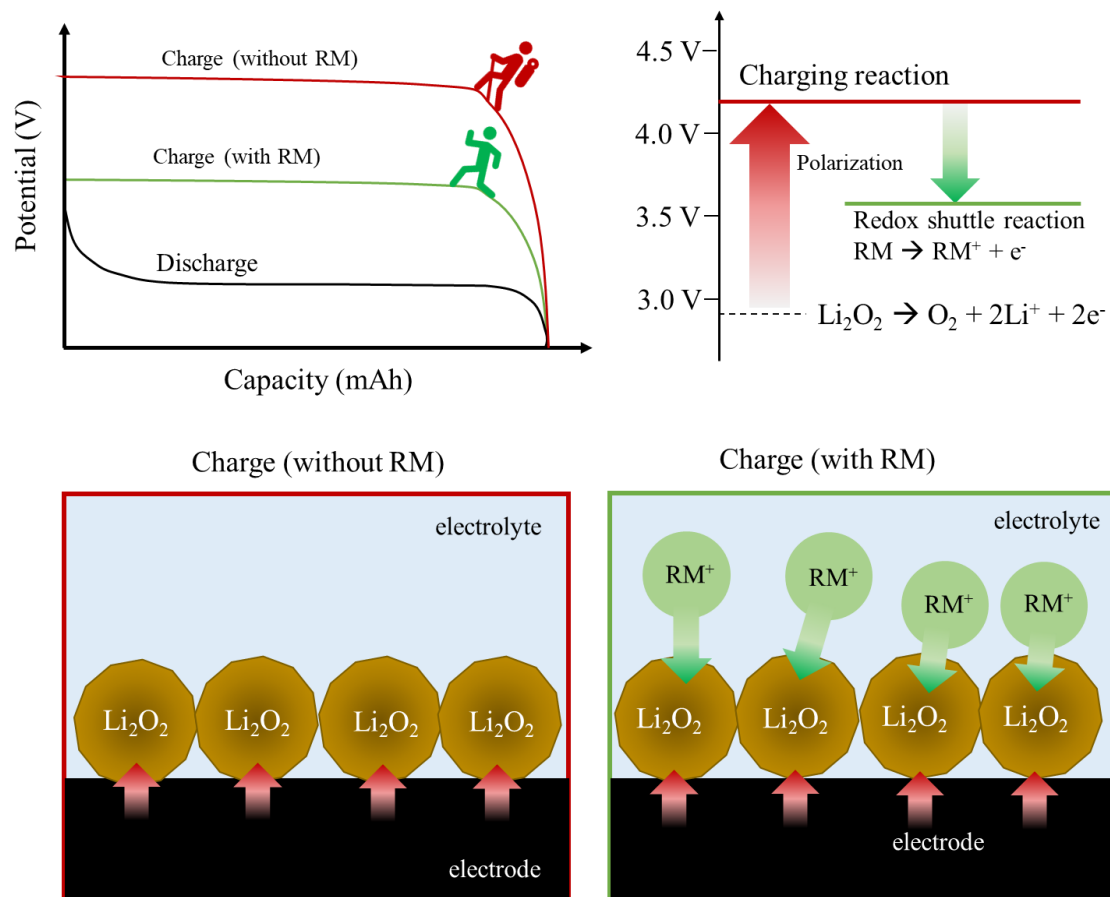
Charge (without RM)

Charge (with RM)

Discharge

Potential (V)

Capacity (mAh)

4.5 V

4.0 V

3.5 V

3.0 V

Charging reaction

Polarization

Redox shuttle reaction
$RM \rightarrow RM^+ + e^-$

$Li_2O_2 \rightarrow O_2 + 2Li^+ + 2e^-$

Charge (without RM)

electrolyte

Li_2O_2 Li_2O_2 Li_2O_2 Li_2O_2

electrode

Charge (with RM)

electrolyte

RM^+ RM^+ RM^+ RM^+

Li_2O_2 Li_2O_2 Li_2O_2 Li_2O_2

electrode

Figure 1.5 Mechanism of Li-O$_2$ battery charging with and without redox mediator.

Table 1.2 Summary of recent researches on redox mediator in Li-O_2 battery.

Redox mediator	Electrolyte	Cycle number	Ref.
iodide ion (I^-)	0.05 M LiI + 1 M LiTFSI in TEGDME	34 cycles (1000 mAh g^{-1})	[45]
Bromide ion (Br^-)	10 mM LiBr + 1 M LiTFSI in diglyme	15 cycles (500 mAh g^{-1})	[46]
Tetrathiafulvalene (TTF)	10 mM TTF + 1 M $LiClO_4$ in DMSO	100 cycles (300 mAh g^{-1})	[47]
Tris[4-(diethylamino)phenyl]amine (TDPA)	5 mM TDPA + 0.1 M LiTFSI in TEGDME	100 cycles (500 mAh g^{-1})	[48]
2,2,6,6-tetramethylpiperidinyloxyl (TEMPO)	10 mM TEMPO + 0.1 M LiTFSI in diglyme	50 cycles (500 mAh g^{-1})	[49]
N-methylphenothiazine (MPT)	0.1 M MPT + 1 M $LiCF_3SO_3$ in TEGDME	50 cycles (1000 mAh g^{-1})	[50]
Iron phthalocyanine (FePc)	2 mM FePc + 0.1 M LiTFSI in DMSO	135 cycles (1000 mAh g^{-1})	[51]
Tris{4-[2-(2-methoxyethoxy)ethoxy]phenyl}amine (TMPPA)	20 mM TMPPA + 1 M LiTFSI in TEGDME	100 cycles	[52]
1,2-dimethyl-3-(4-(2,2,6, 6-tetramethyl-1-oxyl-4-piperidoxyl)-pentyl)imidazolium bis(trifluoromethane) sulfonimide (IL-TEMPO)	50% IL-TEMPO + 0.5 M LiTFSI in TEGDME	50 cycles (0.25 mAh cm^{-2})	[53]

1.3.1.4 Anode compartment

Most researches of Li-air battery simply employed lithium metal foil as the anode. However, dendrite growth over lithium anode is one of the problems that limits performance of Li-air battery. Dendrite is the tree-like structure grown over surface of lithium metal. It can penetrate through electrolyte and lead to some side reactions which degrades the stability and safety of battery [54]. Dendrite growth could be occurred from many reasons such as oxygen crossover or attack from electrolyte [22]. There were some reports showing that attractive electrolytes like DMSO and TEGDME also cause dendrite formation from oxygen crossover and attack from electrolyte [55,56]. The penetrate of dendrite through electrolyte results in formation of LiOH which is irreversible to lithium metal.

The composite to substitute lithium metal or anode protection layer for dendrite formation have been researched to improve stability of Li-air battery. Silicon has been applied as composite in anode of Li-air battery due to its durability [57]. Research group of Haoshen Zhou reported that lithiated Si composite was able form strong solid electrolyte interphase (SEI) layer which can protect anode from attacking of electrolyte and providing long life of battery [58,59]. Besides the composite for substitution of lithium anode, composite protective layer (CPL) which can protect bare anode from electrolyte attack or crossover of oxygen was reported. Dong Jin Lee et al. demonstrated that CPL composite of Al_2O_3 and PVDF-HFP coated over lithium anode provided improvement of cyclability of $Li-O_2$ battery comparing to anode without coating of CPL 60. Zhang et al. showed simple way to form protective film layer over lithium anode via chemical reactions between Li metal and 1,4-dioxacyclohaxane [61].

1.3.1.5 Design of battery system

The selection and designing of cathode compartment, electrolyte and anode compartment are serious issues for development of Li-air battery. Good battery designing also could improve performance of battery apart from those main compartments. Pouch cell or coin cell have been applied as cell case in most research of Li-air battery. However, it is important to reduce unnecessary weight and optimize the design of cell structure, which could help achieve the greatest value of specific energy of battery. Jung O. Park et al. proposed cell structure of Li-air battery which provided 1000 Wh kg^{-1} specific energy

[62]. They design the battery by folding cathode, electrolyte and Li metal layer, resulting in weight reduction of battery and increase of contact area between each compartment.

Another way to design structure to optimize battery performance was conducted by macroscopic simulation of Li-air battery. There were many studies regarding to macroscopic modeling of Li-air battery [63,64]. Sergeev et al. revealed that porosity, thickness and carbon loading in cathode were responsible for capacity of battery [65]. They reported from simulation that cathode with larger porosity and less thickness provided better capacity. Furthermore, they also simulated that battery discharged with lower current density condition provided better capacity. This simulation results conformed with report from Zhang et al., who explained that battery discharged with low current density leads to formation of particle-like Li_2O_2 while film-like Li_2O_2 formed with high current density [32]. Besides the designing of cathode structure, Tan et al. [66] and Gwak et al. [67] revealed that amount of electrolyte in cathode also affect the performance of battery. They proposed the similar results that cathode wetted with electrolyte provided better performance than cathode flooded with electrolyte due to better transportation of reaction gases in void space occupying no electrolyte.

1.3.2 Supercritical fluids

Supercritical fluid is the substance at above its critical temperature and pressure where there is no distinction between vapor and liquid phases. Beyond this point, substance has high density and solubility like liquid, and low viscosity with high diffusivity like gas. The advantages from those properties have been used in many applications. Among supercritical fluid, supercritical carbon dioxide (sc-CO_2) has been the most widely used due to its low cost, stability, recyclability and simply approached critical point [68]. In this part, properties and application of sc-CO_2 has been reviewed as the method for porous carbon cathode fabrication in this work.

1.3.2.1 Supercritical carbon dioxide and its properties

Carbon dioxide has critical point at 31.1 °C and 73.8 bar, which is comparatively low comparing to another substances. Additionally, sc-CO_2 has low toxicity, environmental friendliness, non-flammability and high stability. It has density between

10^{-1} to 1 g cm^{-3}, diffusivity between 10^{-4} to 10^{-3} cm^2 s^{-1} like liquid and viscosity from 10^{-4} to 10^{-3} g cm^{-1} s^{-1} like gas [68]. Since carbon dioxide has low polarity, it can substitute some hazardous organic solvent in many processes. This attracts many applications to use sc-CO$_2$ as novel and green solvent. Density of sc-CO$_2$ can be varied by simply adjusting pressure and temperature condition as shown in Figure 1.6.

The conventional applications employing sc-CO$_2$ are extraction [68]. It can be used in extraction of bioactive compounds [69], decaffeination [70], extraction of emulsion [71] and of extraction of metal [72]. Sc-CO$_2$ has been further applied as media in production of nanomaterials due to its gas-like diffusivity. Those methods include rapid expansion of supercritical solutions (RESS), Supercritical anti-solvent precipitation (SAS), supercritical assisted atomization (SAA) and supercritical drying of sol/gel [73]. The researches on fabrication of porous materials by sc-CO$_2$ technique were reviewed since it was the main method for cathode fabrication in this work.

1.3.2.2 Fabrication of porous materials by supercritical carbon dioxide

The superior affinity of sc-CO$_2$ with hydrophobic organic solvent attracts many applications including sc-CO$_2$ drying. Sc-CO$_2$ drying has been applied widely in aerogel fabrication from sol-gel solution [73]. In atmospheric drying of sol/gel, liquid changes its phase to vapor while it comes across phase boundary. This causes surface tension which finally pulls the nanoparticles together, leading to the aggregation of gel structure. Sc-CO$_2$ fluid, on the other hand, forms homogeneous phase with organic solvent as one phase hence there is no phase-transition causing no surface tension. Therefore, the sol-gel dried from this method can preserve its structure after solvent elimination. The supercritical drying product of sol-gel is called "aerogel", while evaporation product of sol-gel is called "xerogel" [74]. The drying of sol-gel is illustrated in Figure 1.7. The sc-CO$_2$ drying has been used for fabrication of many porous media such as carbon aerogel and silica aerogel [75-80]. Those porous medias have been employed in various applications. This includes the fabrication of graphene aerogel as cathode materials for Li-O$_2$ battery reported by Jiang et al. [31]. The research of porous materials fabricated in sc-CO$_2$ fluid is listed in Table 1.3.
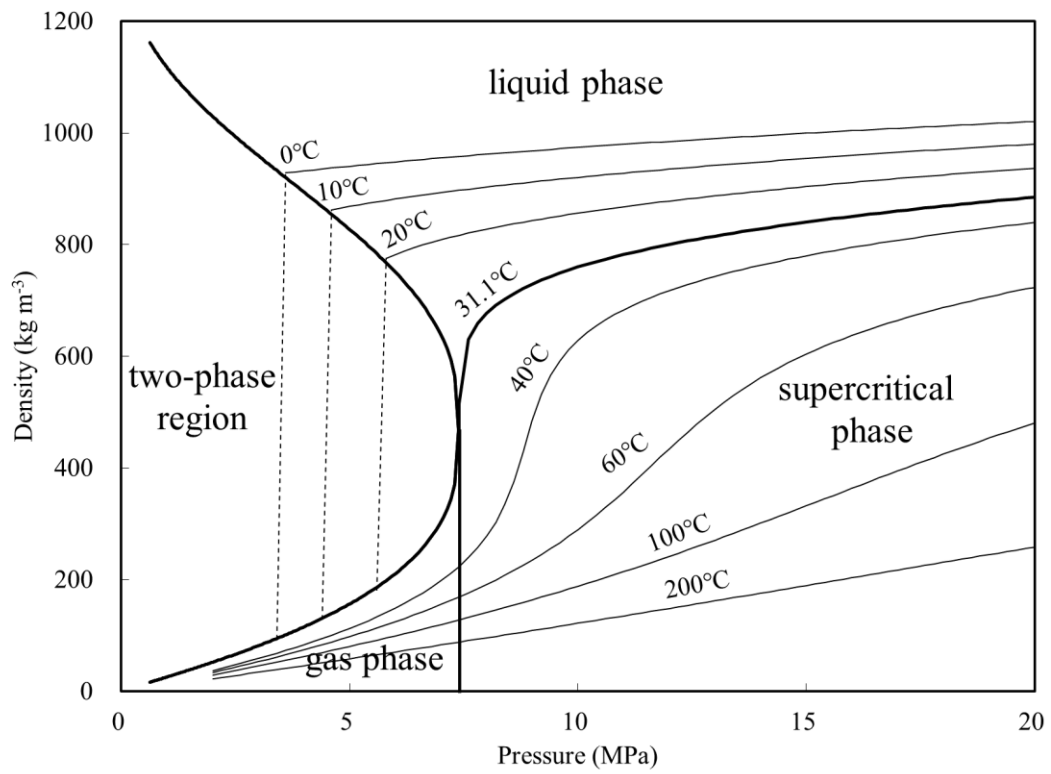
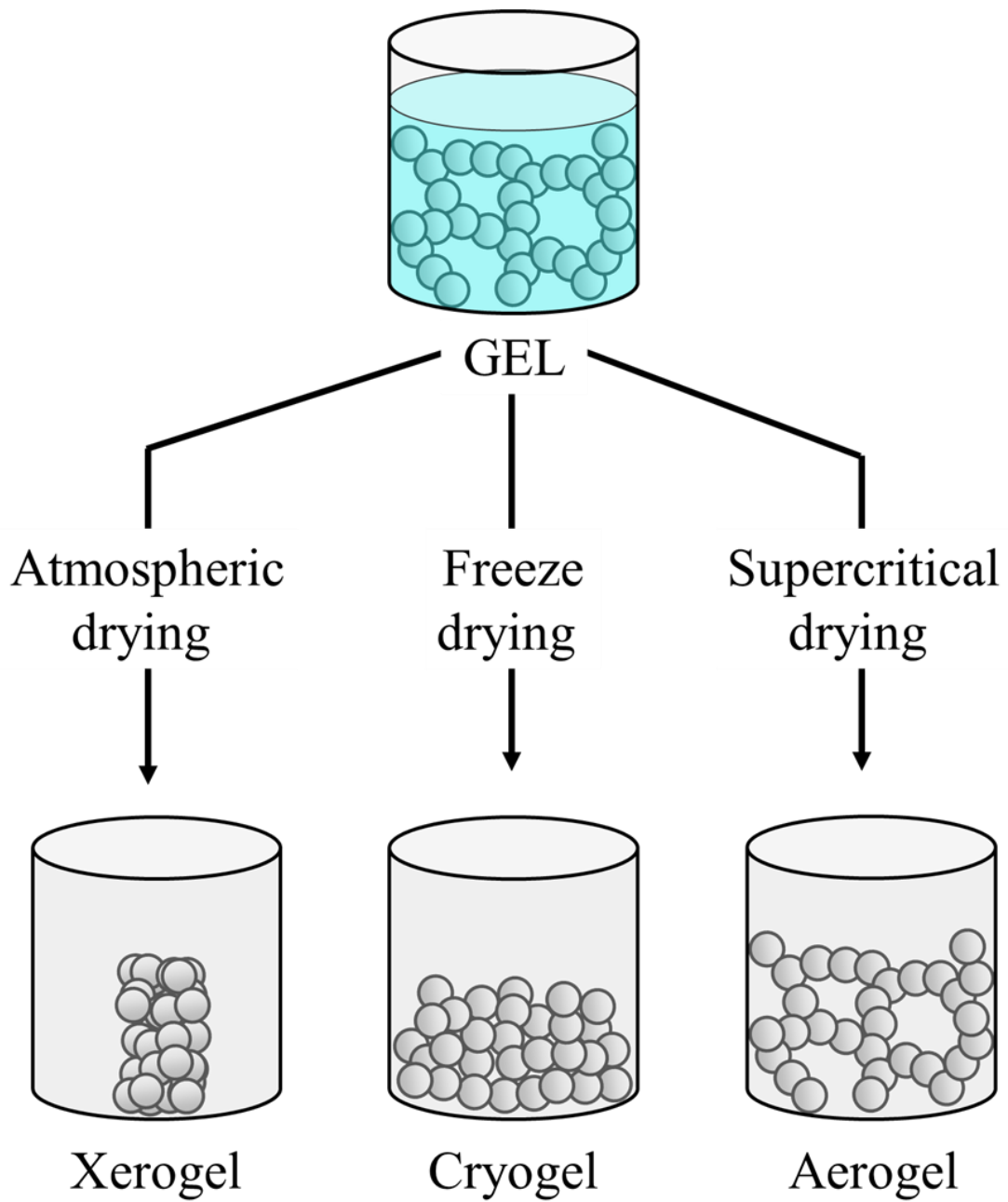Figure 1.6 Density of carbon dioxide as a function of pressure and temperature.

Figure 1.7 Schematic diagram of atmospheric drying, freeze drying and supercritical drying of sol-gel.

Table 1.3 Porous materials fabricated in supercritical carbon dioxide fluid.

Materials	Precursor solution	Sc-CO_2 condition	application	Ref.
Ru particle functionalized graphene aerogel	$RuCl_3$ and GO aqueous solution, washed with ethanol	N/A	Li-air battery	[31]
Titania aerogel	Ti precursor (TIP, TBO, TDB, TEO) in acetic acid	20.0 MPa 40 ℃	photocatalytist	[75]
Carbon aerogel	Resorcinol, Furfural in HMTA mixed in EtOH. Acetic acid was used as catalyst	9 MPa 70 ℃	Hydrogen storage	[76]
Large-area silica aerogel	Polymethoxy siloxane in aqueous ammonia solution. MeOH and DMF used as diluent solvent	15.7 MPa 40 ℃	Cherenkov radiator	[77]
Starch aerogel	Starch in aqueous solution. Ethanol used as co-solvent	100-200 bar 40-120 ℃	Food and pharmaceutical	[78]
Cellulose nanofibrils aerogel	Cellulose nanofibrils in ethanol/water solution	100 bar 45 ℃	Food, cosmetic and biomedical	[79]
Mesoglycan impregnated calcium alginate aerogel	Calcium alginate in aqueous solution exchanged solvent with ethanol.	20 MPa 35 ℃	Wound healing	[80]

Porous media can also be generated by foaming methods, which is normally microcellular polymer foams [80,82]. In this method, polymer is placed in supercritical fluid, forming cellular polymer by gas foaming. After rapid depressurization, supersaturation of polymer leads to the growing of nucleation, creating pore inside polymer matrix. Other methods to fabricate porous polymer media can be conducted by crystallization of swollen and crosslinked polymers [83]. This method starts from melting of polymer, followed by swelling of polymer in sc-CO_2 fluid. The further reduction of system temperature and pressure leads to crystallization of polymer and venting of supercritical fluid, resulting in the formation of porous polymer. Apart from those methods, Supercritical fluid antisolvent induced phase inversion can be used in fabrication of porous polymer [84]. In this method, polymer is initially dissolved in organic solvent, followed by phase-inversion between solution and non-solvent (sc-CO_2 in this case). Polymer is precipitated during phase inversion due to reduction of solubility, which finally forms porous media after depressurization.

It can be clearly seen that fabrication of porous media by sc-CO_2 fluid involves in the utilization of organic compounds such as the solvent in sol/gel solution or solvent of polymer solution. Until now, many data such as solubility of carbon dioxide in organic solvent [85,86] together with vapor-liquid equilibria [87] and mass transfer between carbon dioxide and organic solvent [88] have been investigated. These data are useful information, which leads us to understand the mechanism of phase behavior between sc-CO_2 fluid and organic solvent.

1.4 Contents of dissertation

Chapter 1 states the introduction of this research, including background, objective and literature review. The recent researches on development of Li-air battery on the viewpoint of effect of reaction gases and humidity, cathodic compartment, electrolyte, anode compartment and battery design together with the fabrication of porous materials by sc-CO_2 were reviewed.

Chapter 2 introduces the fundamental study of phase behavior observation in sc-CO_2. The phase behavior of pure organic compound and polymer dispersed solution, together with carbon particle and polymer dispersed solution in sc-CO_2 were studied.

Chapter 3 presents the fabrication of porous carbon electrode composite composed of carbon black and PVDF by sc-CO_2 fluid. Properties of porous carbon electrode composite fabricated from sc-CO_2 and evaporation are compared. The effect of sc-CO_2 pressure on the property of electrode is discussed. Porous carbon electrodes were applied as cathode of Li-air battery. The capacity of battery was tested. The properties of electrode on capacity of Li-air battery are discussed.

Chapter 4 proposes of PVDF-IL ionogel as the binder of carbon electrode, aiming for the development of cathode compartment of Li-O_2/CO_2 battery. The properties of electrode and ionic conductivity of between electrode and electrolyte were investigated. Solubility of O_2 and CO_2 in IL was calculated from conductor like screening model of segment activity coefficient (COSMO-SAC) to investigate the effect of reaction gases solubility in PVDF-IL ionogel binder. The benefit of PVDF-IL ionogel binder in electrode of Li-O_2/CO_2 battery is explained.

Chapter 5 discusses the effect of reaction gases on discharge capacity of Li-air battery. the electrode with PVDF-[bmim][I] ionogel binder is introduced as ionogel binder with redox mediator function. Full discharge-charge profile and cyclic performance of Li-O_2 battery using electrode with PVDF binder, PVDF-[bmim][Tf$_2$N] ionogel binder and PVDF-[bmim][I] ionogel binder are compare. The reaction mechanism in discharge and charge in each electrode are discussed.

Chapter 6 concludes a summary of this work and future outlook.

Chapter 2

Phase behavior on supercritical carbon dioxide drying and phase inversion technique

2.1 Statement of problem and objectives

It is stated on background in Chapter 1 that the new methods for fabrication of cathode must be developed to counter the problem in cathodic compartment of Li-air battery. In this study, we employed sc-CO_2 in fabrication of cathode. Cathode was fabricated by drying the solution composing of carbon particle, polymer and some additives in organic solvent with sc-CO_2. During sc-CO_2 drying, it was considered that organic solvent in dispersed solution forms homogeneous phase with sc-CO_2, providing no interfacial tension due to phase transition. This homogeneous phase formation must be investigated to elucidate the mechanism during sc-CO_2 drying.

In this chapter, we conducted preliminary experiment on the in-situ observation of phase behavior under sc-CO_2 to understand the mechanism of cathode fabrication using sc-CO_2. The experiments were conducted in high pressure view chamber where the solutions were put under sc-CO_2 fluid in batch condition. The video during experiment was recorded and homogeneous phase formation mechanism was analyzed by image processing using grayscale value. The pressure condition was varied between 10.0 to 20.0 MPa at 40 ℃. We initially conducted experiment using pure organic compounds to understand the effect of solvent properties like affinity with CO_2 and vapor pressure. Moreover, the sc-CO_2 drying of PVDF/NMP solution and CB/PVDF/NMP solution was also investigated to understand the effect of carbon nanoparticle and polymer during sc-CO_2 drying.

2.2 Experimental

2.2.1 Materials

Carbon dioxide (purity higher than 99.99 vol.%) was applied as the supercritical fluid and bought from Fuji-bussan corporation. Acetone (purity higher than 99.0 wt%), ethanol (EtOH, purity higher than 99.5 vol%), 1-methyl-2-pyrrolidone (NMP, purity higher than 99.0 wt%), 1-butanol (BuOH, purity higher than 99.0 wt%) and ethyl acetate (EA, purity higher than 99.5 wt%) were purchased from Wako pure chemical corporation. Poly(vinylidene fluoride) or PVDF was obtained from Fluorochem Ltd. Acetylene carbon black or CB (purity 99.99 %) was received from Strem Chemicals.

2.2.2 Apparatus and procedures

The schematic apparatus for experiment in this chapter is shown in Figure 2.1. The detail of main components in apparatus are listed as follows,

- Condenser: Cooling water circulation system series TBG045AE from Advantec Co., Ltd. was applied. Ethylene glycol (Wako, purity >99.0%) was used as refrigerant.

- High pressure pump: Double plunger pump series NP-D-321 from Nihon Seimitsu kagaku Co., Ltd. was applied

- Pre-heated unit: Hastelloy C22 with 750 μm inner diameter and 2 m length was used as pre-heated coil.

- High pressure vessel: High-pressure view vessel with sapphire window and detachable head was used. The Vessel volume was 72 ml. The vessel was made from SUS316 and can withstand maximum pressure and temperature at 25 MPa, 100 ℃.

- Pressure gauge: digital pressure sensor from Sankyo International Corporation was used.

- Temperature controller: Temperature controller series UNIT-PID-100 from Taiatsu Techno Corporation was employed to control temperature and cartridge heater in high-pressure vessel.

a)

1: CO$_2$ cylinder
2: water removal unit
3: condenser
4: pump
5: pre-heated unit

6: high-pressure vessel
7: pressure gauge
8: solvent trapping unit
9: Flow meter

V1: cylinder valve
V2-3: Check valve
V4: Back pressure regulator
V5-6: stop valve
V7: control valve

b)
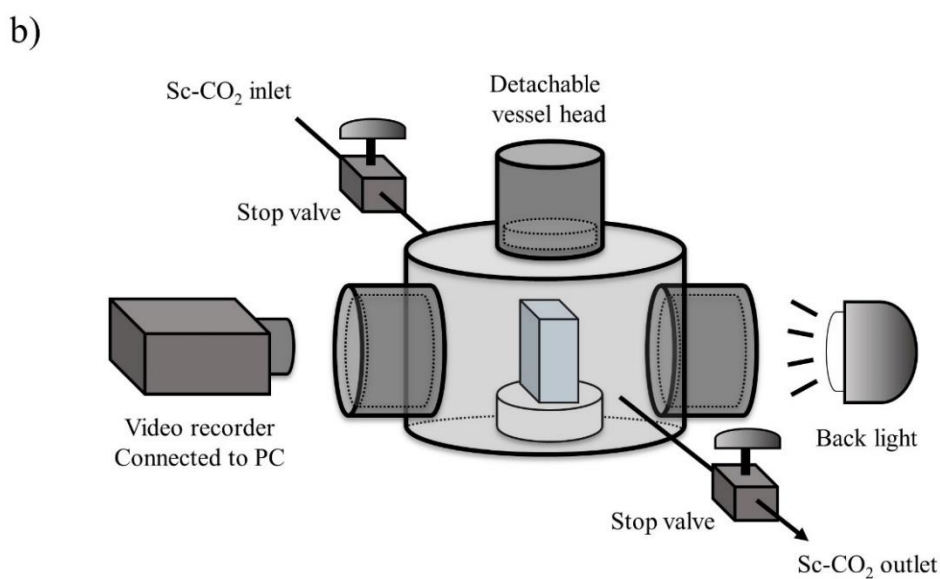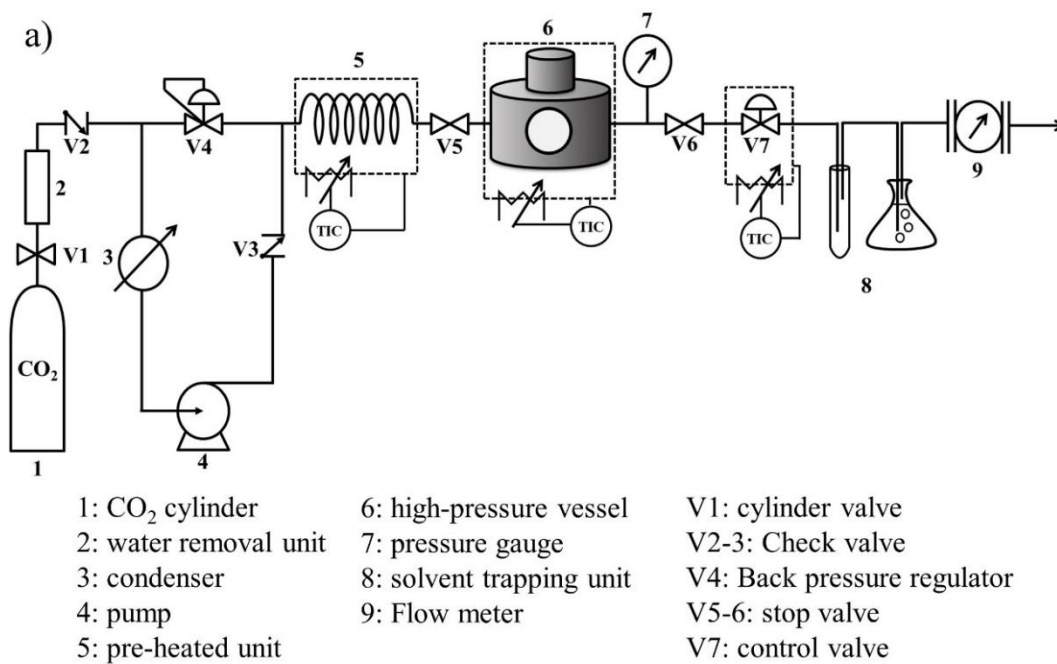
Figure 2.1 Schematic diagram of a) apparatus for view cell experiment and b) high-pressure vessel.

- <u>Heating system for the vessel</u>: Ribbon heater from Taiatsu Techno Corporation was applied to prevent cooling effect on control valve. Temperature controller was connected to this ribbon heater to control temperature.
- <u>Flowmeter</u>: Wet gas meter series W-NK from Shinagawa corporation was applied which can measure flow rate from 1-300 L h^{-1}.
- <u>Check valve</u>: check valve series 613G4Y from HOKE was applied. Valve can withstand 6000 psi pressure.
- <u>Black pressure regulator</u>: Piston type back pressure regulator from TESCOM Denki Co., Ltd. was applied to control pressure in high pressure cell.
- <u>Stop valve</u>: 2-way valves series 02-0120 from GL Science Inc. were used.
- <u>Control valve</u>: Metering valve series 1315G4Y from HOKE Inc. made from SUS316 and can maximum operate at 345 bar was applied to control flow rate.
- <u>Tubes and junctions</u>: Tubes and junctions made from SUS316 from GL science Inc. were applied in this apparatus. Diameter of tubes was 1/16, 1/8 and 1/4 inch.

For the observation of phase behavior of organic compound and sc-CO_2, approximately 3.0 mmol of pure organic compound was put and weighed in quarts cell. This cell was inserted in high-pressure vessel which was prior pre-heated at 40 ºC. After vessel was closed and locked, video camera was started recording and carbon dioxide was soon after delivered to vessel. After leaving for 1 minute, Pump which had its head cooled at -5 ºC was turned on to pump CO_2 into vessel. The time for pressurizing CO_2 from cylindrical pressure to reach supercritical state at desired pressure was set at 5.0 to 8.0 min to reduce effect according to pressurization. After desired pressure was reached, stop valves before and after high pressure cell (V5 and V6) were closed, then pressure and temperature were maintained. Video was recorded until sc-CO_2 and organic solvent formed homogeneous phase. At the end of experiment, sc-CO_2 was depressurized to atmospheric pressure by opening control valve heated at 60 ºC. Volume of CO_2 in vessel was recorded by wet-gas meter during depressurization. Molar amount of CO_2 was calculated from volume of CO_2 using ideal gas law at 25 ºC, 1.0 bar.

Phase behavior between polymer dispersed solution and carbon nanoparticle dispersed solution in sc-CO_2 was also observed. 3.3 wt% of PVDF in NMP solution was prepared by ultrasonication at 60 ºC. 1.0 wt% of CB and 1.0 wt% of PVDF in NMP solution was prepared by dissolving PVDF in NMP using ultrasonication at 60 ºC,

followed by dispersing CB in solution using ultrasonication at 25 ℃. The solution was brought into quart cell in which the molar amount of NMP in solutions was fixed at 3.0 mmol for comparison. After quart cell was delivered in high pressure vessel, the same experiments as pure organic solvent were conducted to observe the phase behaviour.

2.2.3 Analysis

Homogeneous phase formation of pure organic compounds or solutions in sc-CO_2 was analyzed by image analysis. Initially, the images of each minute from recorded video were extracted. These images were combined into time-lapse stack images using *ImageJ* software version 1.50i. The time-lapse images of bottom part of quart cell in which homogeneous phase formation occurred were cropped. The cropped stack images were converted into 8-bit. Finally, mean grayscale value of every pixels in minute t were measured using *ImageJ* software. Mean grayscale value was normalized into percent of maximum mean grayscale value among every time-lapse image as follows,

$$(\text{normalized mean grayscale})_t = \frac{(\text{mean grayscale})_t}{\text{maximum mean grayscale}} \times 100 \qquad (2.1)$$

The normalized mean grayscale value in minute t was plotted with elapsed time. Homogeneous phase formation time τ was determined as follows,

$$\tau = t_{99.90\%} - t_{\text{initial}} \qquad (2.2)$$

where t_{initial} is initial time that pressure reached desired pressure and $t_{99.90\%}$ is the initial time that normalized mean grayscale value is above 99.90%. The analysis method for determining homogeneous phase formation time is illustrated in Figure 2.2.
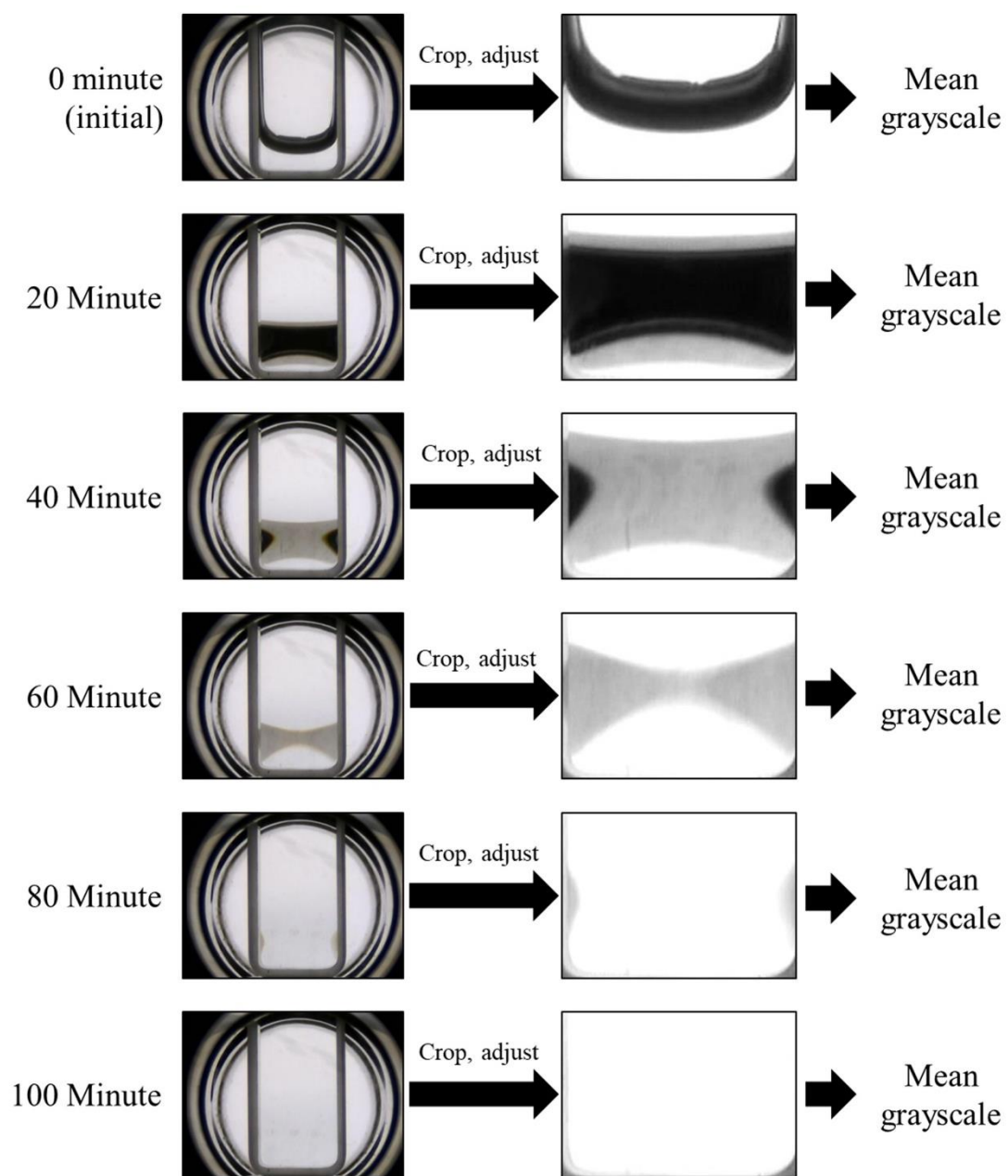
Figure 2.2 Image analysis method for homogeneous phase formation.

2.2.4 Calculation of molecular interaction energy

Molecular interaction energy between organic compound itself and interaction energy between CO_2 and organic were employed to consider effect of affinity on homogeneous phase formation time. molecular interaction is determined from probabilistic surface charge distributions based on COSMO (Conductor like Screening Model). Initially, molecular structure of CO_2 and organic compounds were optimized using *TmoleX* software version 3.3. Basis function was set as def-TZVP, while Hatree-Fock was set as level of theory before optimization. Sigma profile was calculated from surface charge density profile extracted from software. Molecular interaction energy can be calculated from following equation [89],

$$u_{ij} = \sum_{\sigma_m} \sum_{\sigma_n} \frac{A_i}{a_{\text{eff}}} P_i(\sigma_m) \frac{A_j}{a_{\text{eff}}} P_j(\sigma_n) E(\sigma_m, \sigma_n) \tag{2.3}$$

where u_{ij} is molecular interaction energy, a_{eff} is surface area of standard segment 7.50 Å^2, σ_m and σ_n is screening charge segment, A_i and A_j are surface of molecular i and j, respectively. $E(\sigma_m, \sigma_n)$ is interaction energy of the surface charge segment pair. $P_i(\sigma_m)$ and $P_j(\sigma_n)$ are molecular surface charge density to find segment σ_m in molecule i and segment σ_n in molecule j, respectively. $P_i(\sigma_m)$ can be as follows,

$$P_i(\sigma_m) = \frac{A_i(\sigma_m)}{A_i} \tag{2.4}$$

where $A_i(\sigma_m)$ is surface area of charge segment σ_m in molecule i. $E(\sigma_m, \sigma_n)$ was calculated by misfit energy from surface area of standard segment as follows [90],

$$E(\sigma_m, \sigma_n) = \frac{0.64 \times 0.3 \times a_{\text{eff}}^{3/2}}{\varepsilon_0} \tag{2.5}$$

here, ε_0 is permittivity of free space and was set as 2.395×10^{-4} e^2 mol $kcal^{-1}$ Å^{-1} in this work.

2.3 Results and discussion

2.3.1 Phase behavior of pure organic solvent in sc-CO_2

Time-lapse images of organic compounds in sc-CO_2 fluid at approximately 20.0 MPa, 40 ± 1 ℃ are summarized in Table 2.1. Since there was no flowing of sc-CO_2 in all experiments, the effect due to convection could be neglected. At initial state, liquid phase and vapor phase were separated clearly by phase boundary. After sc-CO_2 was induced into supercritical state, thick black layer was observed. This layer is considered as mixture between sc-CO_2 and organic compounds, forming non-homogeneous fluid which reflected light. Intensity of black layer became lower and disappeared as time passed by. The reduction of intensity is considered as diffusion of sc-CO_2 fluid into organic compound. When sc-CO_2 fluid was fully diffused and mixed with organic compounds, the mixture was completely formed homogeneous phase at this point where no light reflection could be observed. Moreover, Eventhough pressure, temperature and molar number of organic compounds were controlled, homogeneous phase formation time was varied with different organic compounds. This difference is considerably due to different diffusion rate of sc-CO_2 in organic compounds due to their physical properties.

The effect of pressure on homogeneous phase formation time for NMP, BuOH, EtOH, EA and acetone in sc-CO_2 fluid at 40 ± 1 ℃ are shown in Figure 2.3 to 2.7, respectively. Experimental conditions, mole fractions and homogeneous phase formation time are summarized in Table 2.2. It can be seen that homogeneous phase formation time decreases as pressure increases. Since mole fraction of sc-CO_2 in vessel increases as pressure increases, the diffusion rate of sc-CO_2 in organic solvent is higher due to larger difference of concentration. This leads to shorter time for homogeneous phase formation as diffusion rate increases. Accordingly, pressure condition is considered as one of the important factors in designing sc-CO_2 drying process.

Table 2.1 Time-lapse images of 3.0 mmol organic compounds in sc-CO_2 fluid at 40 ± 1 ℃.

Organic compound (pressure)	t (min)														
	0	5	10	15	20	25	30	40	50	60	70	80	90	100	110
NMP (200.88 ± 1.25 bar)															
1-BuOH (197.74 ± 2.48 bar)															
EtOH (197.93 ± 2.09 bar)															
Ethyl acetate (202.99 ± 2.43 bar)															
acetone (204.16 ± 0.57 bar)															
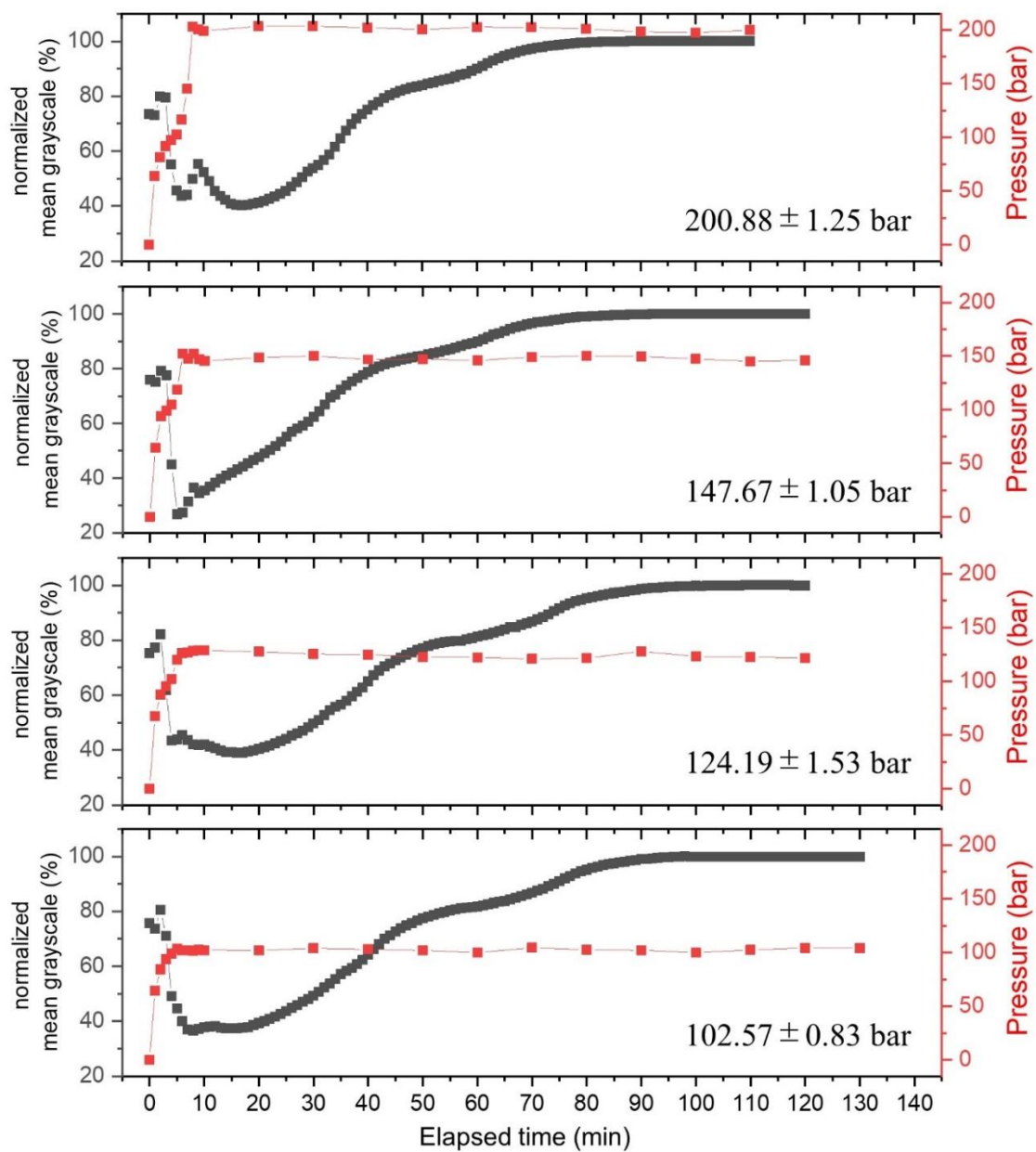
Figure 2.3 Normalized mean grayscale profile of 3.0 mmol NMP in sc-CO_2 at 40 ± 1 ℃.
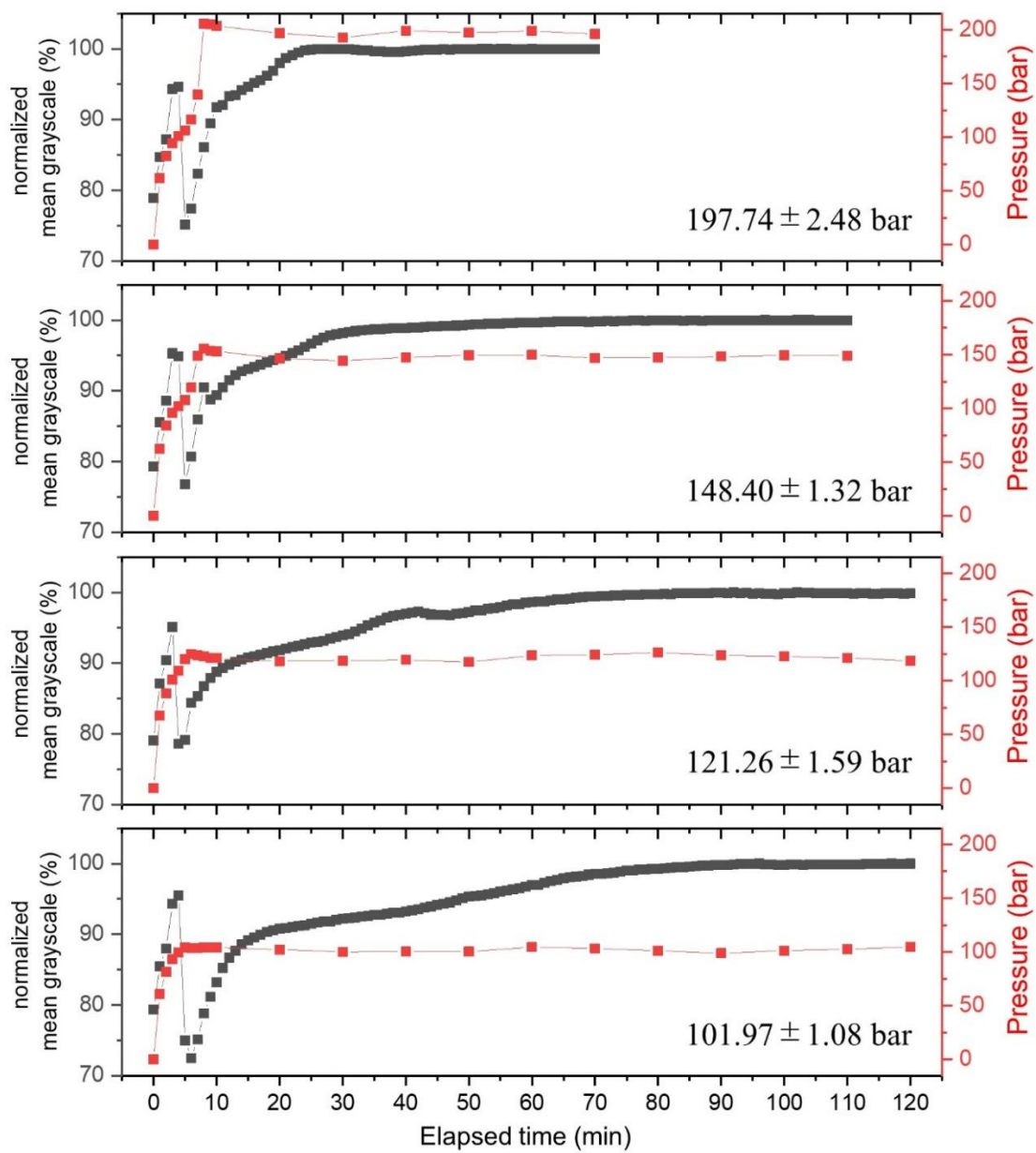
Figure 2.4 Normalized mean grayscale profile of 3.0 mmol 1-butanol in sc-CO$_2$ at 40 ± 1 °C.
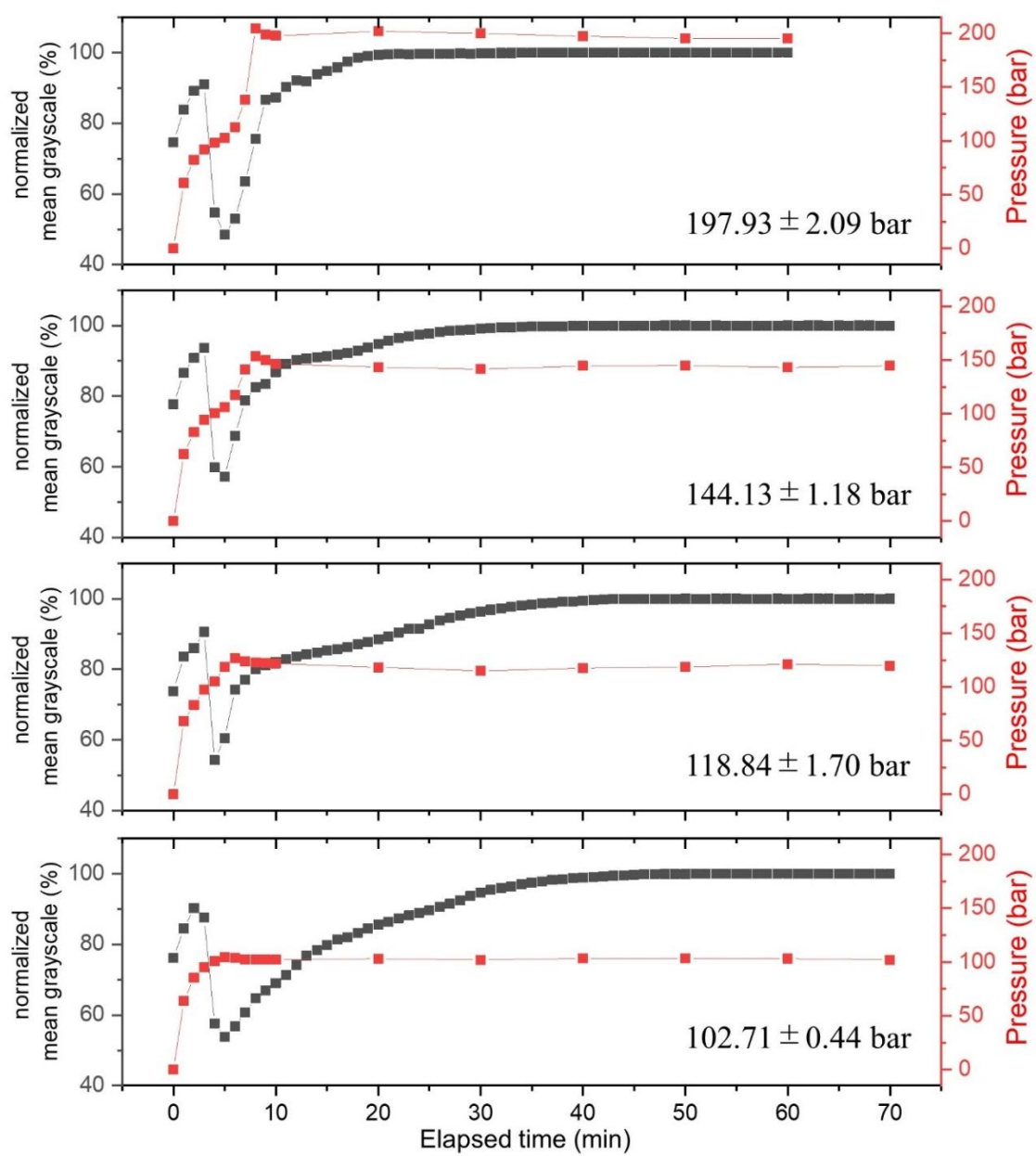
Figure 2.5 Normalized mean grayscale profile of 3.0 mmol ethanol in sc-CO_2 at $40 \pm 1\ ℃$.
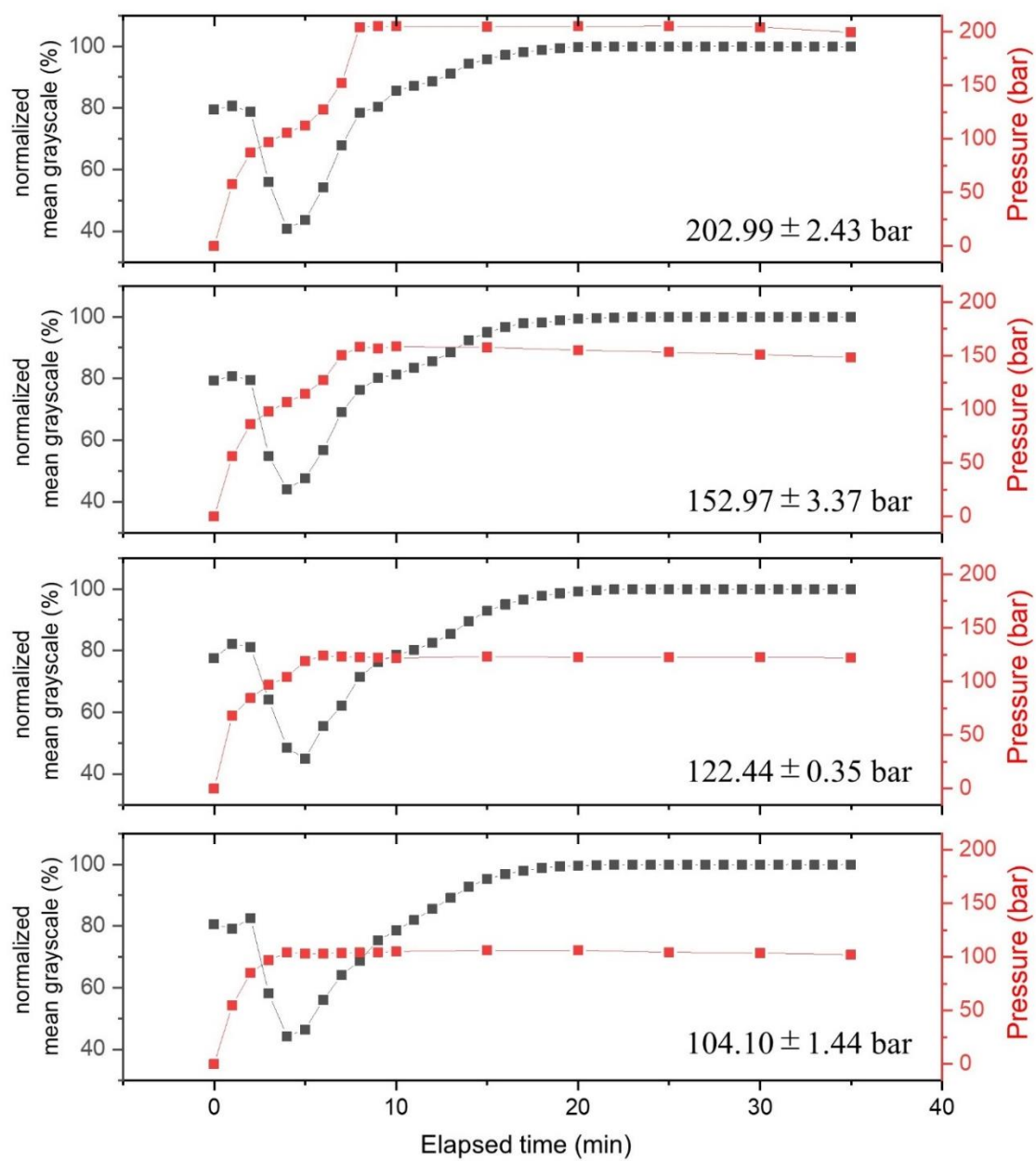
Figure 2.6 Normalized mean grayscale profile of 3.0 mmol ethyl acetate in sc-CO_2 at 40 ± 1 ℃.
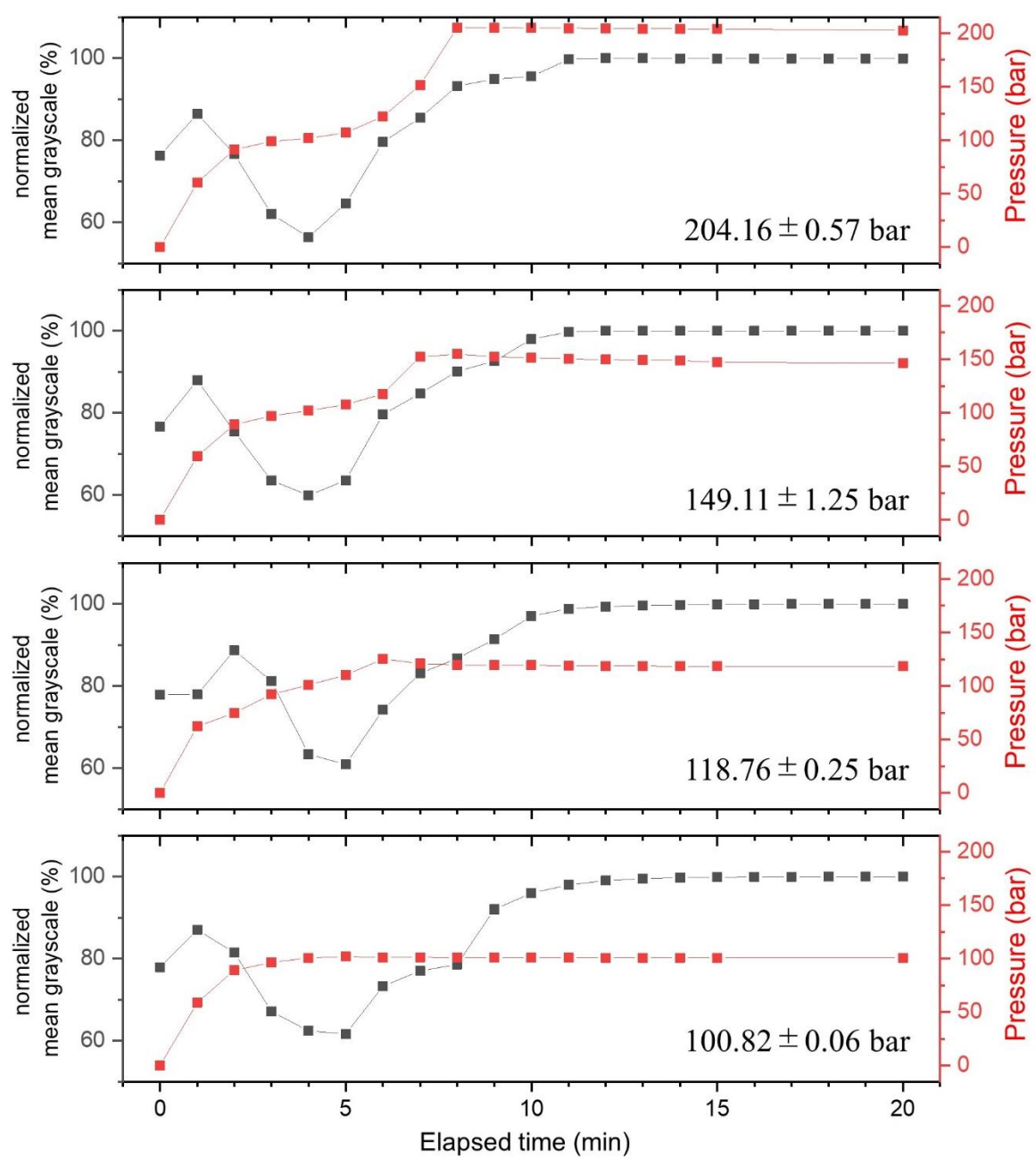
Figure 2.7 Normalized mean grayscale profile of 3.0 mmol acetone in sc-CO_2 at 40 ± 1 °C.

Table 2.2 Mole fraction and homogeneous phase formation time.

organic compound (OC)	Pressure (bar)	CO_2 (mmol)	y_{OC} (mmol)	y_{CO2} (mol mol^{-1})	Homogeneous phase formation time τ (min)
NMP	102.57 ± 0.83	5.364×10^2	3.002	0.9944	108
	124.19 ± 1.53	6.227×10^2	3.071	0.9951	99
	147.67 ± 1.05	7.248×10^2	3.007	0.9959	85
	200.88 ± 1.25	7.843×10^2	3.055	0.9961	77
EtOH	102.71 ± 0.44	4.424×10^2	3.074	0.9931	46
	118.84 ± 1.70	6.095×10^2	2.998	0.9951	37
	144.13 ± 1.18	6.814×10^2	3.080	0.9955	33
	197.93 ± 2.09	7.364×10^2	3.074	0.9958	26
1-BuOH	101.97 ± 1.08	4.564×10^2	3.018	0.9934	107
	121.26 ± 1.59	6.080×10^2	3.052	0.9950	80
	148.40 ± 1.32	6.923×10^2	3.025	0.9956	68
	197.74 ± 2.48	7.588×10^2	3.033	0.9960	36
Acetone	101.97 ± 1.08	4.486×10^2	2.972	0.9934	12
	118.76 ± 0.25	6.149×10^2	3.065	0.9950	9
	149.11 ± 1.25	6.884×10^2	2.996	0.9957	6
	204.16 ± 0.57	7.619×10^2	3.035	0.9960	5
EA	104.10 ± 1.44	4.788×10^2	2.995	0.9938	20
	122.44 ± 0.35	6.219×10^2	3.090	0.9951	17
	152.97 ± 3.37	7.008×10^2	3.003	0.9957	16
	202.99 ± 2.43	7.634×10^2	3.013	0.9961	14

The correlation of molar amount of carbon dioxide with homogeneous phase formation time is shown in Figure 2.8a. It was found that homogeneous phase formation time has linear relation with negative value of natural log of CO_2 mole fraction or $-\ln(y_{CO2})$, which can be shown as following equation,

$$\tau = -\tau' \ln(y_{CO_2})$$
(2.6)

here, τ' is named as homogeneous phase formation time constant, which varied differently due to organic compounds. τ' value also implies the time to form homogeneous phase with sc-CO_2 for one organic compounds. Organic compound with higher τ' value spends longer time to form homogeneous phase under the same pressure condition. τ' value after linear regression from experimental data are summarized in Table 2.3.

Homogeneous phase formation time constant τ' is considered as predictable parameter. In this work, molecular interaction energy among organic compounds itself u_{11}, molecular interaction energy between organic compounds and CO_2 u_{12} and viscosity μ are considered as parameters affecting τ'. It is considered that τ' is proposional to u_{11} and reversely proposional to u_{12}. This is regarded since u_{11} reflects the cohesive force in organic compound while u_{12} reflects the adhesive force between organic compounds and CO_2. Moreover, τ' is considered to be proposional to μ, because sc-CO_2 fluid tends to diffuse slowly in organic compound with comparatively high viscosity. The value of u_{11}, u_{12} and μ are summarized in Table 2.3. Results of linear regression regarding to above consideration is shown in Figure 2.8b, in which equation can be expressed as follows,

$$\tau' = 5180.82\mu\left(\frac{u_{11}}{u_{12}}\right)$$
(2.7)

The result of linear regression shows high consistency with R-square value of 0.997. This result implies that physical properties of organic compound can be employed to predict time to form homogeneous phase with sc-CO_2.

Table 2.3 Physical properties and homogeneous phase formation time constant of organic compounds.

Organic compound	u_{11} (kJ mol^{-1})	u_{12} (kJ mol^{-1})	u_{11}/u_{12}	μ (mPa s)	τ' (min)
NMP	1112.73	402.00	2.77	1.348 [91]	19874
1-butanol	688.26	402.72	1.71	1.773 [92]	14945
EtOH	480.39	335.30	1.43	0.866 [93]	6902
Ethyl acetate	841.54	443.21	1.90	0.343 [94]	3420
Acetone	634.91	385.14	1.65	0.284 [95]	1650

Viscosity was referred or estimated at 313.15 K
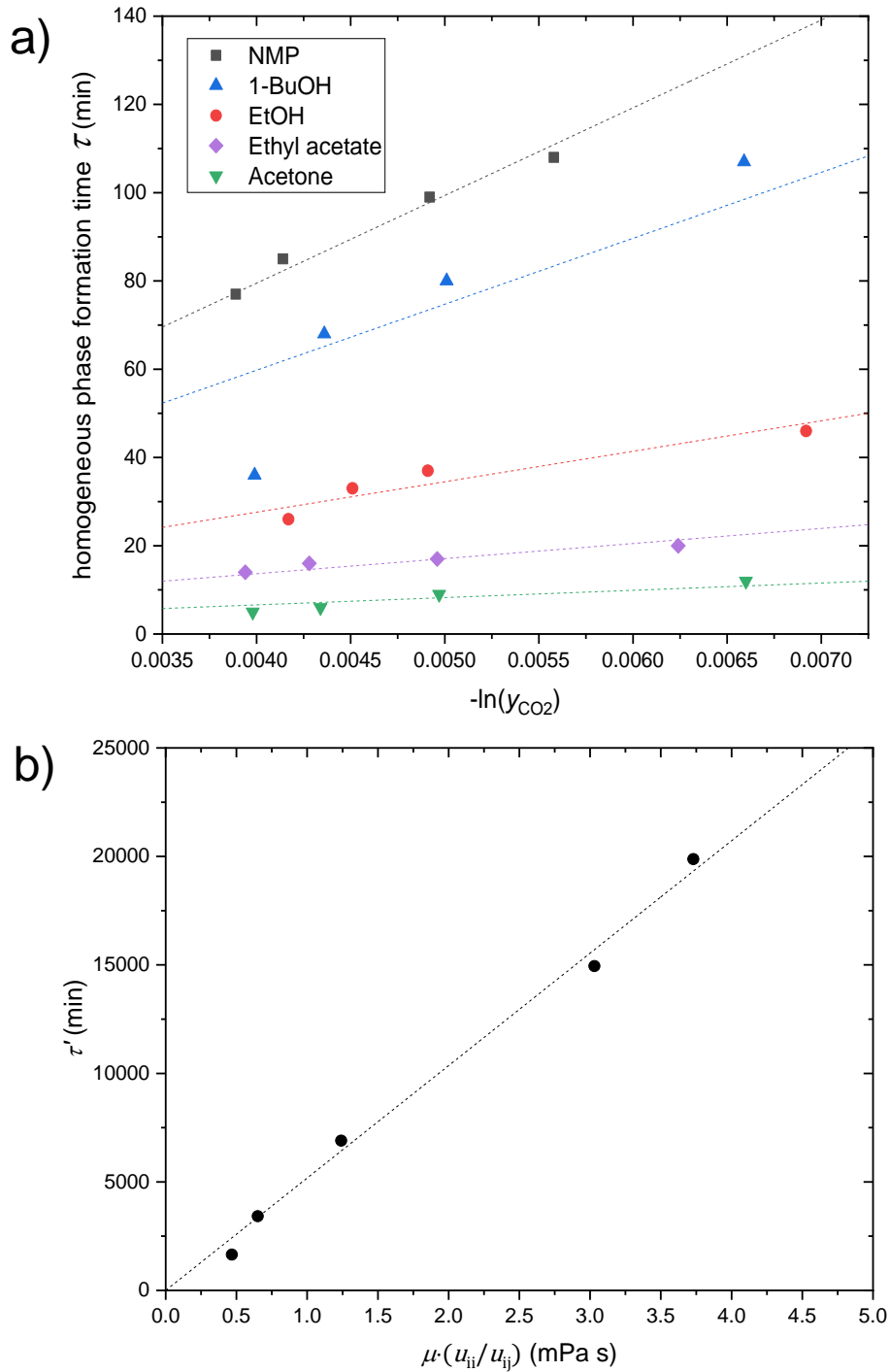
Figure 2.8 Correlation and estimation between a) homogeneous phase formation time and mole fraction of CO_2, b) homogeneous phase formation constant and physical properties of organic compounds.

2.3.2 Phase behavior observation of PVDF/NMP in sc-CO$_2$

Phase behavior of 3.3 wt% of PVDF in NMP solution in sc-CO$_2$ fluid was observed to investigate effect of polymer during sc-CO$_2$ drying of solution. three pressure conditions between 10.0 to 20.0 MPa were observed to consider effect of pressure. Time-lapse images of PVDF/NMP solution in sc-CO$_2$ fluid are shown in Table 2.4, while the normalized mean grayscale profiles of the bottom part are presented in Figure 2.9. It is clearly seen that the mechanism of sc-CO$_2$ drying of PVDF/NMP solution is different from case of pure NMP. In case of PVDF/NMP solution, the solution formed two phases, separating as the upper part and the bottom part after sc-CO$_2$ was pressurized into the vessel. The light intensity of upper part became lighter and disappeared after time passed by. Simultaneously, intensity of lower part became darker and finally black. The lower part was then lower its level, finally leave thin black layer at the bottom.

The explanation of this phenomena is illustrated in Figure 2.10. Initially sc-CO$_2$ is dissolved in solution. However, sc-CO$_2$ acts as anti-solvent to NMP which decreases solubility of PVDF in NMP solution. This leads to phase separation between NMP/sc-CO$_2$ in the upper part and PVDF/NMP/sc-CO$_2$ in the lower part. Sc-CO$_2$ initially forms homogeneous phase in the upper phase then further dispersed into lower phase, leading to crystallization of PVDF. The crystallization of PVDF was observed as lower part became darker. As PVDF is insoluble in sc-CO$_2$ fluid, repulsive force between PVDF and sc-CO$_2$ is occurred, leading to the aggregation of polymer at the end. This phenomenon can be called as phase inversion since sc-CO$_2$ acts as anti-solvent to PVDF/NMP solution. The results from this experiment shows that highly porous polymer matrix cannot be fabricated by this method since polymer was aggregated at the end of process. Results from Figure 2.9 also implies that the phase inversion of sc-CO$_2$ in PVDF/NMP solution is occurred faster under higher sc-CO$_2$ pressure condition. This conforms to the results of pure organic compounds due to the larger diffusion rate of sc-CO$_2$ in higher pressure condition.

Table 2.4 Time-lapse images of PVDF/NMP solution and CB/PVDF/NMP solution in sc-CO$_2$ fluid at 40 ± 1 ℃.

Figure 2.9 Normalized mean grayscale profile of 3.3 wt% PVDF/NMP in sc-CO_2 at 101.30 bar (—■—), 151.66 bar (—●—) and 200.83 bar (—▲—). Temperature was $40 \pm$ 1 ℃ in all investigation.
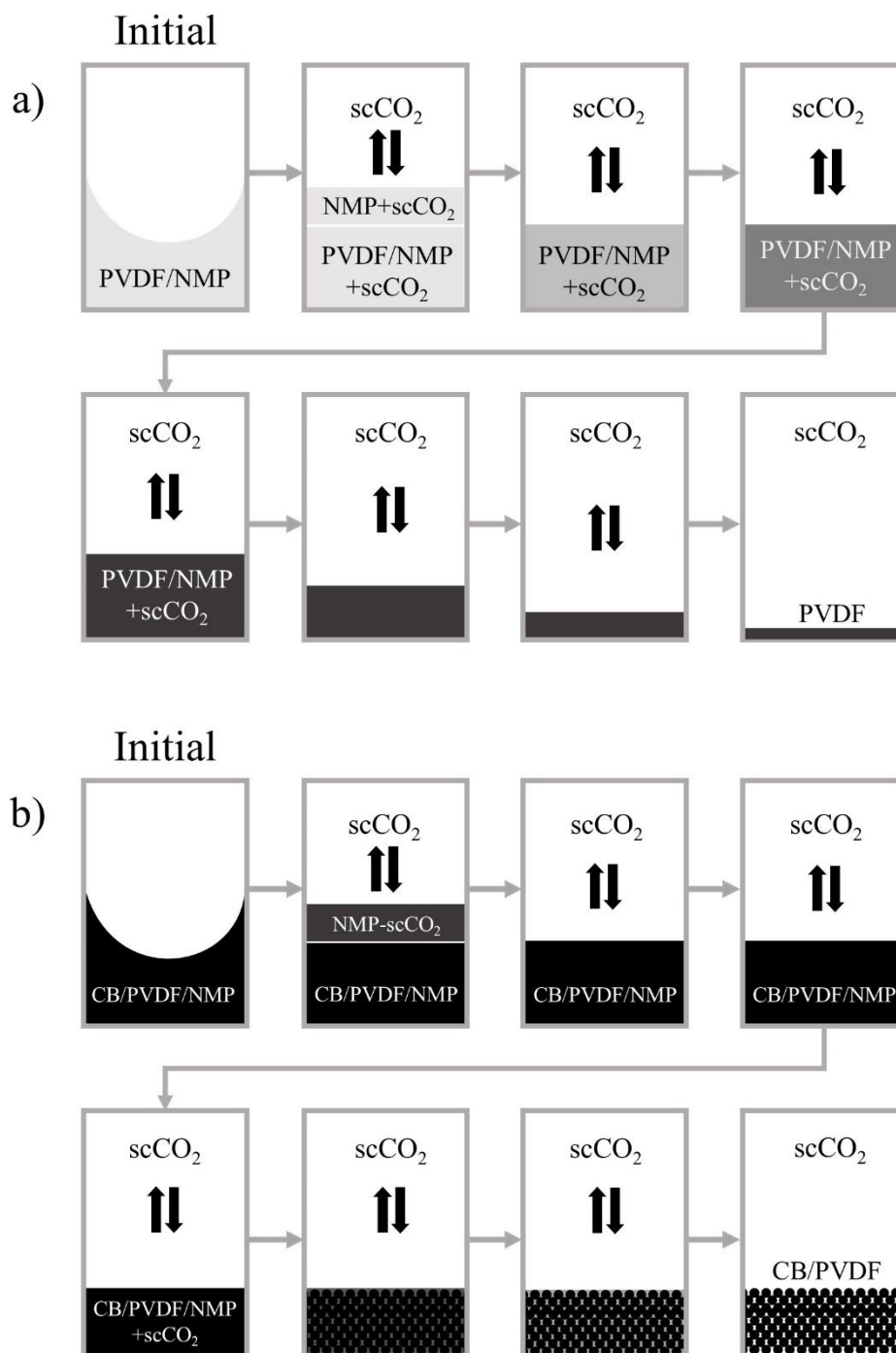
Figure 2.10 Mechanism of phase inversion by supercritical carbon dioxide in a) PVDF in NMP solution and b) CB/PVDF in NMP solution.

2.3.3 View cell investigation of CB/PVDF/NMP in sc-CO$_2$

Phase inversion of sc-CO$_2$ in 1.0 wt% CB/PVDF/NMP solution was observed at 20.0 MPa, 40 ℃. Time-lapse images of 1.0 wt% CB/PVDF/NMP solution in sc-CO$_2$ fluid are shown in Table 2.4. Initially, carbon dispersed solution was expanded after sc-CO$_2$ was delivered to vessel. As time passed, light intensity of upper part of solution became weaker and finally disappeared. However, the structure of bottom part can be maintained until the end of process, which was different from the case of PVDF/NMP solution that polymer was aggregated at bottom of quart cell.

The mechanism of phase inversion of sc-CO$_2$ in CB/PVDF/NMP solution is illustrated in Figure 2.10. It is considered that solution was separated into upper phase and bottom phase like the case of PVDF/NMP. Sc-CO$_2$ then forms homogeneous phase with the upper phase as it disappeared. The dissolution of sc-CO$_2$ in lower phase leads to the crystallization of PVDF. However, unlike the case of PVDF/NMP, crystallized PVDF forms among carbon particle instead of aggregated at the bottom. This result enlightens the role of carbon particle in phase inversion process that it helps maintain the porous structure, despite the effect of anti-solvent by sc-CO$_2$. Accordingly, sc-CO$_2$ fluid can be employed in phase inversion of carbon and polymer dispersed organic solution to fabricate porous carbon structure. This technique is further applied as fabrication method of porous carbon cathode for Li-air battery, which is stated in the next chapter.

Chapter 3

Fabrication of porous carbon electrode
using phase inversion and drying by supercritical carbon dioxide

3.1 Statement of problems and objectives

Li-air battery is one of the promising energy storages for next generation due to its relatively high energy density. However, many prospects including cathode compartment must be developed to achieve capacity nearly to its theoretical value. One of the problems regarding to cathode compartment is pore clogging by discharge product. This leads to the necessary of development of highly porous cathode, which can reduce pore clogging by discharge product and simultaneously enhance air transportation during discharging process. The mechanism of phase inversion and homogeneous phase formation of sc-CO_2 on carbon and polymer dispersed organic solvent solution was previously explained in Chapter 2. This technique can be applied to fabricate highly porous electrode because of the homogeneous phase formation between organic compounds in solution and sc-CO_2 fluid, providing zero interfacial tension during process. In this chapter, we applied sc-CO_2 in fabrication of cathodes for Li-air battery, while evaporation was employed as comparative method. The effect of pressure condition of sc-CO_2 on physical properties of electrodes were investigated. Finally, electrodes dried by evaporation and sc-CO_2 drying were applied in actual Li-air batteries. Capacity was tested with dried air in this experiment. The effects of pressure condition and content of polymer in cathode toward capacity of batteries were investigated.

3.2 Experimental

3.2.1 Materials

Carbon dioxide (99.5 %) was purchased from Fujii-bussan. Acetylene carbon black or CB (99.99 %) with 40 nm diameter was bought from Strem chemicals. Poly(vinylidene fluoride) or PVDF was obtained from Fluorochem. 1-Methyl-2-pyrrolidone or NMP (99.0 %), Mangenses (IV) Oxide or MnO_2, Lithium Bis(trifluoromethanesulfonyl)imide or LiTFSI (90.0 %) were purchased from Wako. 1-

Butyl-3-methylimidazolium bis(trifluoromethylsulfonyl)imide or [bmim][Tf$_2$N] (98.0 %) was bought from Tokyo Chemical Industry. Lithium foil (99.9 %) with 15 mm diameter and 0.2 mm thickness was purchased from Honjo Metal Co., Ltd.

3.2.2 Fabrication of electrodes

3.2.2.1 Preparation of black viscous slurry

Black viscous slurry, in which CB and PVDF were dispersed, was prepared by following method. Initially, PVDF was dissolved into NMP by ultra-sonication at 60 ℃ until polymer was fully dissolved. carbon black was soon after added to the solution and dispersed by ultra-sonication at room temperature for 1 h. Finally, the black viscous slurry was stirred by magnetic stirrer at room temperature for 12 h. Weight ratio of PVDF to CB and PVDF to NMP were controlled at 1.5 and 27, respectively.

Black viscous slurry, in which CB, MnO$_2$ and PVDF were dispersed, was prepared and further used as cathode compartment of Li-air battery after drying. The slurry was prepared as follows. Initially, PVDF was dissolved into NMP by ultra-sonication at 60 ℃ until polymer was fully dissolved. MnO$_2$ was added in this solution and dispersed by ultra-sonication at room temperature for 1 h. Then, carbon black was put into the solution and dispersed by ultra-sonication at room temperature for 1 h. The black viscous slurry was finally stirred by magnetic stirrer at room temperature for 12 h. Weight ratio of PVDF to MnO$_2$ and PVDF to NMP were fixed at 0.3 and 27, respectively, while weight ratio of CB to PVDF was varied as 0.5, 1.0 and 1.5.

3.2.2.2 Drying of black viscous slurry

1.00 g of black viscous slurry was weighed and put in clean Petri dish (34 mm inner diameter). The Petri dish was tapped to spread out slurry uniformly. NMP in slurry was soon after dried by evaporation or sc-CO$_2$ fluid. In term of evaporation, the slurry was brought into thermostat which has temperature controlled at 80 ℃ for 12 h. The apparatus used for cathode fabrication by sc-CO$_2$ is shown in Figure 3.1. The detail of apparatus components is listed as follows,

- Condenser: Cooling water circulation system series TBG020AA from Advantec Co., Ltd. was applied. Ethylene glycol (Wako, purity >99.0%) was used as refrigerant.
- High pressure pump: Double plunger pump series NP-D-321 from Nihon Seimitsu kagaku Co., Ltd. was applied
- Pressure gauge: Analog pressure meter from Tiatsu Techno Corporation which can show pressure between 0-35 MPa was used at the entrance of the cell. Digital pressure meter series VSM3-2S-A3-A3-4 and pressure senser series VESI M50 2M from VALCOM were used to shown pressure in cell.
- Thermostat: Automatic oven series EO-300B from AS ONE Corporation was applied
- High pressure cell: 80 mL cylindrical high-pressure cell (SUS316, maximum opration at 25 MPa, 100 ºC) with 40 mm inner diameter, 70 mm outer diameter and 64 mm inner height was used in experiment.
- Flow meter: Wet gas meter series W-NK from Shinagawa corporation was applied which can measure flow rate from 1-300 L h^{-1}.
- Heating system: Heating system from Taiatsu Techno Corporation was applied to prevent cooling effect on control valve. Temperature controller was connected to this ribbon heater to control temperature.
- Check valve: check valve series 613G4Y from HOKE was applied. Valve can withstand 6000 psi pressure.
- Stop valve: 2-way valves series 02-0120 from GL Science Inc. were used.
- Black pressure valve: Piston type back pressure valve from TESCOM Denki Co., Ltd. was applied to control pressure in high pressure cell.
- Control valve: Metering valve series 1315G4Y from HOKE Inc. made from SUS316 and can maximum operate at 345 bar was applied to control flow rate.
- Tubes and junctions: Tubes and junctions made from SUS316 from GL science Inc. were applied in this apparatus. Diameter of tubes was 1/16, 1/8 and 1/4 inch.

a)

b)
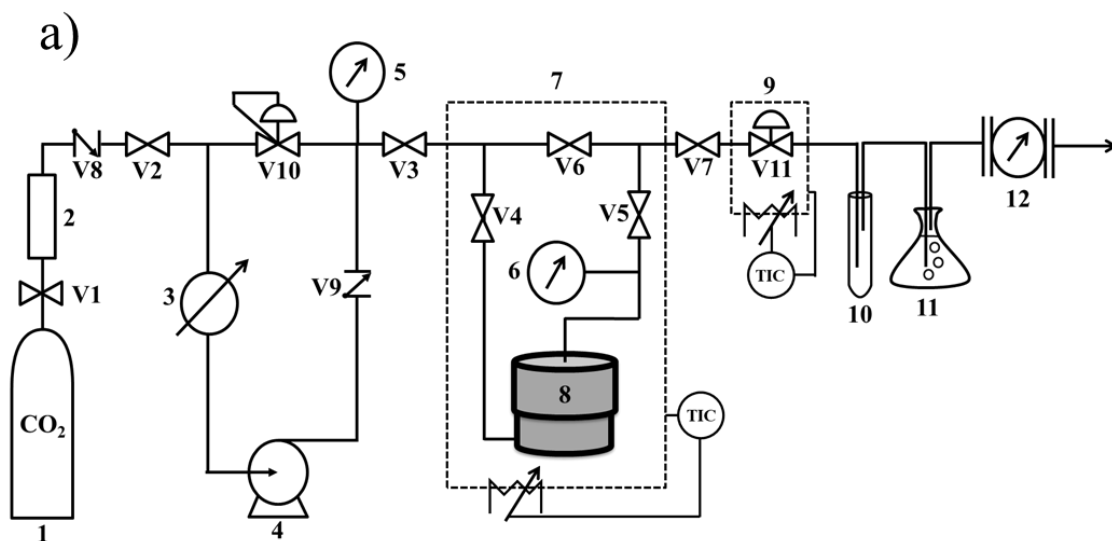
1: CO_2 cylinder	8: high-pressure cell	V1: cylinder valve
2: water removal unit	9: pre-heated unit	V2-3: Check valve
3: condenser	10: trapping unit	V4-9: stop valve
4: pump	11: gas saturated unit	V10: Back pressure regulator
5-6 : pressure gauge	12: Wet-gas flowmeter	V11: control valve
7: thermostat		
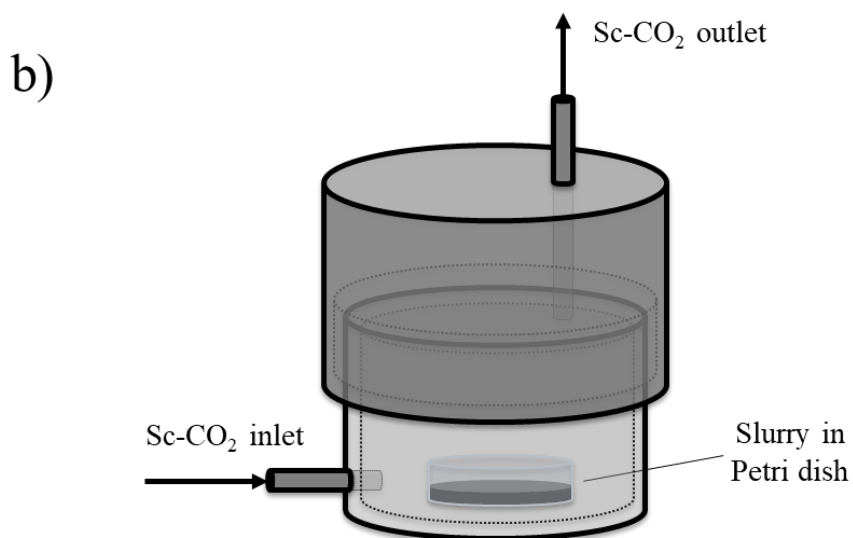
Figure 3.1 Schematic diagram of a) apparatus for cathode fabrication by supercritical carbon dioxide fluid and b) high-pressure cell.

The carbon electrodes were fabricated by sc-CO_2 fluid as follows. Initially, the temperature of high-pressure cell was initially keeped at 40 ℃ prior to the experiment. The Petri dish containing slurry was put into heated high-pressure cell and was then locked to prevent leakage of carbon dioxide. The valve of carbon dioxide cylinder and stop valves before high pressure cell were soon after released to flow carbon dioxide into high-pressure cell. In this step, the pressure of cell was equalized to cylindrical pressure. Carbon dioxide was cooled and pumped into high pressure cell to pressurize carbon dioxide into supercritical state until desired pressure. After pressure was reached, the stop valve and control valve at the exit of the vessel was opened to flow the mixture of solvent and sc-CO_2 out of cell. Flowrate of sc-CO_2 was controlled at approximately 6.0 mmol min^{-1} by adjusting control valve. After the operation for 6 h, the pump and valve of cylinder were closed, and sc-CO_2 was gradually drained out to depressurize until atmospheric pressure. Time for depressurization in this step was approximately 4 h. Petri dish was put out from the high-pressure cell soon after depressurization. It has to be mentioned that the pressure conducted in this experiment was set over 10.0 MPa to confirm the homogeneous phase between sc-CO_2 and NMP, according to critical point of CO_2 + NMP mixture at 9.0 MPa, 40 ℃ [96].

3.2.3 Characterization

3.2.3.1 Morphology investigation

Surface morphology of electrodes was investigated by field emission scanning electron microscope (FE-SEM) series S-4700 from Hitachi located in Technical Department, Ookayama Materials Analysis Division, Tokyo Institute of Technology. Accelerating voltage and beam current were set to 8.0 kV and 10.0 μA, respectively in all investigation.

3.2.3.2 Porosity measurement

Porosity of electrodes was calculated by following equation,

$$\text{porosity} = \frac{V_{void}}{V_{total}} \tag{3.1}$$

where V_{void} is void volume of the composite and V_{total} is total volume of the composite. Total volume of composite can be calculated as follows,

$$V_{total} = A_{top} \times h_{av} \tag{3.2}$$

A_{top} is top area of the composites and h_{av} is average thickness of the composite. Top area of the composite was measured by image analysis of the bird-eye view images of composite using particle analysis function on *imagej* software version 1.50i. To measure thickness of the composite, cross-sectional images of composite were taken using scanning electron microscope (JSM-6000 Plus, JEOL). Average thickness of the composite was calculated from approximately 400 spots of thickness among all cross-sectional SEM images. The confidence interval for the calculation of average thickness was confirmed to be higher than 95.0 %. V_{void} of the composite was measured as follows,

$$V_{void} = V_{total} - \sum \frac{w_{solid,liquid}}{\rho_{solid,liquid}} \tag{3.3}$$

where $w_{solid,liquid}$ and $\rho_{solid,liquid}$ are weight and density of each solid components (CB, PVDF, MnO_2) or liquid component (IL) inside the composite, respectively. Weight of solid components were calculated from initial weight of slurry in Petri dish. Density of CB was measured from Archimedes' principle by replacing CB particle in acetone (Wako, >99.0 %). Density of PVDF was measured from the same principle by replacing PVDF in ultrapure water. Density of MnO_2 was obtained from company (Wako).

3.2.3.3 Electrical conductivity measurement

The electrical conductivity of electrode was considered from theory of sheet conductivity and measured by 4-point probe method. Initially, resistance of composite R was calculated from slope of linear relation between potential V and electric current I. This was measured by Potentiostat Galvanostat (VersaSTAT3-200, Princeton Applied Research) using linear scan voltammetry function with 0.1 V s^{-1} scan rate. Sheet conductivity can be measured from the following equation [97],

$$\text{sheet conductivity} = \frac{\ln 2}{\pi h_{av} R \cdot F(h_{av}/s)} \tag{3.4}$$

where, R is resistance and s is length between each probe which was fixed at 0.5 cm in this experiment. It should be noted that $F(h_{av}/s)$ is considered as unity in this experiment since h_{av}/s ratio is less than 0.2.

3.2.3.4 Thermogravimetric analysis

Thermogravimetric data (TG) were collected from thermogravimetric analyzer TGA-50 series (SHIMADZU). The heating rate was set to 3.0 °C min^{-1} from ambient temperature until 550.0 °C in all experiment. Weight loss of compsite during measurement was calculated by following equation,

$$\text{weight } (\%) = \frac{w_T}{w_0} \times 100 \tag{3.5}$$

w_T is weight of sample at temperature T and w_0 is initial weight of sample. Weight of sample at 200 °C was used as initial weight to avoid effect from impurities. Derivative Thermogravimetric data (DTG) were calculated from first derivative function in TA60 software version 2.2.1 (SHIMADZU).

3.2.3.5 X-ray powder diffraction analysis

The effect of sc-CO_2 fluid on the crystallinity of PVDF can be investigated because PVDF is semi-crystaline polymer. The X-ray powder diffraction (XRD) analysis was measured by D8 discover μHR (Bruker AXS) located in Technical Department, Ookayama Materials Analysis Division, Tokyo Institute of Technology. The obtained data were analyzed by PDXL software (Rigaku) to find crystallinity of PVDF by peak deconvolution method as follows [98],

$$\text{crystallinity} = \frac{\text{total integral intensity of crystalline PVDF}}{\text{total integral intensity of PVDF}} \tag{3.6}$$

peak area for crystalline PVDF were considered from $2\theta = 18.4$ for α-PVDF and $2\theta = 20.2$ for β-PVDF [99, 100]. Here, the peak at $2\theta = 25.7$ was considered as carbon black. The left peak area between $2\theta = 18.4$ and 20.2 was considered as amorphous PVDF. Finally, all peak area was fitted in the software by fix peak area between acetylene carbon black and PVDF as 1.5 which equals to weight ratio of those two components.

3.2.4 Li-air battery test

3.2.4.1 Battery assembly

The as-prepared electrode fabricated by sc-CO_2 fluid was cut into round disk with 13.0 mm diameter. In term of evaporation, 13.0 mm diameter of carbon sheet was cut and immersed into black viscous slurry, followed by evaporation at 80 ℃ for 12 h. This electrode was used as electrode fabricated by evaporation. Next, all Li-air battery components including electrode were brought into glovebox. Argon gas was flowed in the glovebox to fill the inert gas inside and decrease humidity. After humidity was 5.0 %, the battery was assembled and crimped by the coin cell crimping machine. 150 μl of 1.0 M LiTSFI in [bmim][Tf$_2$N] was dropped into Whatman^{TM} glass fiber filter, grade GF/A as a separator in argon atmosphere. The schematic diagram for structure of coin cell Li-air battery are shown in Figure 3.2a. The apparatus and materials were listed as follows,

- Glovebox: Large-scale glove box (800 × 600 × 620 mm) was from AS ONE Corporation. argon gas was filled in the glovebox prior to battery assembling
- Argon gas: Purity 99.99% Argon gas was bought from Fujii-Bussan
- Crimper: Hydraulic Crimper for CR2032 Case series MSK-110 from MTI corp. was used for coin cell crimping. All coin cells were crimped at 1000 psi.
- Humidity meter: Temperature/humidity meter from AS ONE Corporation was used in glove box. Minimum relative humidity which can be detected is 5.0 %.
- Coin cell case: Meshed CR2032 Coin cells cases series CR2032-CASE-304-MESH from MTI corporation were used in coin cell assembly. Cases are made from SUS316 with 20mm outer diameter and 15.8 mm inner diameter. Diameter of mesh was 12 mm diameter and pore size was 1 mm.
- Spacer: 304 Stainless Steel spacers with 15.5 mm diameter and 0.2 mm thickness were used in coin cell assembly.

a)

1: coin cell case   2: spacer   3: lithium foil
4: electrolyte layer   5: cathode

b)

1: Air cylinder   2: regulator   3: flowmeter
4: aluminium case   5: coin cell   6: coin cell holder
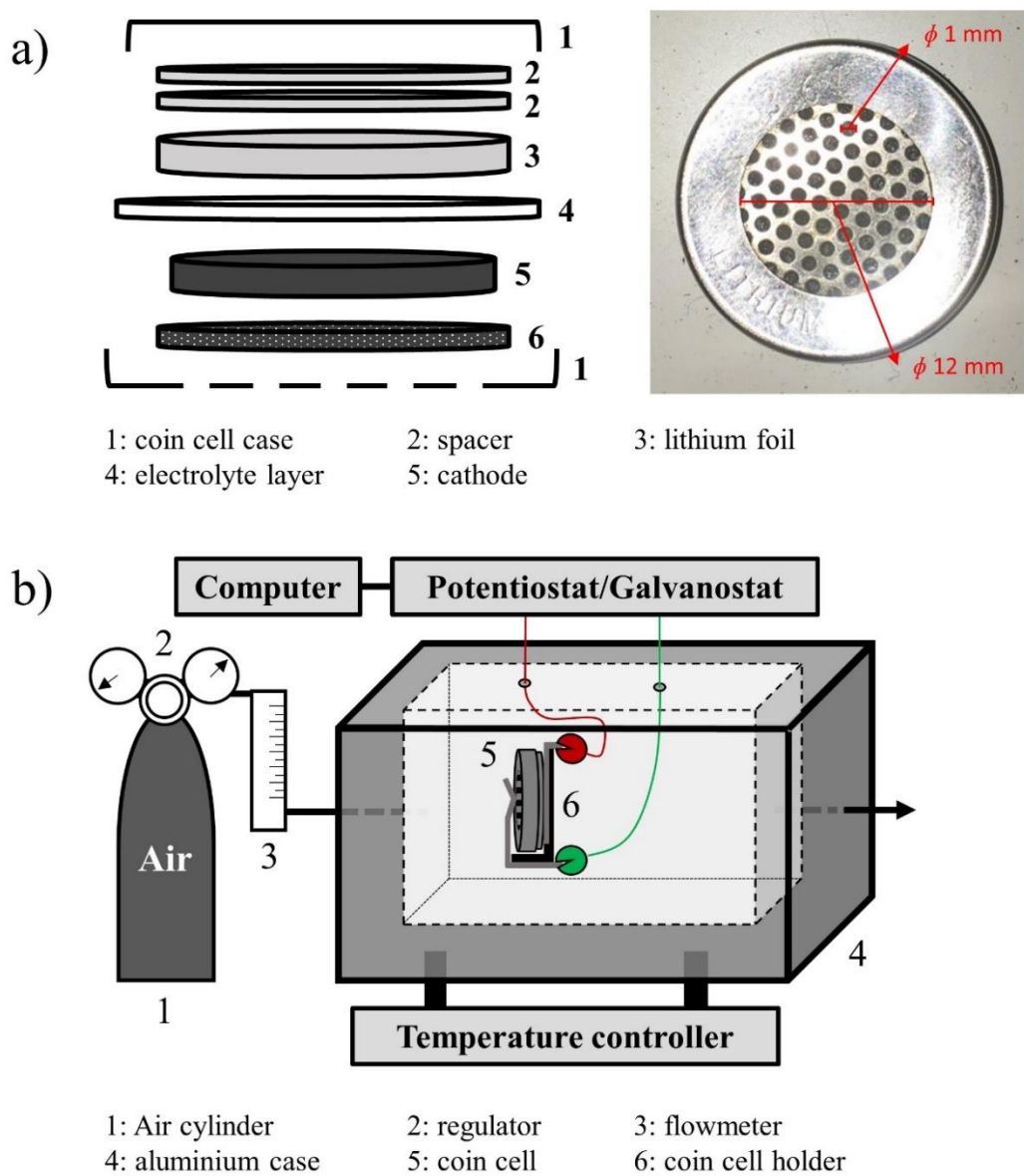
Figure 3.2 Schematic diagram of a) CR2032 meshed coin cell with actual image and b) apparatus for capacity measurement of Li-air battery.

- Li metal: Li metal disks from Honjo Metal Co., Ltd. with 15 mm diameter and 0.2 mm thickness were used in coin cell assembly.
- Separator: Whatman[TM] glass microfiber filters GF/A (21 mm diameter, 260 μm thickness, 1.6 μm pore size) was used with electrolyte as a separator between Li metal and cathode in coin cell assembly.
- Gas diffusion layer: Teflon[TM] treated TORAY[TM] carbon paper series EC-TP1-060T (0.44 g cm^{-3}, 0.19 mm thickness) was cut into 15.5 mm diameter round disk and used as gas diffusion layer in coin cell assembly.

3.2.4.2 Capacity measurement of Li-air battery

Assembled Li-air battery was locked into coin cell holder which is located inside the aluminium cell box and connected with Potentiostat/Galvanostat. Before measurement, this cell box was pre-heated and temperature was controlled at 25 ºC, then pure air was flowed into the cell at approximately 50 ml min^{-1}, 1.0 bar. Capacity of electrode was measured by Potentiometry function in Potentiostat/Galvanostat. In this measurement, the current was fixed at 0.1 mA (0.075 mA cm$^{-2}_{cathode}$) and measurement range is set between 1.5 to 4.5 V. specific capacity was calculated from cathode surface area, which was 1.327 cm^2. The schematic diagram of capacity measurement is shown in Figure 3.2b. The apparatus used in this experiment are listed as follows

- Regulator: Pressure regulator series YR-90 from Yamato Sangyo Co., Ltd.
- Flowmeter: Flowmeter with precision needle valve model RK1200 series from Kojima Instruments Inc. made from SUS316 was used.
- Aluminium cell box: 8×3.5×6 cm aluminium cell box was connected with temperature controller.
- Silica gel: Silica gel beats with 4 to 6 mm diameter was put inside aluminium cell box to decrease effect of humidity during measurement
- Potentiostat/Galvanostat: Chronopotentiometry function in VersaSTAT3-200, Princeton Applied Research was applied to measure capacity of Li-air battery
- Coin cell holder: CR2032 coin cell holder series BH-2032-25 from Battery Space was employed.
- Temperature controller: Catridge heater with temperature controller wasa used to control temperature of aluminium cell box.

3.3 Results and discussion

3.3.1 Morphology and properties of electrodes

The appearance, cross-sectional and surface observation of carbon electrode by SEM are shown in Figure 3.3. It can be clearly seen in Figure 3.3a that electrode fabricated by evaporation was disrupted, while cross-sectional SEM image implies that cathode was shrunk. Moreover, surface SEM image indicates that carbon particle in composite from evaporation aggregated together, providing size of macro pore smaller than 500 nm. On the other hand, Figure 3.3b and c indicates that electrodes fabricated by sc-CO_2 fluid have self-standing structure. Cross-sectional SEM images reveals that composites fabricated by sc-CO_2 were thick comparing to composites fabricated by evaporation. Additionally, surface SEM images implies that carbon particle in composites fabricated from sc-CO_2 fluid provide highly porous structure with macro pore size larger than 1 μm. The difference between structure of composites fabricated by evaporation and sc-CO_2 fluid can be explained from stress on capillary surface between organic solvent and carbon particle. In term of evaporation, NMP solvent alters its phase from liquid to vapor which cause capillary stress due to phase transition. After evaporation, pore network among carbon particle is collapsed, pulling partile together which finally cause shrinkage of composite. On the contrary, NMP solvent can form homogeneous phase and be miscible in sc-CO_2 fluid. This phenomenon can be optically observed in Chapter 2. The stress from capillary surface is considered to be extremely low comparing to evaporation due to no phase transition of organic solvent. As a result, pore network is not collapsed during solvent elimination and depressurization.

The properties of composites are summarized in Table 3.1. Porosity of composite fabricated from evaporation was 58.3 % with 140 μm thickness, while porosities of composites from sc-CO_2 was higher than 90.0 % and has thickness over 700 μm. Eventhough difference of morphology due to variation of pressure cannot be clarified from SEM images, results from Table 3.1 implies that porosity of composites increases as elevation of sc-CO_2 pressure. It can be seen from Chapter 2 that NMP spends shorter time to form homogeneous phase with sc-CO_2 fluid in higher pressure condition.
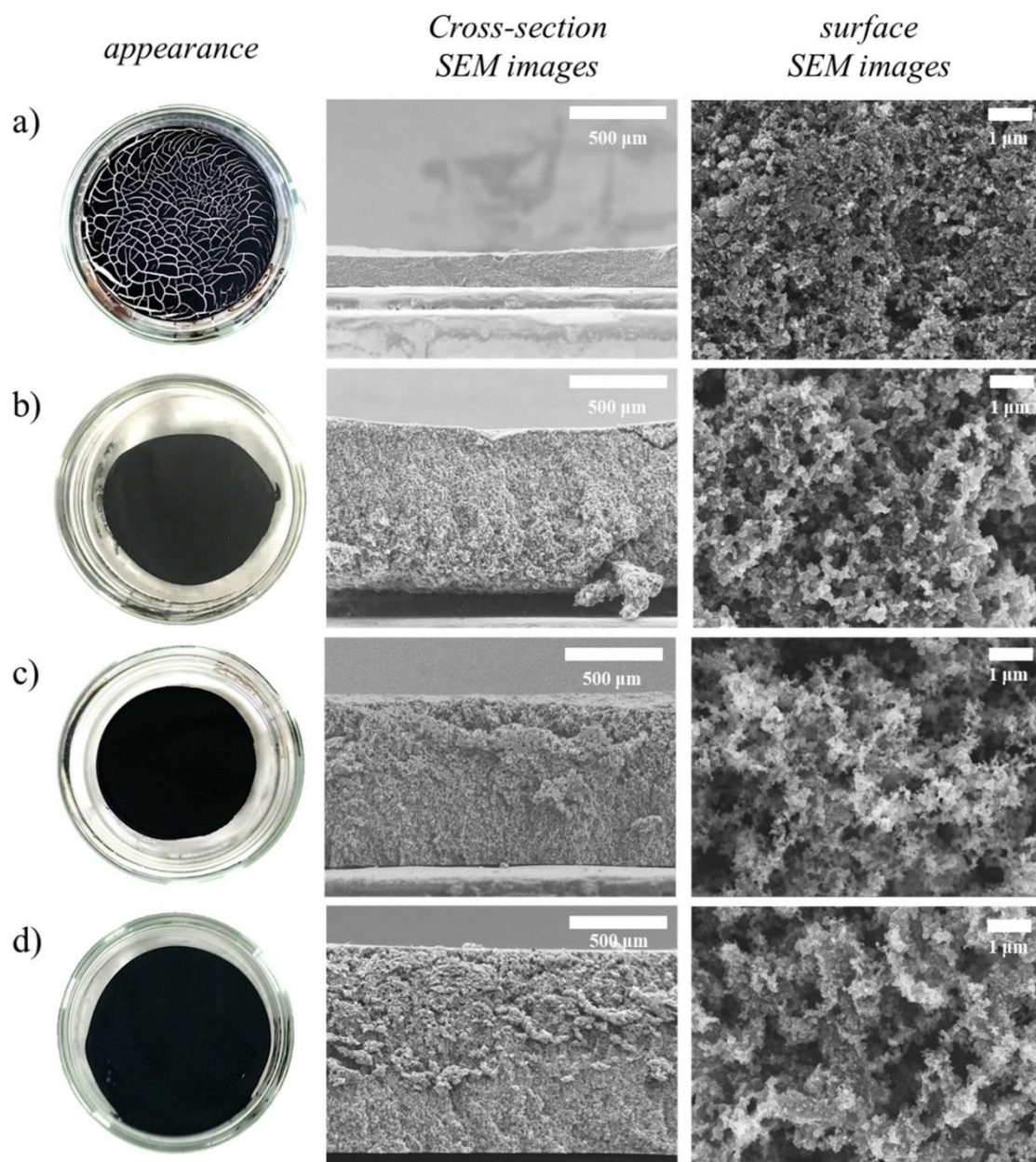
Figure 3.3 Appearance, cross-section SEM images and surface SEM images of electrodes fabricated by a) evaporation at 80 ℃, b) sc-CO_2 at 10.0 MPa, 40 ℃, c) sc-CO_2 at 15.0 MPa, 40 ℃ and d) sc-CO_2 at 20.0 MPa, 40 ℃. Weight ratio of CB to PVDF was controlled as 1.5.

Table 3.1 Porosity and sheet conductivity of electrodes.

CB:PVDF (weight)	Drying condition	Thickness (μm)	Porosity (-)	Sheet conductivity (S cm^{-1})
1.5	Evaporation (80 ℃)	140.48	0.583	-
1.5	Sc-CO$_2$ (10 MPa, 40 ℃)	746.40	0.902	8.699×10^{-2}
1.5	Sc-CO$_2$ (15 MPa, 40 ℃)	765.40	0.924	3.678×10^{-2}
1.5	Sc-CO$_2$ (20 MPa, 40 ℃)	902.08	0.942	2.070×10^{-2}

*Density of CB = 2.023 g cm^{-3}, PVDF = 1.648 g cm^{-3}

This can be considered that capillary stress due to liquid-vapor phase transition could be occurred before complete homogeneous phase formation. This capillary stress is considered to be lower in term of higher sc-CO_2 pressure due to shorter homogeneous phase formation time, providing composites with comparatively high porosity. The promotion of porosity can be explained from larger diffusion of sc-CO_2 into NMP. Since molar amount of sc-CO_2 fluid increases as the increment of pressure, NMP could expand in higher rate due to higher diffusion of sc-CO_2 fluid. Then after NMP is eliminated, higher porosity and thicker electrode could be fabricated when applying higher sc-CO_2 pressure as seen in Table 3.1.

Sheet conductivity of composites was also measured and summarized in Table 3.1. Sheet conductivity of composite from evaporation could not be measured due to disruption of composite. Sheet conductivity of composites fabricated from sc-CO_2 fluid reduced with increment of sc-CO_2 pressure. It can be explained that the volume of void space which is non-conductive spot is larger as porosity increases. Thus, sheet conductivity of material decreases with elevation of porosity which affected from increment of supercritical drying pressure. Another reason regarding to decline of sheet conductivity could be considered from swelling of polymer and changing of crystallinity, which was analyzed by TG and XRD. The results of TG and XRD are shown in Figure 3.4 and 3.5. The data obtained from XRD analysis is concluded in Table 3.2, while the crystallinity and DTG peak of composites are summarized in Table 3.3. Result from XRD show that composite fabricated by evaporation has larger crystallinity than composites fabricated from sc-CO_2 fluid. This conforms with result from TG that composite fabricated by evaporation has larger peak of DTG than composite fabricated by sc-CO_2 fluid. This can be interpreted that heating from evaporation causes stretching of polymer chain which increase crystallinity of composite [101]. Therefore, composite could have lower crystallinity since fabrications of composite by sc-CO_2 fluid were conducted in lower temperature. Moreover, crystallinity of composite was promoted as fabrication method varied from evaporation to sc-CO_2 fluid. It was previously reported PVDF was swollen 8.7 % in 11.6 MPa, 40 °C of sc-CO_2 fluid [102]. The swelling of PVDF from CO_2 absorption are taken place only in the amorphous phase of PVDF due to impermeability of CO_2 in crystalline phase of PVDF [103, 104]. This leads to the reduction of crystalline
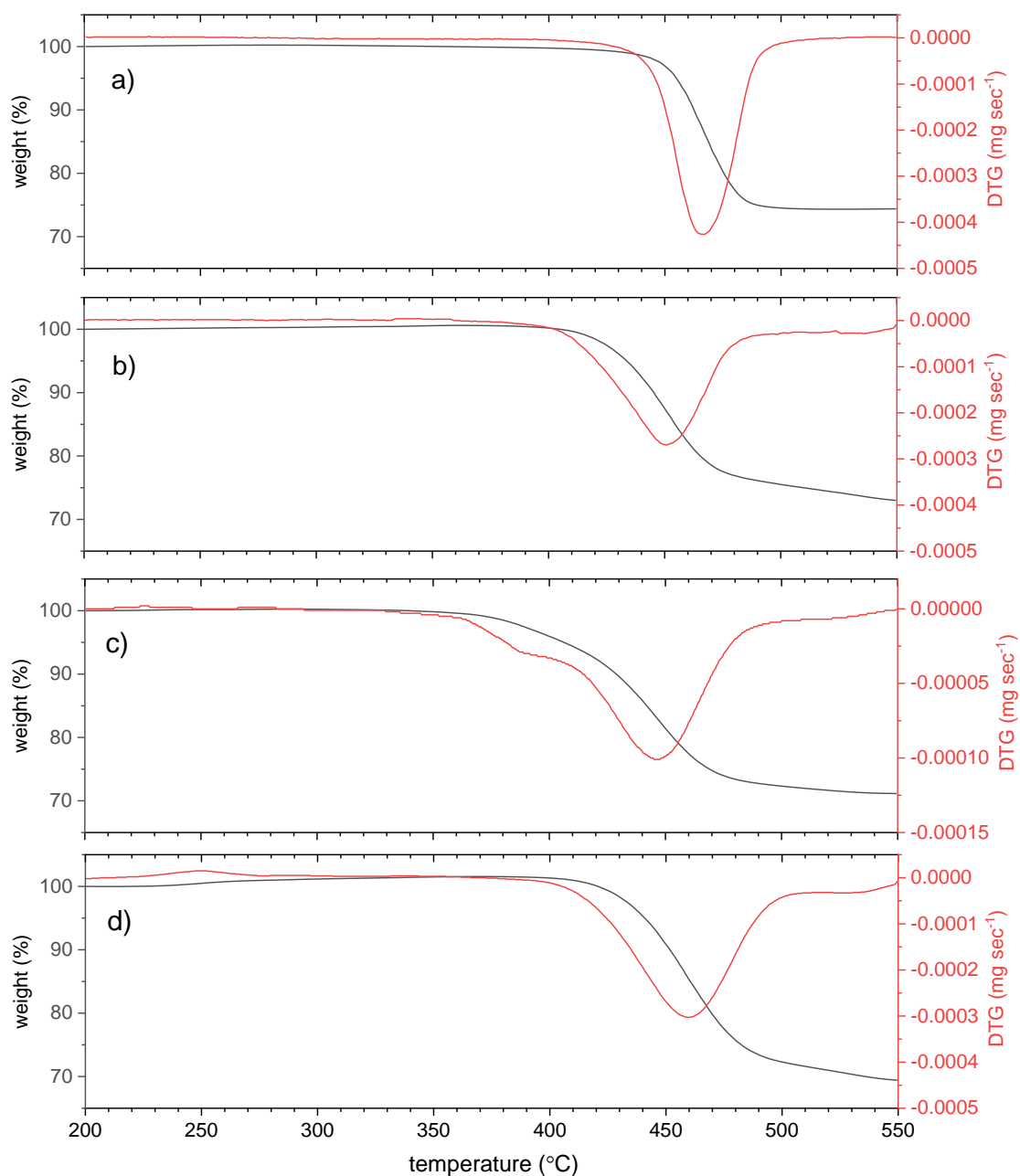
Figure 3.4 Thermogravimetric and derivative thermogravimetric profiles of electrodes fabricated by a) evaporation at 80 ℃, b) sc-CO_2 at 10.0 MPa, 40 ℃, c) sc-CO_2 at 15.0 MPa, 40 ℃ and d) sc-CO_2 at 20.0 MPa, 40 ℃. Weight ratio of CB to PVDF was controlled as 1.5.
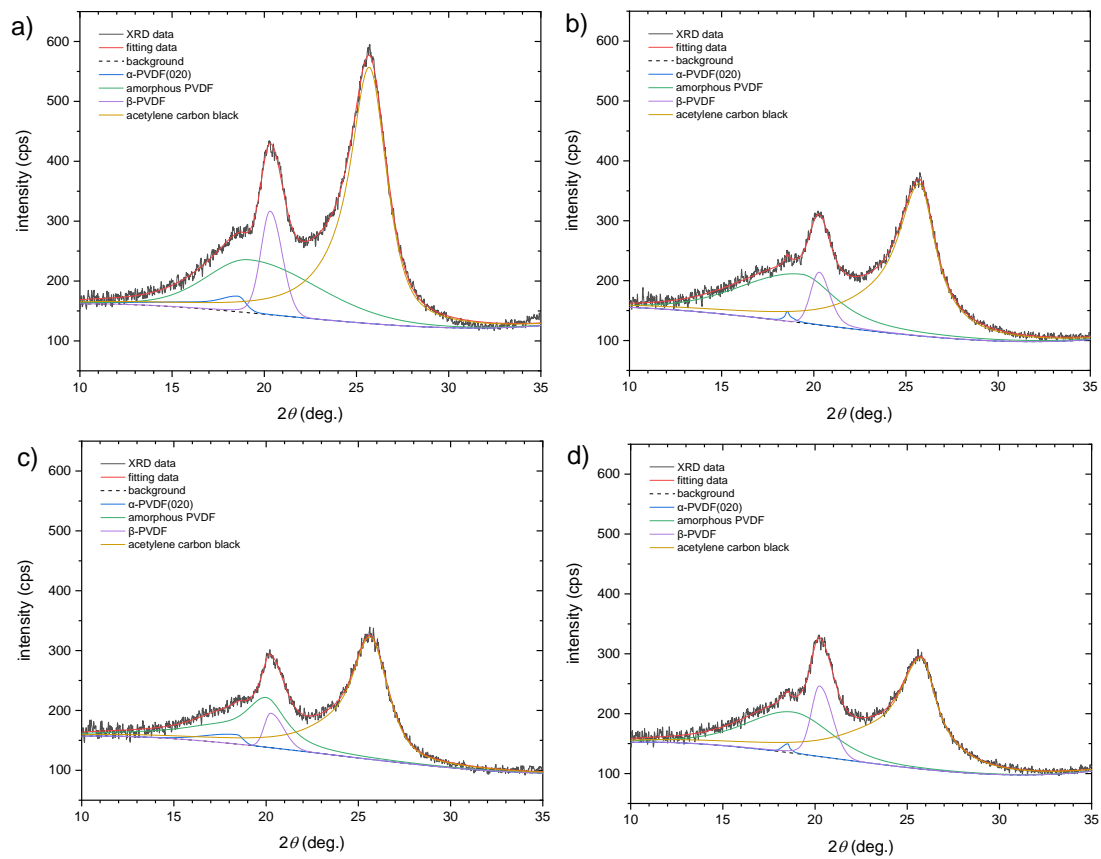
Figure 3.5 X-ray diffraction analysis results of electrodes fabricated by a) evaporation at 80 ºC, b) sc-CO_2 at 10.0 MPa, 40 ºC, c) sc-CO_2 at 15.0 MPa, 40 ºC and d) sc-CO_2 at 20.0 MPa, 40 ºC. Weight ratio of CB to PVDF was controlled as 1.5.

Table 3.2 Data from X-ray diffraction analysis of PVDF in each electrode

phase	2θ (deg)	peak height (cps)	FWHM (deg)	integral intensity (cps·deg)
CB/PVDF electrode fabricated from evaporation				
α-PVDF	18.56	17.41	2.20	69.33
amorphous PVDF	19.14	59.16	7.11	483.82
β-PVDF	20.30	115.66	1.36	174.37
carbon black	25.67	285.98	2.45	1067.57
CB/PVDF electrode fabricated from sc-CO₂ 10.0 MPa, 40 ºC				
α-PVDF	18.53	11.52	0.29	6.71
amorphous PVDF	19.33	54.22	6.13	419.57
β-PVDF	20.28	58.89	1.23	83.74
carbon black	25.72	169.96	2.67	764.05
CB/PVDF electrode fabricated from sc-CO₂ 15.0 MPa, 40 ºC				
α-PVDF	18.40	10.47	2.35	26.18
amorphous PVDF	19.98	55.45	3.03	298.59
β-PVDF	20.23	38.45	1.24	50.77
carbon black	25.61	136.47	2.56	553.90
CB/PVDF electrode fabricated from sc-CO₂ 20.0 MPa, 40 ºC				
α-PVDF	18.53	9.68	0.46	5.72
amorphous PVDF	18.77	45.80	5.41	304.73
β-PVDF	20.22	78.74	1.35	118.91
carbon black	25.73	124.05	2.84	634.98

Table 3.3 Cystallinity and DTG peak of electrodes.

CB:PVDF (weight)	Drying condition	Crystallinity of PVDF	DTG peak (℃)
1.5	Evaporation (80 ℃)	0.335	466.36
1.5	Sc-CO_2 (10 MPa, 40 ℃)	0.177	450.80
1.5	Sc-CO_2 (15 MPa, 40 ℃)	0.205	446.08
1.5	Sc-CO_2 (20 MPa, 40 ℃)	0.290	459.66

phase of PVDF because amount of amorphase phase is comparatively larger from polymer swelling. It can be seen that crystallinity of polymer increased as pressure of sc-CO_2 elevated. This result conforms with previous work reported elsewhere [105, 106]. This is considered from anti-solvent effect of sc-CO_2 which causes crystallization of PVDF. This leads to the larger amount of PVDF is crystallized out from structure since sc-CO_2 fluid diffuses more in higher pressure condition of sc-CO_2. The result of TG analysis shows that tendency of DTG peak conforms with crystallinity of PVDF. It can be interpreted that crystalline polymer has higher thermal durability due to stronger bonding comparing to amorphous polymer. Therefore, structure of composite is considerably stronger when composite is fabricated from higher sc-CO_2 pressure condition.

3.3.2 Performance of Li-air battery

The composites composed of CB, PVDF and MnO_2 were used as the cathode of Li-air battery. CB content and pressure condition were varied to investigate effect of those parameters on performance of Li-air battery. Properties of electrodes together with fabricating conditions are summarized in Table 3.4, while surface SEM images of electrodes are shown in Figure 3.6. Porosity of electrode fabricated from evaporation was the lowest among all electrode. SEM image confirmed that carbon particles were aggregated on electrode fabricated from evaporation. This result is considered to be affected from stress on capillary surface as previously discussed in section 3.3.1. Moreover, Porosity of composites increased, and sheet conductivity decreased as pressure condition of sc-CO_2 incresed. This result conforms with previous result discussed in section 3.3.1 due to higher association of sc-CO_2 fluid. Porosity and sheet conductivity were found to be decreased as the reduction of CB content in composites. The reduction of porosity and conductivity could be explained that CB is conductive porous material, therefore reducing this material leads to the reduction of void space and conductive area in electrodes.

Table 3.4 Porosity and sheet conduvtivity of electrode for capacity test of Li-air batteries.

LAB No.	CB:PVDF:MnO$_2$ (weight)	Drying condition	Thickness (μm)	Porosity (-)	Sheet conductivity (S cm^{-1})
3-1	1.5:1.0:0.3	Evaporation (80 °C)	130.98	0.558	-
3-2	1.5:1.0:0.3	Sc-CO$_2$ (10 MPa, 40 °C)	585.79	0.870	1.103×10^{-1}
3-3	1.5:1.0:0.3	Sc-CO$_2$ (20 MPa, 40 °C)	1080.33	0.949	2.716×10^{-2}
3-4	1.0:1.0:0.3	Sc-CO$_2$ (10 MPa, 40 °C)	582.21	0.870	6.613×10^{-2}
3-5	1.0:1.0:0.3	Sc-CO$_2$ (20 MPa, 40 °C)	746.12	0.920	2.882×10^{-2}
3-6	0.5:1.0:0.3	Sc-CO$_2$ (20 MPa, 40 °C)	551.71	0.880	2.087×10^{-2}

*Density of CB = 2.023 g cm^{-3}, PVDF = 1.648 g cm^{-3}, MnO$_2$ = 5.026 g cm^{-3}
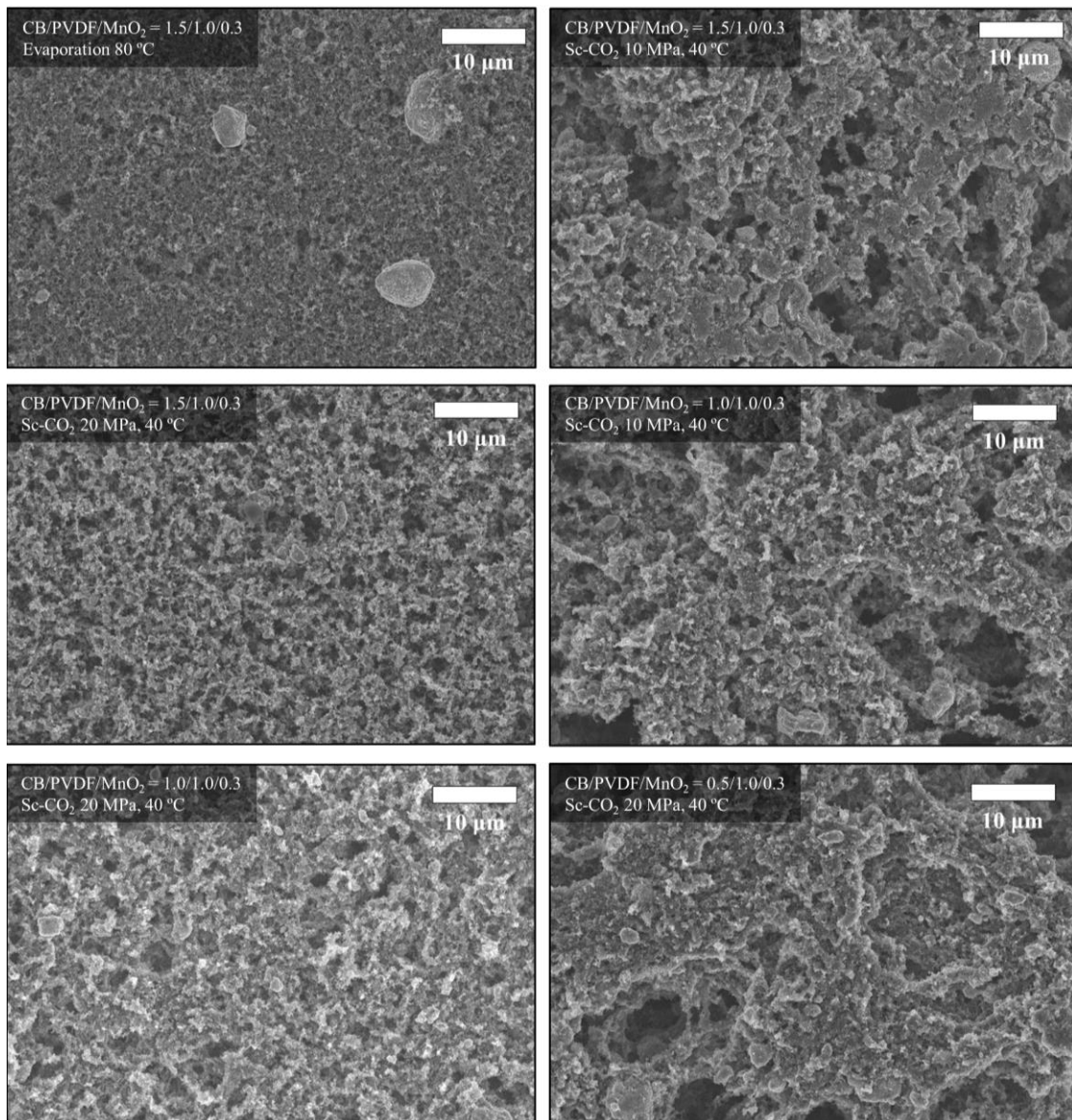
Figure 3.6 Scanning electron microscopy images of surface of pristine electrodes prepared for capacity test of Li-air battery.

The results of discharge-charge profiles of Li-air batteries for 3 cycles and plot of capacity against cycle number are shown in Figure 3.7 and 3.8. Li-air battery using cathode with CB:PVDF ratio as 1.5 and fabricated from evaporation provided initial discharge capacity of 0.2 mAh cm^{-2} as seen in Figure 3.8a, while Li-air battery using cathode fabricated from sc-CO_2 drying at 10.0 MPa and 20.0 MPa provided 1.1 and 4.4 mAh cm^{-2} as seen in Figure 3.8b and c, respectively. It can be seen that Li-air battery using cathode with higher porosity provides higher capacity. Normally, lithium-oxide discharge products are produced over surface of carbon cathode from oxygen reduction reaction between Li and O_2. The discharge product is considered to be non-conductive and insoluble in electrolyte, which leads to the pore blockage during discharge reaction. Consequently, Li-air battery with higher porosity is inclined to provide higher capacity because of the larger pore size for dispersion of reaction gas and larger pore volume for accumulation of discharge product. After reducing CB:PVDF from 1.5 to 1.0, Li-air battery using cathode fabricated from sc-CO_2 fluid at 10.0 MPa and 20.0 MPa provided initial discharge capacity at 1.3 mAh cm^{-2} and 8.4 mAh cm^{-2} as seen in Figure 3.8d and e, respectively. Li-air batteries using cathode with CB:PVDF ratio as 1.0 provided high initial discharge capacity than cathode with CB:PVDF ratio as 1.5 despite the reduction of porosity and sheet conductivity of cathode. This result is contrary to the assumption that capacity of Li-air battery is proposional to porosity of cathode. It is considered that cathode with lower CB:PVDF ratio has higher durability due to increment of binder content comparing to cathode with higher CB:PVDF ratio. The improvement of durability enhance cathode to withstand the stress inside cathode structure which is caused from growth of discharge product. Accordingly, durability of cathode is one of the factors that affects discharge capacity of Li-air battery. As CB:PVDF ratio was adjusted from 1.0 to 0.5, the initial discharge capacity of Li-air battery dropped to 0.54 mAh cm^{-2} as seen in Figure 3.8f. Despite the reduction of initial discharge capacity, this battery maintained its capacity in the 2nd and 3rd cycles. This implies that cathode with too low CB:PVDF ratio provides poor capacity due to reduction of porosity, however, the cyclability was improved by enhancement of durability. Accordingly, the optimization of porosity and durability of cathode is significant for designing Li-air battery with high performance and long-life.
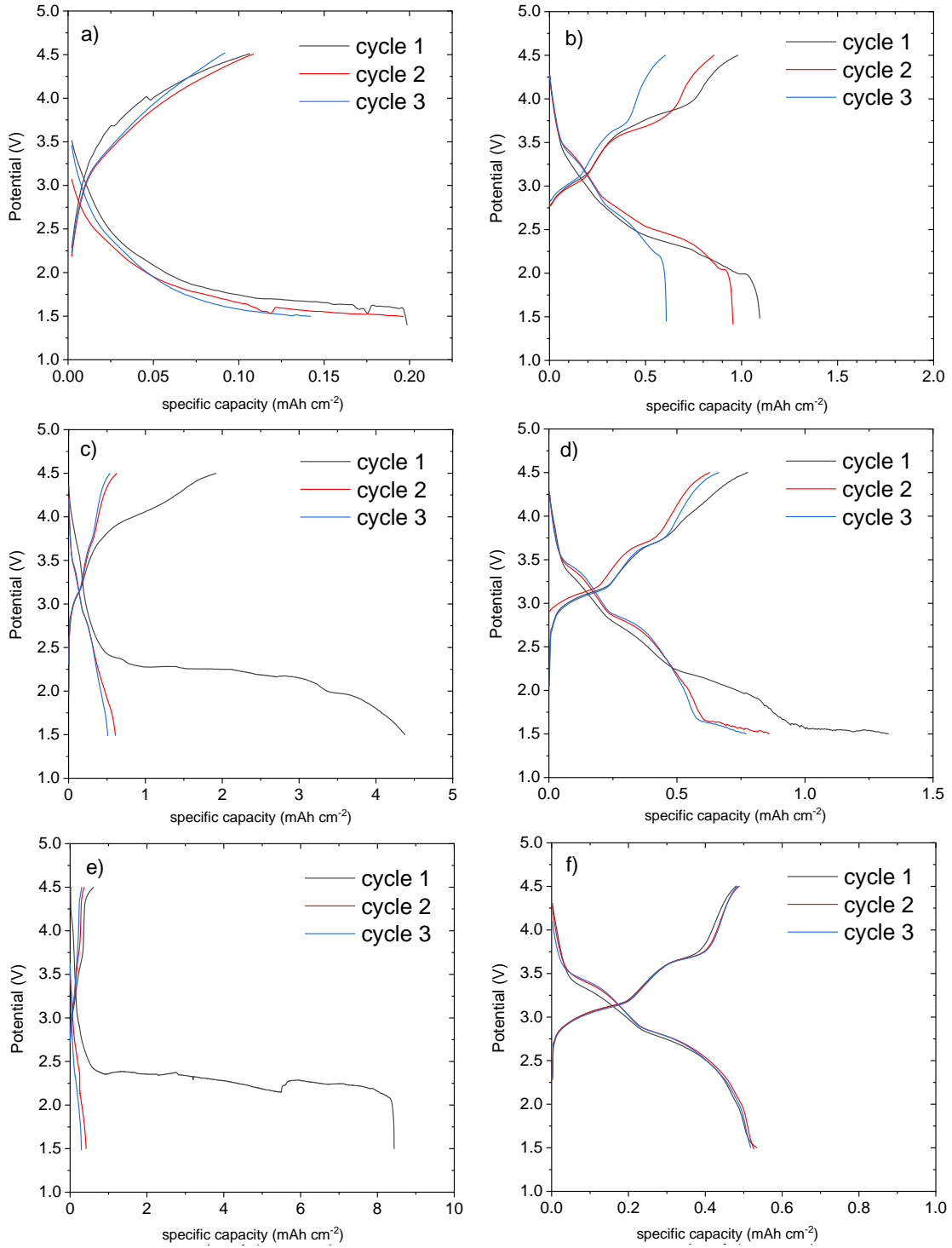
Figure 3.7 Discharge-charge profile of 3 initial cycles of a) LAB3-1, b) LAB3-2,
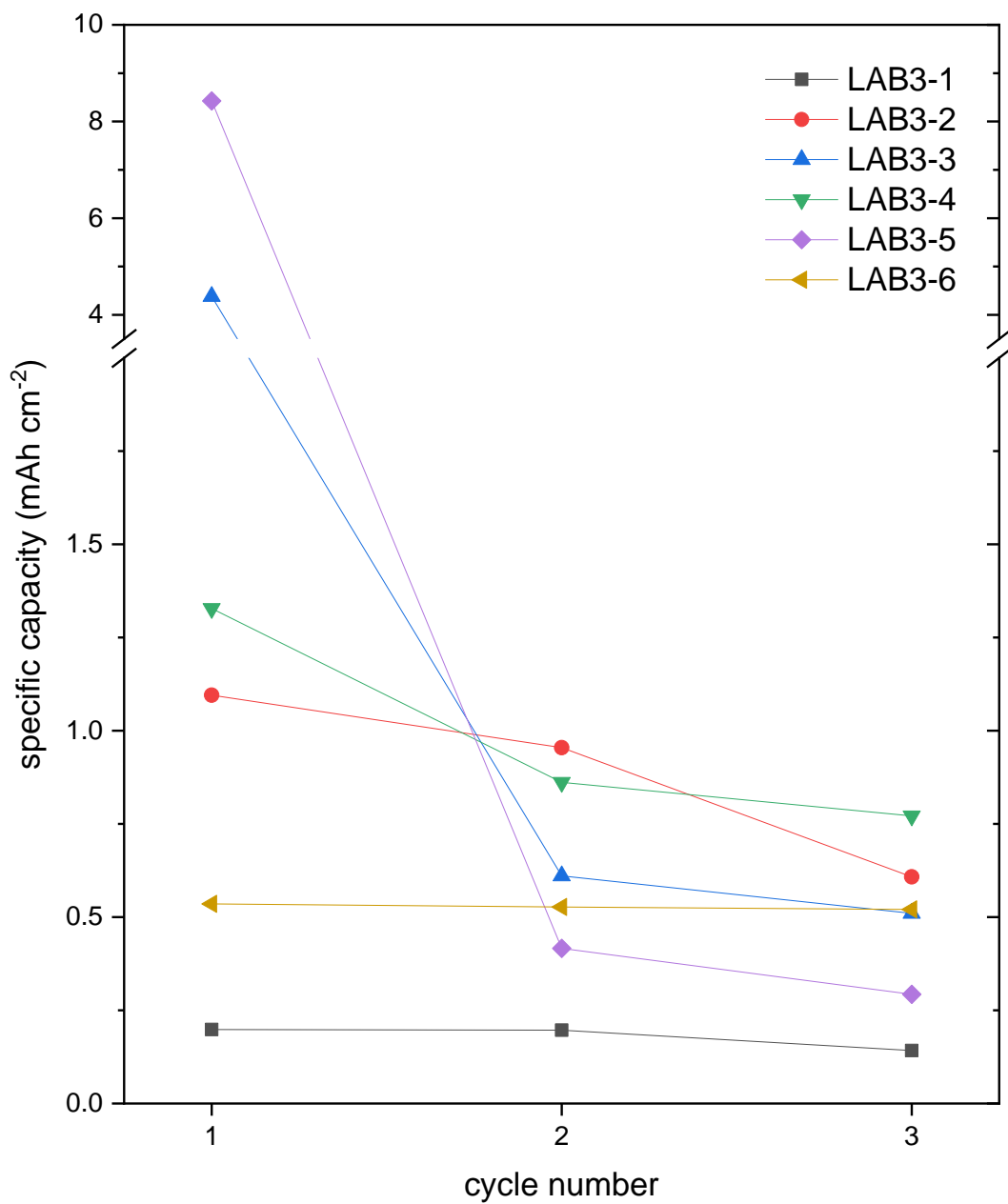c) LAB3-3, d) LAB3-4, e) LAB3-5 and f) LAB3-6.

Figure 3.8 Plot of cycle number with discharge capacity of Li-air batteries. Cut-off voltage for discharging was set at 1.5 V.

Chapter 4

Porous carbon electrode with ionogel binder
fabricated in supercritical carbon dioxide

4.1 Statement of problem and objectives

The rapid growth of world population leads to many problems including insufficient energy sources and pollutant. This urge us to find the new way to response to those problems. Li-O_2/CO_2 battery, one type of Li-air battery, employs electrochemical reaction between oxygen, carbon dioxide and lithium to generate electricity. Since carbon dioxide is captured to produce electricity during discharging process, Li-O_2/CO_2 battery is considered as the novel energy source which can reduce greenhouse gas and supply energy, simultaneously. One of the problems that limits performance of Li-O_2/CO_2 battery is from pore blocking of discharge product, lithium carbonate, after discharging process. Accordingly, cathode compartment of Li-O_2/CO_2 batteryhas to be developed to improve performance of battery.

The novel method to fabricate highly porous electrode by sc-CO_2 fluid is proposed in Chapter 3. It was found that this highly porous electrode improved performance of Li-air battery comparing to conventional fabrication method. However, polymer binder in cathode has defect on its non-conductive property, limiting transportation of ion and reactant during discharge process. Accordingly, improvement of polymer binder leads to the enhancement of battery performance. In this chapter, highly porous electrode fabricated by sc-CO_2 fluid was employed as cathode of Li-O_2/CO_2 battery. Moreover, IL was used as additive in polymer binder of cathode to enhance ionic conductivity and gas transfer inside the electrode during discharge process. The morphology and properties of electrodes were investigated. Electrodes were employed as cathode of Li-O_2/CO_2 battery and capacity of battery was tested to discuss the effects and functions of IL in cathode.

4.2 Experimental

4.2.1 Materials

Carbon dioxide (99.5 %) oxygen (99.7 %) were purchased from Fujii-bussan. Acetylene carbon black or CB (99.99 %) with 40 nm diameter was bought from Strem chemicals. Poly(vinylidene fluoride) or PVDF was obtained from Fluorochem. 1-methyl-2-pyrrolidone or NMP (99.0 %), mangenses(IV) Oxide or MnO_2, lithium bis(trifluoromethanesulfonyl)imide or LiTFSI (90.0 %) were purchased from Wako Chemicals. 1-butyl-3-methylimidazolium bis(trifluoromethylsulfonyl)imide or [bmim][Tf_2N] (98.0 %) was bought from Tokyo Chemical Industry. 1-butyl-3-methylimidazolium hexafluorophosphate or [bmim][PF_6] (98.0 %) was purchased from Merck. 1-butyl-3-methylimidazolium iodide or [bmim][I] was obtained from Wako. Dimethyl sulfoxide or DMSO (99.0 %) and tetraethylene glycol dimethyl ether or TEGDME (98.0 %) were purchased from Wako Chemicals and Alfa Aesar, respectively.

4.2.2 Fabrication of elctrode

4.2.2.1 Preparation of black viscous slurry

Black viscous slurry composed of CB, PVDF and MnO_2 was prepared as follows. Initially, PVDF was dissolved into NMP by ultra-sonication at 60 ℃ until polymer was fully dissolved. MnO_2 was added in this solution and dispersed by ultra-sonication at room temperature for 1 h. Then, carbon black was put into the solution and dispersed by ultra-sonication at room temperature for 1 h. The black viscous slurry was finally stirred by magnetic stirrer at room temperature for 12 h. Weight ratio of PVDF to CB, PVDF to MnO_2 and PVDF to NMP were fixed at 1.0, 0.3 and 13.5, respectively.

Black viscous slurry composed of CB, PVDF, MnO_2 and ionic liquid (IL) was prepared as follows. Initially, PVDF was dissolved into NMP by ultra-sonication at 60 ℃ until polymer was fully dissolved. IL was then added to the solution and stirred by magnetic stirrer for 30 minutes. After that, MnO_2 was added in this solution and dispersed by ultra-sonication at room temperature for 1 h. Then, carbon black was put into the solution and dispersed by ultra-sonication at room temperature for 1 h. The black viscous

slurry was finally stirred by magnetic stirrer at room temperature for 12 h. Weight ratio of PVDF to CB, PVDF to MnO_2 and PVDF to NMP were fixed at 1.0, 0.3 and 13.5, respectively. Weight ratio of IL to PVDF was varied as 0.2, 0.5, 1.0.
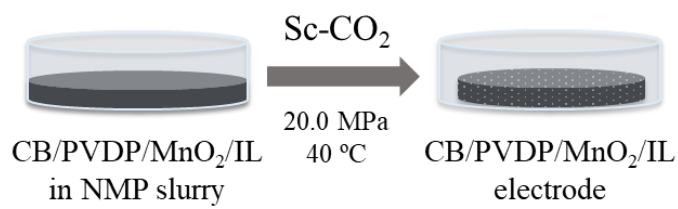
4.2.2.2 Drying of black viscous slurry

1.00 g of black viscous slurry was weighed and put in clean Petri dish (34.0 mm inner diameter). The Petri dish was tapped to spread out slurry uniformly. NMP in slurry was soon after eliminated by evaporation or sc-CO_2 fluid. In term of evaporation, the slurry was brought into thermostat which has temperature controlled at 80 ℃ for 12 h. sc-CO_2 fluid was used as solvent elimination and impregnation of IL. 1-step method and 2-step method of sc-CO_2 fluid was applied in this chapter. The apparatus used for cathode fabrication by sc-CO_2 fluid is previously shown in Figure 3.1.

1-step method of sc-CO_2 fluid was conducted as the same procedure stated in section 3.2.2.2. sc-CO_2 was flowed for 6 h, while pressure and temperature of the cell during the process were controlled at 20.0 MPa and 40 ℃, respectively. Flowrate of sc-CO_2 was controlled at approximately 6.0 mmol min^{-1}.

2-step method was applied to fabricate electrode with high weight ratio of ILto PVDF. 2-step method of sc-CO_2 fluid was initially conducted by the same procedure as 1-step method to eliminate NMP from slurry containing CB, PVDF and MnO_2. After solvent elimination, [bmim][Tf_2N] ionic liquid was dropped on the electrode equitably. Weight ratio of IL to PVDF in electrode was controlled as 6.0. The electrode was put in high-pressure cell which was prior kept at 40 ℃. The cell was then locked to prevent gas leakage. CO_2 was soon after flowed into the cell and pressurized until 15.0 MPa, 40 ℃. After pressure was reached, stop-valve before and after the cell were closed. After leaving for 1 h, stop-valve at the exit of the cell was opened to depressurize CO_2 until atmospheric pressure. Finally, the cell was opened to take electrode out from the cell. The schematic diagram explaining 1-step and 2-step method of sc-CO2 fluid is illustrated in Figure 4.1.

1-step method

Sc-CO$_2$
20.0 MPa
40 ℃

CB/PVDP/MnO$_2$/IL
in NMP slurry

CB/PVDP/MnO$_2$/IL
electrode

2-step method

IL dropping

Sc-CO$_2$
20.0 MPa
40 ℃

Sc-CO$_2$
15.0 MPa
40 ℃

CB/PVDP/MnO$_2$
in NMP slurry

CB/PVDP/MnO$_2$
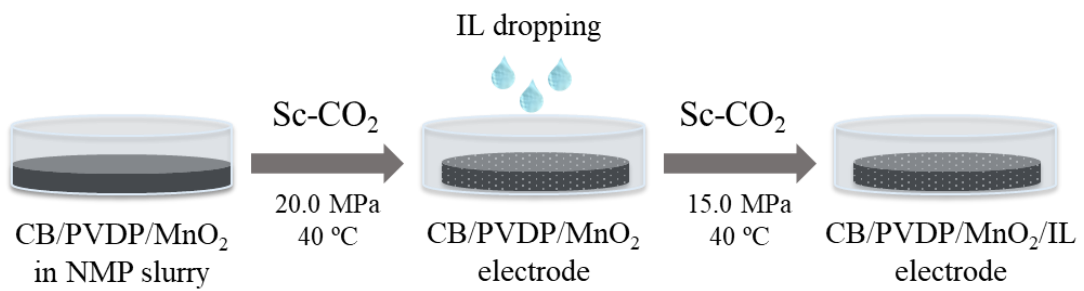electrode

CB/PVDP/MnO$_2$/IL
electrode

Figure 4.1 Schematic diagram of 1-step and 2-step method of supercritical carbon dioxide.

4.2.3 Characterization

4.2.3.1 Morphology investigation

Surface morphology of electrodes was investigated by field emission scanning electron microscope (FE-SEM) series S-4700 from Hitachi located in Technical Department, Ookayama Materials Analysis Division, Tokyo Institute of Technology. Accelerating voltage and beam current were set to 8.0 kV and 10.0 μA, respectively in all investigation.

4.2.3.2 Porosity measurement

Porosity of electrodes was calculated by equation (3.1). Same method as stated in section 3.2.3.2 was conducted to measure porosity of electrodes.

4.2.3.3 BET surface area

Specific surface area of carbon electrodes was measured from N_2 adsorption isotherms applying Brunauer-Emmett-Teller (BET) method using surface area analyser Gemini VII 2390 series (Micrometric). All electrodes were pre-heated at 200 °C for 1 h prior to the BET analysis to degas and eliminate impurities in the electrode.

4.2.3.4 Thermogravimetric analysis (TGA)

Thermogravimetric data were collected from thermogravimetric analyzer TGA-50 series (SHIMADZU). The heating rate was set to 3.0 °C min^{-1} from ambient temperature until 550.0 °C in all experiment. Further detail on data analysis from TGA results and derivation of DTG are stated in section 3.2.3.4.

4.2.3.5 Impedance spectroscopy

Impedance spectroscopy of the carbon electrodes was measured to investigate the ionic conductivity using a symmetric cell. The compositions of the symmetric cell are shown in Figure 4.2a. The apparatus used in this section is listed as follows,
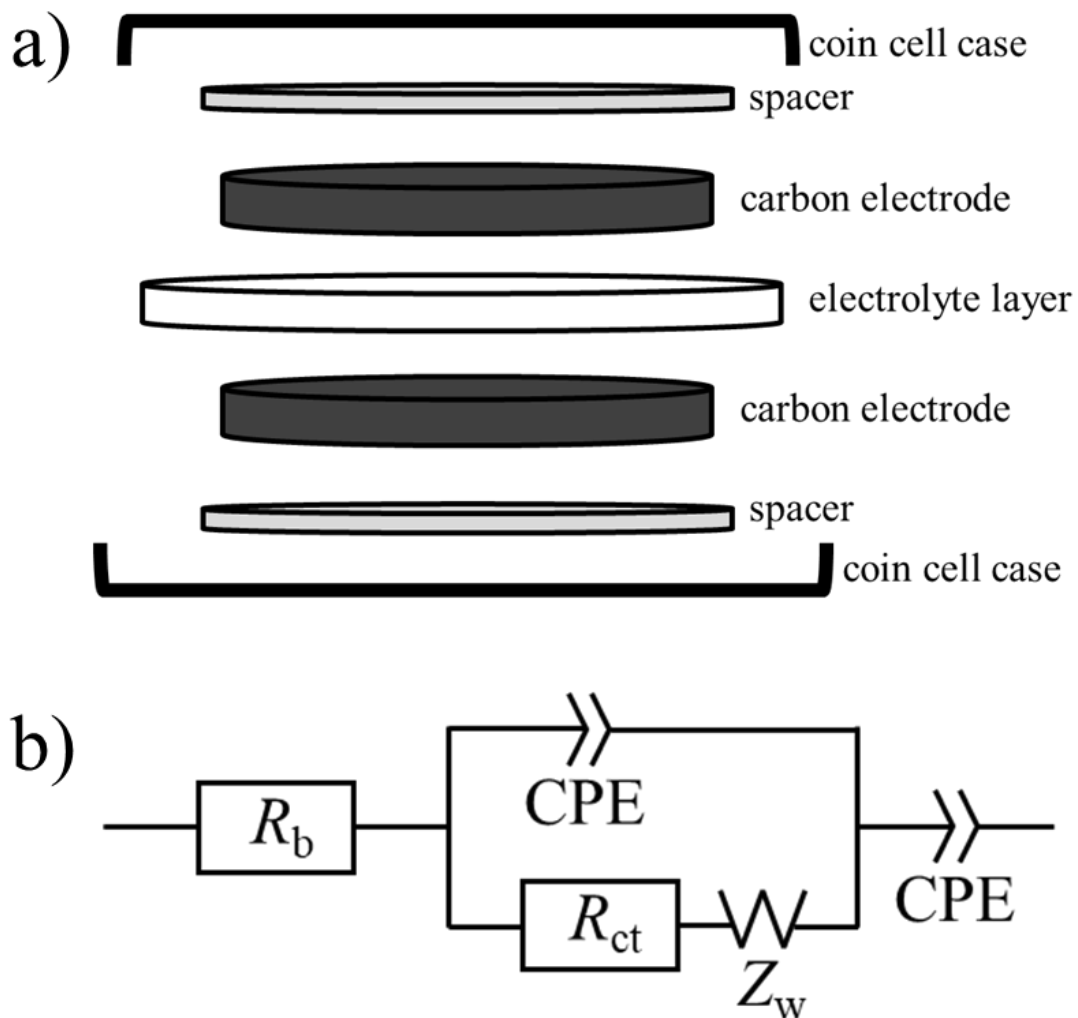
Figure 4.2 Schemicatic diagram of a) symmetric cell and b) equivalent circuit for impedance spectroscopy where R_b is bulk resistance, R_{ct} is charge transfer resistance, CPE is constant phase element and Z_w is Warburg impedance.

- Crimper: Hydraulic Crimper for CR2032 Case series MSK-110 from MTI corporation was used for coin cell crimping. All coin cells were crimped at 1000 psi.
- Coin cell case: CR2032 case series EQ-CR2032-CASE-316 from MTI corporation was employed. The case has 20 mm outer diameter and 15.8 mm inner diameter.
- Spacer: 304 Stainless Steel spacers with 15.5 mm diameter and 0.2 mm thickness were used in coin cell assembly.
- Separator: Whatman^{TM} glass microfiber filters GF/A (21 mm diameter, 260 μm thickness, 1.6 μm pore size) was used with electrolyte as a separator between Li metal and cathode in coin cell assembly.
- Coin cell holder: coin cell holder series BH-2032-25 from Battery Space was used.

The as-prepared electrodes were cut into two round disks with 13.0 mm diameter. 150 μl of 1.0 M LiTFSI in TEGDME was immersed in separator. this separator was sandwiched between two cut electrodes and put in coin cell case with spacers. The coin cell was soon after assembling by crimper. The assembled symmetric cell was put in coin cell holder connected to a chemical impedance analyser (IM3590, Hioki). Impedance spectroscopy of symmetric cell was measured in frequency range from 10000 Hz to 0.01 Hz at a voltage of 0.01 V. Determination of circuit elements was conducted by data regression with equivalent circuit shown in Figure 4.2b using Z fit function in *BT-lab* software version 1.52.

4.2.4 Battery performance test

4.2.4.1 Battery assembling

The same method and apparatus for battery assembling stated in section 3.2.4.1 are employed in this chapter.

4.2.4.2 Initial discharge capacity and cyclability test

Assembled meshed coin cell battery was locked into coin cell holder which is located inside aluminium cell box and connected with Potentiostat/Galvanostat.

Temperature of this box was controlled at 25 ºC. Mixing gases of O_2 and CO_2 was flowed into the box. Flow rate of each gases was set to the same level at 50 ml min^{-1}, 1 bar. volumetric ratio of O_2 and CO_2 was set to 1.0. capacity of electrode was then measured by Potentiometry function in Potentiostat/Galvanostat. The current was fixed at 0.1 mA (0.075 mA cm$^{-2}_{cathode}$) in all measurement. Initial discharge capacity was measured by pre-charging the battery until 4.0 V and then discharged the battery until 2.0 V. The initial discharge capacity was determined by the capacity of battery at the cut-off voltage. specific capacity was calculated from cathode surface area, which was 1.327 cm^2. Cyclability of battery was tested by discharging and charging battery until 0.5 mAh cm^{-2} for many cycles. Cut-off voltage for discharging was set at 2.0 V in all cyclability test. The apparatus used for battery test are listed in section 3.2.4.2 where air cylinder was changed to oxygen and carbon dioxide cylinders. Oxygen cylinder (99.7 %) and liquidified carbon dioxide cylinder (99.5 %) were purchased from Fujii-Bussan. The scemetic diagram of Li-O_2/CO_2 battery test is shown in Figure 4.3.

4.2.4.3 Investigation of electrode after discharge

The discharged coin cells were disassembled in argon filled globe box by decrimper. The apparatus used for disassembling are listed as follows,

- Glovebox: Large-scale glove box ($800 \times 600 \times 620$ mm) was obtained from AS ONE Corporation. argon gas was filled in the glovebox prior to battery assembling
- Argon gas: Purity 99.99% Argon gas was bought from Fujii-Bussan
- Decrimper: Hydraulic Crimper for CR2032 Case series MSK-110D from MTI corporation was used for decrimping the coin cells.
- Humidity meter: Temperature/humidity meter from AS ONE Corporation was used in glove box. Minimum relative humidity which can be detected is 5 %.

Morphology of discharged electrode was investigated by field emission scanning electron microscope (FE-SEM) series JSM-7500F from JEOL located in Technical Department, Ookayama Materials Analysis Division, Tokyo Institute of Technology. Discharged product in electrode was confirmed by benchtop powder X-ray diffraction (XRD) instrument series Mini Flex 600 from Rigaku. XRD was scanned from 20.0 to 60 .0degree at scanning rate of 1 degree min^{-1}.
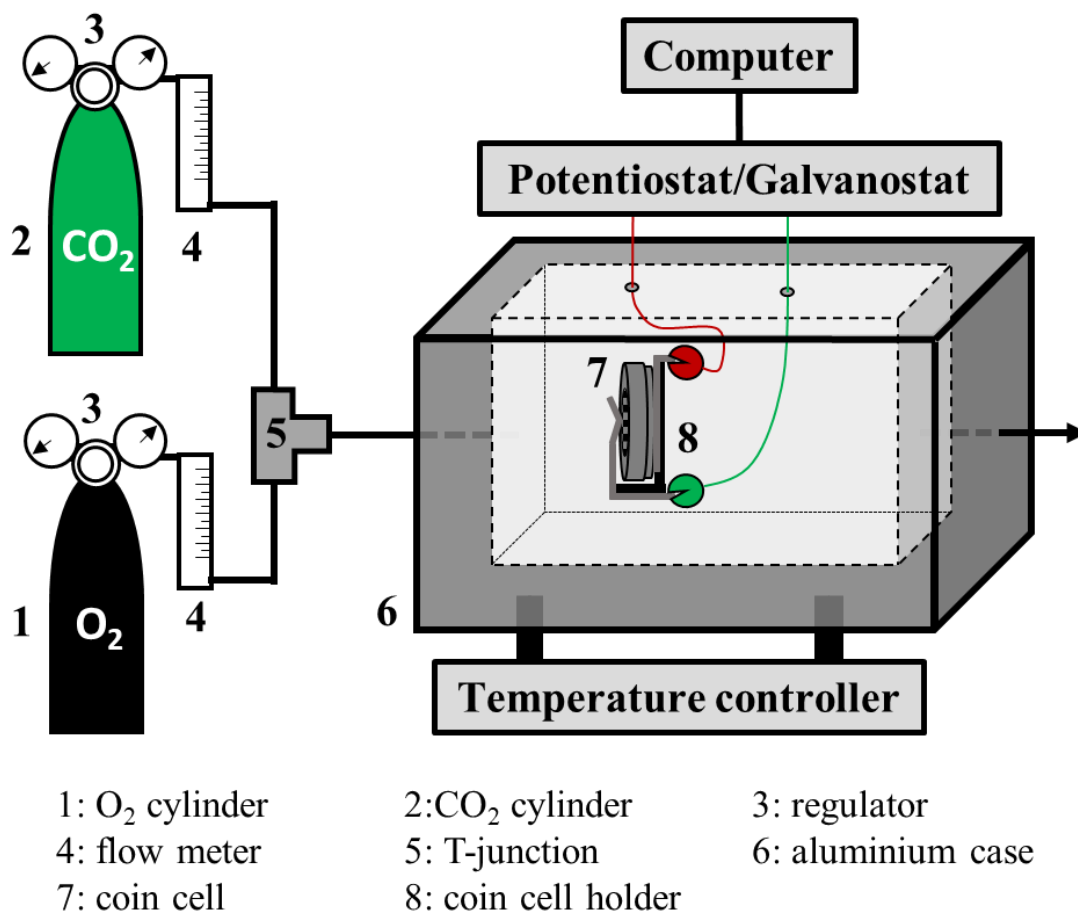
1: O_2 cylinder   2: CO_2 cylinder   3: regulator
4: flow meter   5: T-junction   6: aluminium case
7: coin cell   8: coin cell holder

Figure 4.3 Schematic diagram of apparatus for capacity measurement of Li-O_2/CO_2 battery.

4.3 Solubility calculation of O_2 and CO_2 in ionic liquid by COSMO-SAC method

4.3.1 Solubility calculation

Solublity of oxygen and carbon dioxide in pure ionic liquids (IL) was calculated and used in consideration of reaction gases solubility in ionogel binder. The solubility of vapor component in IL was derived from vapor-phase equilibria of O_2 + IL and CO_2 + IL system. Since IL has nearly zero vapor pressure, O_2 or CO_2 was assumed as the only component existed in vapor phase [107]. Solubilities of O_2 or CO_2 in IL can be calculated from following equation,

$$x_i = \frac{P_{tot}}{\gamma_i f_i^{ref}}$$

(4.1)

where, P_{tot} is total pressure at 1.0 bar, γ_i is activity coefficient of O_2 or CO_2, f_i^{ref} is fugacity of O_2 or CO_2 in IL at standard state. solubility data of O_2 and CO_2 in [bmim][PF$_6$] at 283 to 343 K [108] was used to find the temperature dependence of fugacity at standard state. The temperature dependence after regression with experimental data can be shown as follows,

$$\ln f_{CO_2}^{ref} = -\frac{1765.3}{T} + 10.259$$

(4.2)

$$\ln f_{O_2}^{ref} = -\frac{1261.4}{T} + 10.958$$

(4.3)

where T (K) is system temperature. The temperature in solubility calculation was set to 298.15 K, which was the temperature during battery performance test.

4.3.2 COSMO-SAC method

Activity coefficient in equation (4.1) was derived from COSMO-SAC (conductor like screening model of segment activity coefficient) method [90]. Initially, molecular structure of O_2, CO_2 and IL were optimized using *TmoleX* software version 3.3. def-SV(P) and Hatree-Fock were used as basis function and level of theory, respectively. The sigma

profile of single molecule was calculated from surface charge density profile extracted from software. The molecular surface charge density to find charge segment σ_m in mixture or $P_S(\sigma_m)$ can be expressed as follows,

$$P_S(\sigma_m) = \frac{\sum x_i A_i P_i(\sigma_m)}{\sum x_i A_i} \tag{4.5}$$

where x_i is mole fraction of molecule i in mixture. $P_i(\sigma_m)$ can be derived from equation (2.4) stated in section 2.2.4. The segment activity coefficient of mixture $\Gamma_S(\sigma_m)$ and pure component $\Gamma_i^o(\sigma_m)$ are derived from following equation [90],

$$\ln \Gamma_S(\sigma_m) = -\ln\left\{\sum_{n=1}^{k} P_S(\sigma_n)\Gamma_S(\sigma_n)\exp\left[\frac{-\Delta W(\sigma_m,\sigma_n)}{RT}\right]\right\} \tag{4.6}$$

$$\ln \Gamma_i^0(\sigma_m) = -\ln\left\{\sum_{n=1}^{k} P_i(\sigma_n)\Gamma_i^0(\sigma_n)\exp\left[\frac{-\Delta W(\sigma_m,\sigma_n)}{RT}\right]\right\} \tag{4.7}$$

Exchange energy $\Delta W(\sigma_m, \sigma_n)$ is exchange energy which can be derived from following equation,

$$\Delta W(\sigma_m,\sigma_n) = \left(\frac{0.64 \times 0.3 \times a_{\text{eff}}^{3/2}}{2\varepsilon_0}\right)(\sigma_m+\sigma_n)^2 + c_{\text{hb}}\max[0,\sigma_{\text{acc}}-\sigma_{\text{hb}}]\min[0,\sigma_{\text{don}}-\sigma_{\text{hb}}] \tag{4.8}$$

where a_{eff} is standard surface area, ε_0 is permittivity of free space, c_{hb} is constant for interaction of hydrogen bonding, σ_{hb} is cut-off value for hydrogen bonding interaction, σ_{acc} and σ_{don} are accepter and donor charge segment, which are larger and smaller values of σ_m and σ_n. In this work, $a_{\text{eff}} = 7.50$ Å^2, $\varepsilon_0 = 2.359 \times 10^{-4}$ e^2 mol kcal^{-1} Å^{-1}, $c_{\text{hb}} = 85580$ kcal Å^4 mol^{-1} e^{-2} and $\sigma_{\text{hb}} = 0.0084$ e Å^{-2} were used. Finally, activity coefficient can be derived from following equation using segment activity coefficient,

$$\ln(\gamma_i) = \ln \gamma_i^C + \frac{A_i}{a_{\text{eff}}} \sum_{\sigma_m} P_i(\sigma_m)[\ln \Gamma_S(\sigma_m) - \ln \Gamma_i^0(\sigma_m)] \tag{4.9}$$

The combinatorial term of activity coefficient γ_i^C can be derived from Staverman-Guggenheim equation [109, 110], which can be shown as following equations,

$$\gamma_i^C = \ln \frac{\phi_i}{x_i} + \frac{z}{2} q_i \ln \frac{\theta_i}{\phi_i} + l_i - \frac{\phi_i}{x_i} \sum_j x_j l_j \tag{4.10}$$

$$\theta_i = \frac{x_i q_i}{\sum_j x_j q_j} \tag{4.11}$$

$$\phi_i = \frac{x_i r_i}{\sum_j x_j r_j} \tag{4.12}$$

$$l_i = \frac{z}{2}[(r_i - q_i) - (r_i - 1)] \tag{4.13}$$

$$r_i = \frac{V_i}{V_{\text{st}}} \tag{4.14}$$

$$q_i = \frac{A_i}{A_{\text{st}}} \tag{4.15}$$

V_i and A_i are volume and surface of molecule i, respectively. V_{st} and A_{st} are standard volume and surface area, respectively. z is coordination number. $V_{\text{st}} = 66.69$ Å^3, $A_{\text{st}} = 79.53$ Å^2 and $z = 10$ were used in this work.

4.4 Results and discussion

4.4.1 Morphology and properties of electrodes

The composition, fabrication method, porosity and BET surface area of electrodes are summarized in Table 4.1. Porosity of electrode fabricated from evaporation method was 0.382, while porosity of electrode fabricated from sc-CO_2 was 0.920. The Increment of porosity is considered from less stress on capillary surface due to liquid-vapor phase transition, which is discussed in section 3.3.1. However, BET surface area of both electrodes shows no large difference. This result implies that sc-CO_2 fluid method is ineligible to increase surface area of electrode because the same composition and material was employed in both electrodes. After adding [bmim][Tf$_2$N] in slurry and fabricating electrode by sc-CO_2 fluid, porosity and BET surfacea area of electrode decreased as content of [bmim][Tf$_2$N] increased. The same result was also obtained after employing [bmim][PF$_6$] and [bmim][I] in slurry. Morphology of electrode with only PVDF and electrode with IL:PVDF weight ratio as 1.0 and fabricated by 1-step sc-CO_2 method are shown in Figure 4.4a and b. No morphological difference was observed despite the difference of porosity and BET surface area of both electrodes. The electrode with [bmim][Tf$_2$N]:PVDF weight ratio as 6.0 and fabricated by 2-step sc-CO_2 method provided 0.520 porosity and 0.84 m^2 g^{-1} BET surface area, which was the lowest value among all electrodes fabricated by sc-CO_2 fluid. Morphology of this electrode is shown in Figure 4.4c. It can be seen that large amount of IL was covered over the nanoparticle structure in electrode.

Thermogravimetric analysis was employed for consideration of compatibility between PVDF and IL. TG and DTG results of pure components and electrodes are shown in Figure 4.5 and 4.6, respectively. The electrode with only PVDF binder lost 30 % of its initial weight at 550.0 ℃ as seen in Figure 4.6a. Moreover, as weight ratio of [bmim][Tf$_2$N]:PVDF increased to 0.2, 0.5 and 1.0, weight loss in electrode increased to 34, 37 and 43 %, respectively as shown in Figure 4.6b to d. Accordingly, weight loss of electrode during TG analysis is contributed to the decomposition of PVDF and IL.

Table 4.1 Composition, fabrication method and properties of electrodes.

electrode	Compositions of electrode	Fabrication method	IL:PVDF (weight ratio)	Porosity	BET (m^2 g^{-1})
CFMn_E	CB/PVDF/MnO$_2$	Evaporation	-	0.382	11.97
CFMn_SC-1	CB/PVDF/MnO$_2$	scCO$_2$ (1-step)	-	0.920	13.95
CFMn0.2BT_SC-1	CB/PVDF/MnO$_2$/[bmim][Tf$_2$N]	scCO$_2$ (1-step)	0.2	0.916	12.75
CFMn0.5BT_SC-1	CB/PVDF/MnO$_2$/[bmim][Tf$_2$N]	scCO$_2$ (1-step)	0.5	0.895	9.57
CFMn1.0BT_SC-1	CB/PVDF/MnO$_2$/[bmim][Tf$_2$N]	scCO$_2$ (1-step)	1.0	0.830	5.68
CFMn1.0BP_SC-1	CB/PVDF/MnO$_2$/[bmim][PF$_6$]	scCO$_2$ (1-step)	1.0	0.808	6.08
CFMn1.0BI_SC-1	CB/PVDF/MnO$_2$/[bmim][I]	scCO$_2$ (1-step)	1.0	0.821	7.98
CFMn6.0BT_SC-2	CB/PVDF/MnO$_2$/[bmim][Tf$_2$N]	scCO$_2$ (2-step)	6.0	0.520	0.84

*weight ratio of CB:PVDF:MnO$_2$ = 1.0:1.0:0.3 for all electrodes

*porosity was calculated from density of CB = 2.023 g cm^{-3}, PVDF = 1.648 g cm^{-3}, MnO$_2$ = 5.026 g cm^{-3}, [bmim][Tf$_2$N] = 1.44 g cm^{-3}, [bmim][PF$_6$] = 1.38 g cm^{-3}. [bmim][I] = 1.46 g cm^{-3}
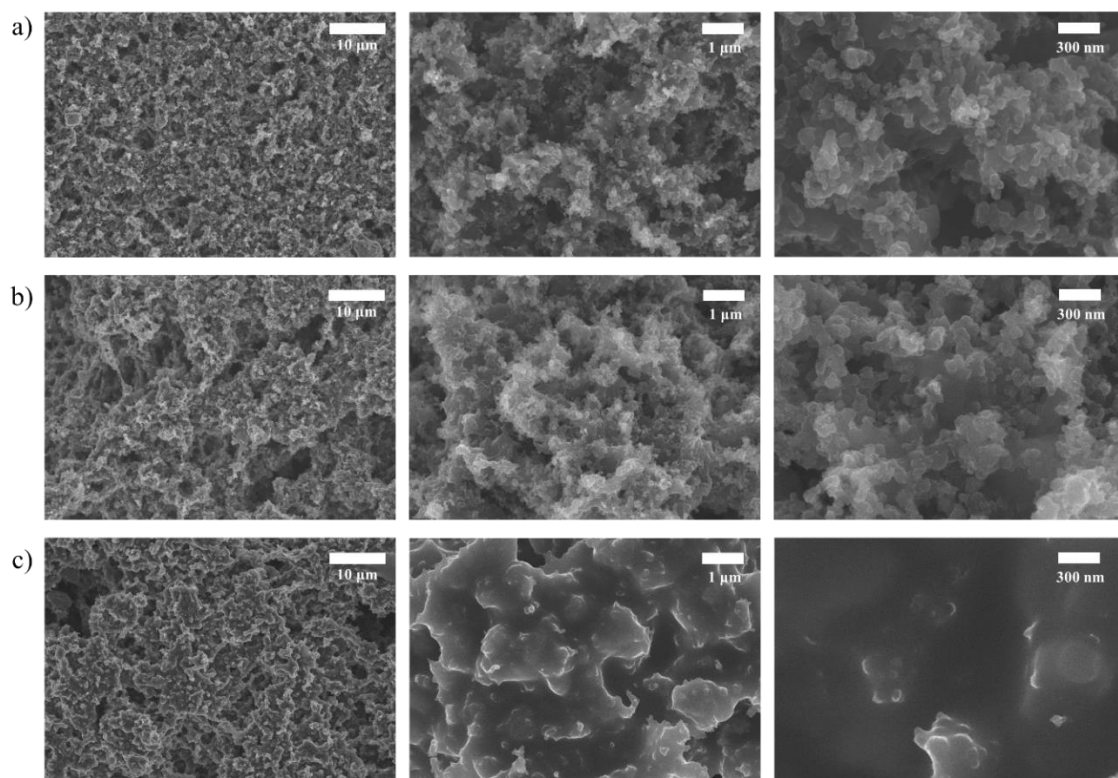
Figure 4.4 Scanning electron microscopy images of surface of a) CFMn_SC-1, b) CFMn1.0BT_SC-1 and c) CFMn6.0BT_SC-2 electrode.
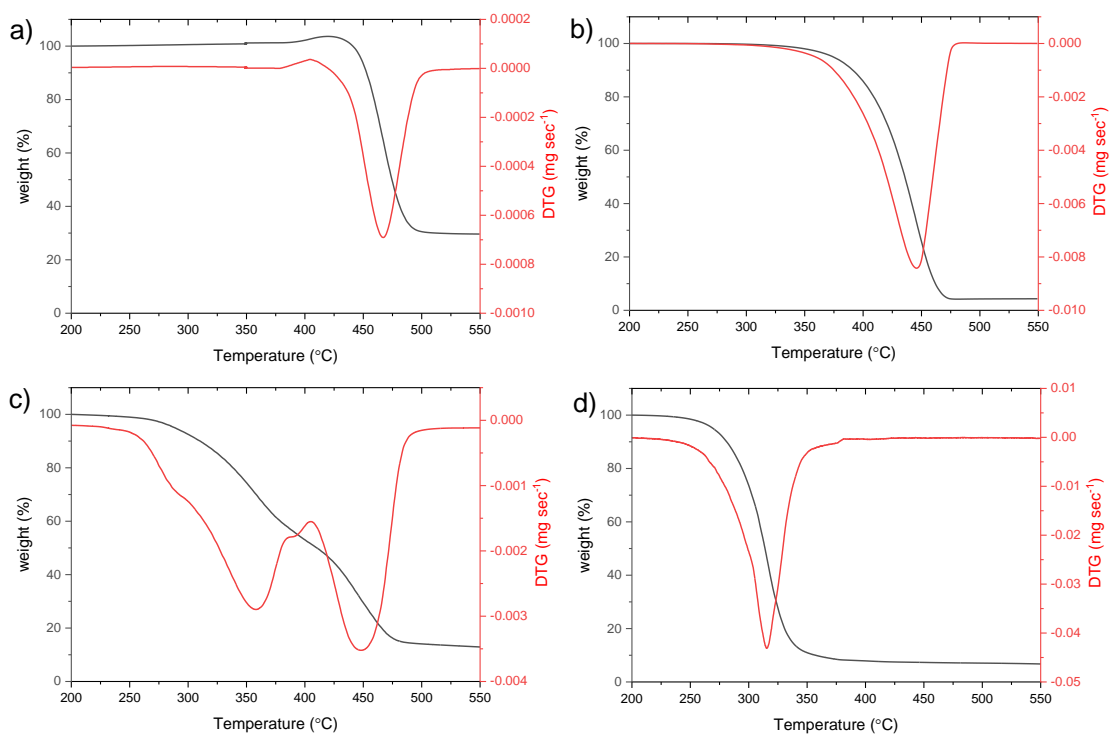
Figure 4.5 Thermogravimetric and derivative thermogravimetric profiles of a) pure PVDF, b) pure [bmim][Tf$_2$N], c) pure [bmim][PF$_6$] and d) pure [bmim][I].
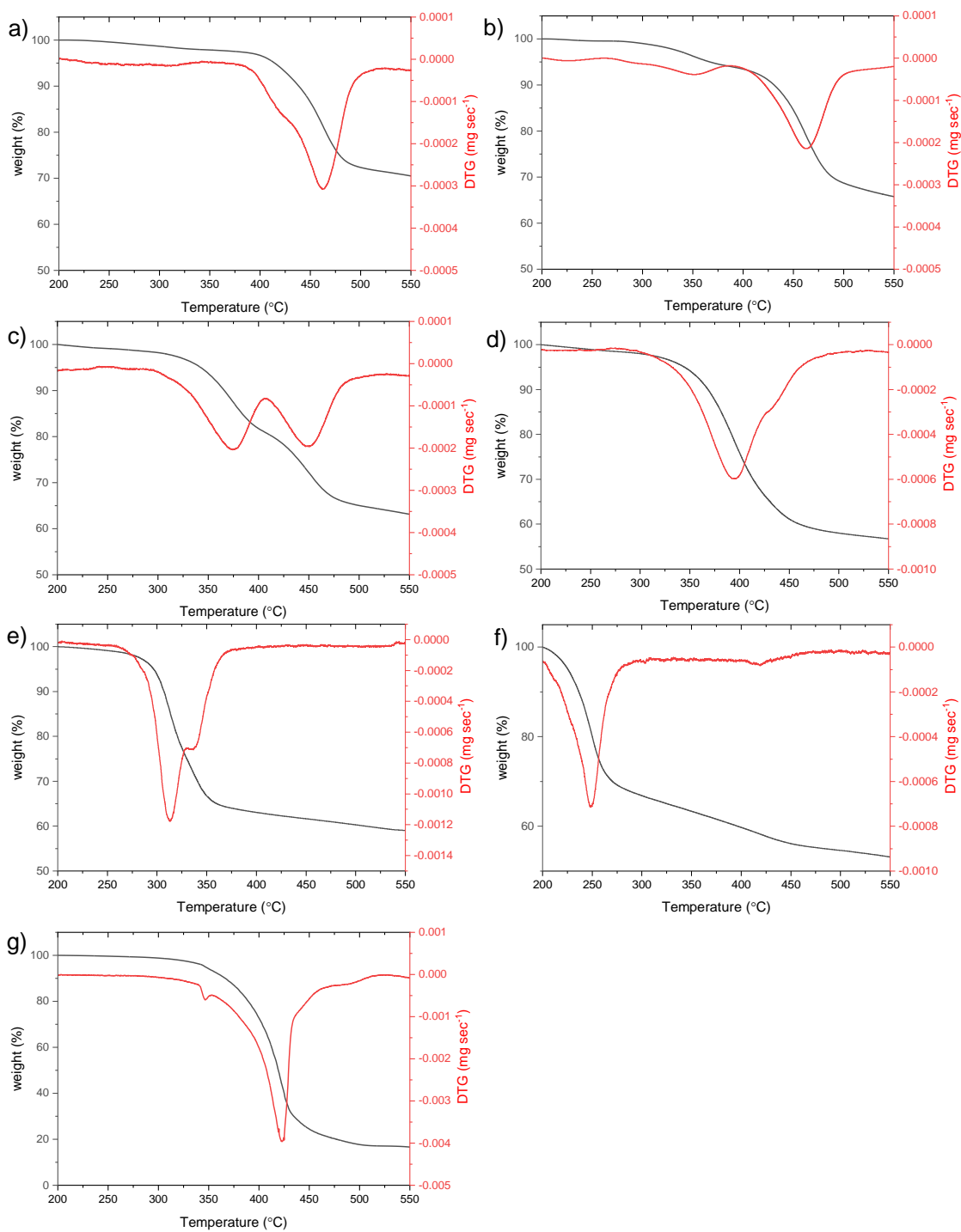
Figure 4.6 Thermogravimetric and derivative thermogravimetric profiles of a) CFMn_SC-1, b) CFMn0.2BT_SC-1, c) CFMn0.5BT_SC-1, d) CFMn1.0BT_SC-1, e) CFMn1.0BP_SC-1, f) CFMn1.0BI_SC-1 and g) CFMn6.0BT_SC-2 electrode.

The compatibility of PVDF and IL were interpreted from DTG peak. electrode composed of only PVDF binder shows DTG peak at 463 ℃, which is near to DTG peak of pure PVDF at 467 ℃. As content of [bmim][Tf$_2$N] increased, DTG peak was splitted into two peaks at higher and lower temperature. Electrode with weight ratio of [bmim][Tf$_2$N]:PVDF as 1.0 shows DTG peak at 313 ℃. Since DTG peak of pure [bmim][Tf$_2$N] was 445 ℃, the reduction of DTG peak in electrode with PVDF and [bmim][Tf$_2$N] cannot be simply considered from effect of only [bmim][Tf$_2$N] itself. The reduction of DTG peak as the increment of [bmim][Tf$_2$N] is considered from complexing behaviour between polymer and IL [111]. During the fabrication of electrode from slurry containing PVDF and IL by sc-CO$_2$ fluid, viscosity of IL decreases due to the diffusion of CO$_2$ into IL, while PVDF swells from absorption of CO$_2$. The reduction of IL viscosity and swelling of PVDF matrix assists the impregnation of IL into PVDF matrix, resulting in complex of PVDF and IL at the end of fabrication process. This complex is formed by attractive force like hydrogen bond between PVDF and IL. Accordingly, DTG peak in lower and higher temperature area are contributed to the complex and pure component, respectively because attractive force between PVDF and IL has lower strength than covalent bond in pure substance. The results of DTG peak reduction were also obtained from electrode with [bmim][PF$_6$] and [bmim][I] as shown in Figure 4.6e and f, respectively. However, electrode with [bmim][Tf$_2$N]:PVDF raio as 6.0 and fabricated by 2-step method of sc-CO$_2$ fluid revealed the small DTG peak at 327 ℃ and larger DTG peak at 422 ℃ as shown in Figure 4.6g. It can be considered that PVDF and [bmim][Tf$_2$N] formed comparatively small amount of complex comparing to total amount of PVDF and [bmim][Tf$_2$N] in this case. The reasons behind this result are contributed to excess amount of IL and defect of 2-step method. Here, the complex cannot be completely formed if amount of IL is comparatively larger than amount of PVDF. The evidence of excess IL can also be observed in electrode morphology shown in Figure 4.4c. Moreover, IL is considered to be hardly impregnated into PVDF in 2-step process since PVDF matrix is shutted after fabrication in the first step. On the other hand, IL is comparatively easier to be impregnated into PVDF in 1-step proess because PVDF matrix is still open in solution. This leads 1-step proess to be more effective than 2-step process. From this section, the complex of PVDF polymer and IL in electrode is called as ionogel, which is the immobilization of IL and solid matrix [112].

4.4.2 Ionic conductivity

        The result of impedance spectroscopy of symmetric cell and curve fitting with equivalent cell is shown in Figure 4.7. The value of circuit components obtained from curve fitting are summarized in Table 4.2. R_b is contributed to bulk resistance in electrolyte, while interfacial resistance R_{ct} is contributed to charge-transfer resistance on the surface between electrolyte and electrodes [113]. The bulk resistance value was found significantly invariable in range between 6.3 to 23.5 Ω although the component in electrode changed. This conforms with contribution of bulk resistance since the same concentration of electrolyte was employed in all measurement. Interfacial resistance of electrode with only PVDF binder was 446.4 Ω. However, interfacial resistance decreased to 357.1, 291.0 and 132.3 Ω as the weight ratio of [bmim][Tf$_2$N]:PVDF increased to 0.2, 0.5 and 1.0. Electrodes with [bmim][PF$_6$] and [bmim][I] also provided low interfacial resistance as 127.8 and 142.0 Ω, respectively. The reduction of interfacial resistance is considered from enhancement of ionic transportation in PVDF/IL ionogel comparing to matrix of only PVDF This corresponds with the consideration that PVDF matrix is non-conductive solid in which ion is non-transferable. On the other hand, PVDF/IL ionogel has properties between solid and liquid in which ion can transfer through the channel containing IL. This improvement of charge transfer is important for Li-O$_2$/CO$_2$ battery since Li-ion has to transfer to electrochemically react with reaction gases on the surface of carbon particle. The benefit of ionogel on performance of Li-O$_2$/CO$_2$ battery is further revealed and discussed in the next section.
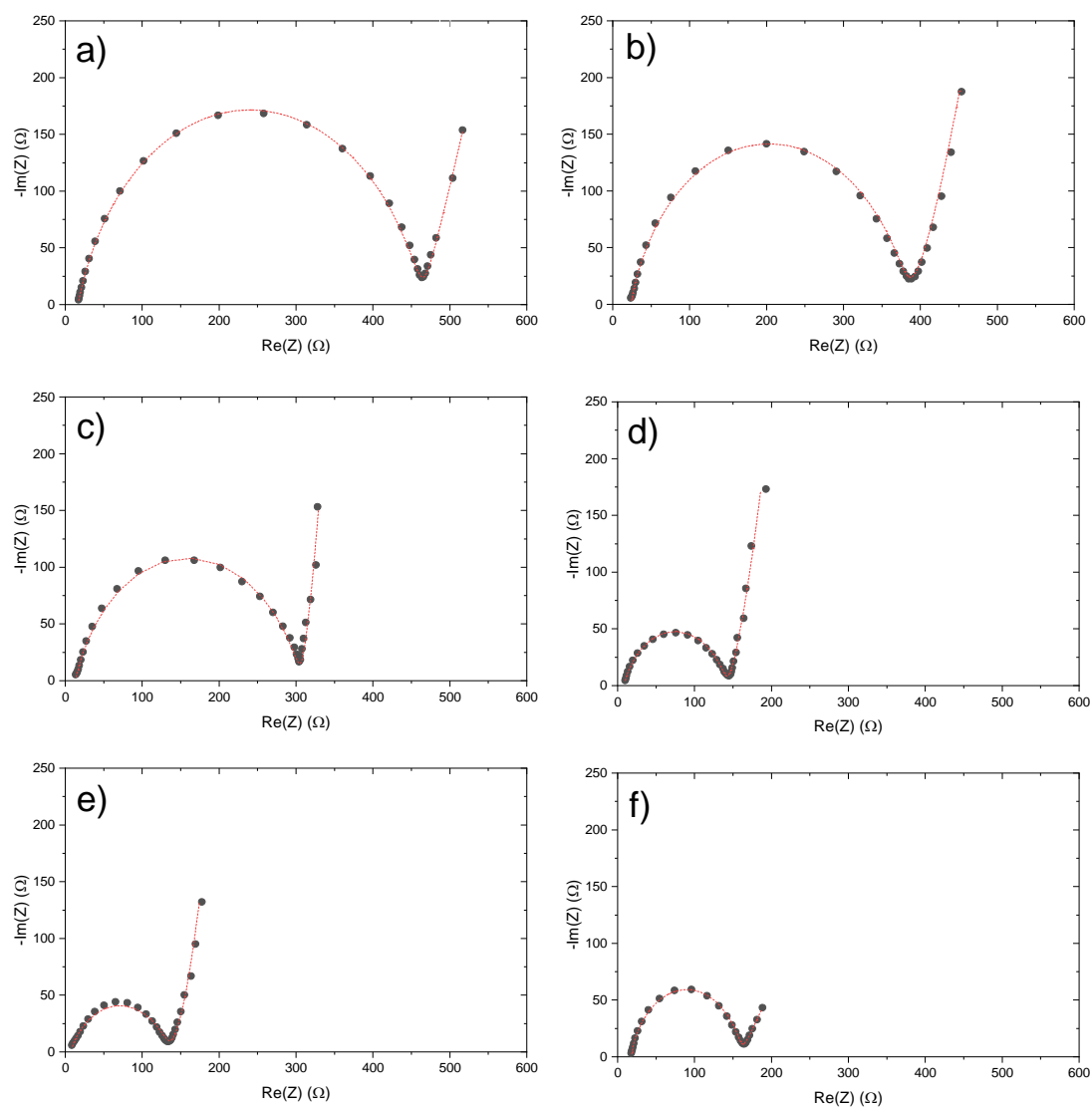
Figure 4.7 Results of impedance spectroscopy (dot) and curve fitting with equivalent circuit (dashed line) of symmetric cell using carbon electrode; a) CFMn_SC-1, b) CFMn0.2BT_SC-1, c) CFMn0.5BT_SC-1, d) CFMn1.0BT_SC-1, e) CFMn1.0BP_SC-1, f) CFMn1.0BI_SC-1. 1.0 M LiTFSI in TEGDME was applied as electrolyte.

Table 4.2 Bulk resistance R_b and interfacial resistance R_{ct} of electrodes in 1.0 M LiTFSI in TEGDME electrolyte.

electrode	Compositions of electrode	Fabrication method	IL:PVDF (weight ratio)	R_b (Ω)	R_{ct} (Ω)
CFMn_SC-1	CB/PVDF/MnO$_2$	scCO$_2$ (1-step)	-	16.4	446.4
CFMn0.2BT_SC-1	CB/PVDF/MnO$_2$/[bmim][Tf$_2$N]	scCO$_2$ (1-step)	0.2	23.5	357.1
CFMn0.5BT_SC-1	CB/PVDF/MnO$_2$/[bmim][Tf$_2$N]	scCO$_2$ (1-step)	0.5	13.0	291.0
CFMn1.0BT_SC-1	CB/PVDF/MnO$_2$/[bmim][Tf$_2$N]	scCO$_2$ (1-step)	1.0	8.0	132.3
CFMn1.0BP_SC-1	CB/PVDF/MnO$_2$/[bmim][PF$_6$]	scCO$_2$ (1-step)	1.0	6.3	127.8
CFMn1.0BI_SC-1	CB/PVDF/MnO$_2$/[bmim][I]	scCO$_2$ (1-step)	1.0	17.5	142.0

4.4.3 Performance of Li-O_2/CO_2 battery

The initial discharge profiles of Li-O_2/CO_2 batteries with 1.0 M LiTFSI in DMSO and TEGDME electrolyte are shown in Figure 4.8, while discharge capacities at the cut-off voltage of Li-O_2/CO_2 batteries with each electrodes are summarized Table 4.3. In DMSO electrolyte, electrode with PVDF binder fabricated from evaporation and sc-CO_2 provided discharge capacity of 0.24 and 2.95 mAh cm^{-2}, respectively. This result conforms with result in Chapter 3 that electrode with higher porosity provides larger discharge capacity due to the enhancement of gas transportation and more accumulation of discharge product. Same result can be obtained in case of TEGDME electrolyte, where electrode with PVDF binder fabricated from evaporation and sc-CO_2 provided discharge capacity of 0.14 and 4.05 mAh cm^{-2}, respectively. As binder was varied from PVDF binder to PVDF/[bmim][Tf$_2$N] ionogel binder, capacity of battery was enhanced to 5.45 mAh cm^{-2} in DMSO electrolyte and 15.07 mAh cm^{-2} in TEGDME electrolyte. This implies that ionogel binder assists the discharge reaction between lithium ion and reaction gases, resulting in the improvement of discharge capacity. However, electrode with weight ratio of [bmim][Tf$_2$N]:PVDF as 6.0 provides discharge capacity of 2.14 mAh cm^{-2} in DMSO electrolyte, which is lower that electrode with PVDF binder. The reduction of capacity lies on the excess amount of IL, which lower porosity and surface area of electrodes. This leads to the failure of reaction gas transfer in the electrodes, resulting in declination of discharge capacity.

Discharge profile of Li-O_2/CO_2 batteries reveals that discharge behavior was affect by type of electrolyte in the batteries. The discharge profile of Li-O_2/CO_2 batteries using DMSO in this work provided discharge plateau at 2.9 V, which is higher than batteries using TEGDME at 2.7 V. This result corresponds with the previous report that DMSO supported the electrochemical pathway of Li$_2$CO$_3$ formation in Li-O_2/CO_2 batteries due to the strong solvation property [43]. However, batteries with TEGDME electrolyte provided larger discharge capacity than batteries using DMSO electrolyte. The suppress of discharge capacity is relied on the instability of DMSO in the presence of oxygen which attacks lithium metal and provides side reaction, leading to dendrite formation in lithium anode [114, 115].
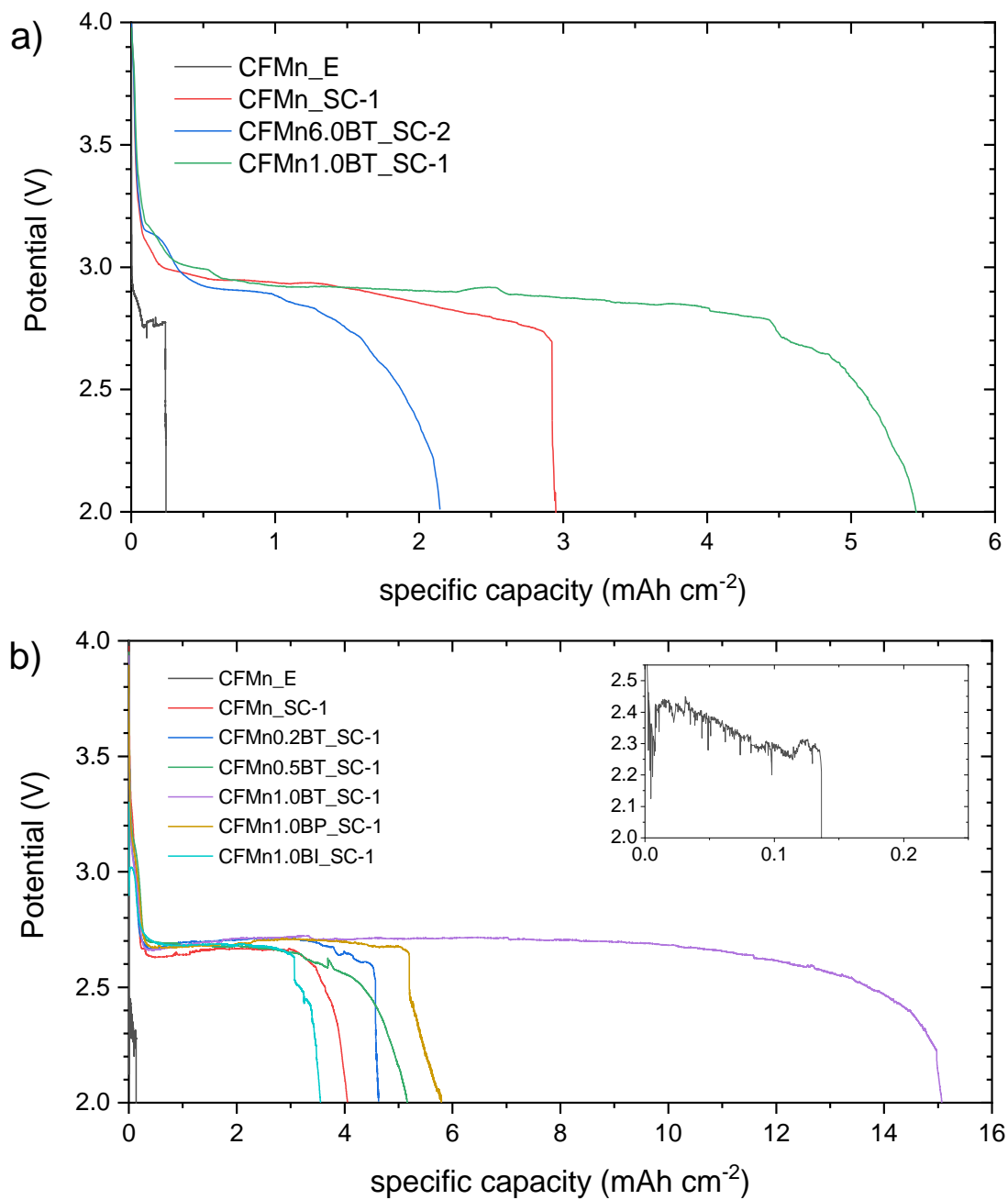
Figure 4.8 Initial discharge profile of Li-O_2/CO_2 battery using a) 1.0 M of LiTFSI in DMSO and b) 1.0 M of LiTFSI in TEGDME.

Table 4.3 Specific capacity and specific energy of Li-O_2/CO_2 batteries.

Cathode	Electrolyte	Specific capacity (mAh cm^{-2})	Specific energy (Wh cm^{-2})
CFMn_E	1.0 M LiTFSI in DMSO	0.24	6.76×10^{-4}
	1.0 M LiTFSI in TEGDME	0.14	3.21×10^{-4}
CFMn_SC-1	1.0 M LiTFSI in DMSO	2.95	8.55×10^{-3}
	1.0 M LiTFSI in TEGDME	4.05	1.09×10^{-2}
CFMn0.2BT_SC-1	1.0 M LiTFSI in TEGDME	4.63	1.25×10^{-2}
CFMn0.5BT_SC-1	1.0 M LiTFSI in TEGDME	5.16	1.35×10^{-2}
CFMn1.0BT_SC-1	1.0 M LiTFSI in DMSO	5.45	1.55×10^{-2}
	1.0 M LiTFSI in TEGDME	15.07	4.00×10^{-2}
CFMn1.0BP_SC-1	1.0 M LiTFSI in TEGDME	5.80	1.54×10^{-2}
CFMn1.0BI_SC-1	1.0 M LiTFSI in TEGDME	3.55	9.44×10^{-3}
CFMn6.0BT_SC-2	1.0 M LiTFSI in DMSO	2.14	6.03×10^{-3}

Type of IL in ionogel binder also influences the discharge capacity of Li-O_2/CO_2 batteries. Discharge capacity reduced to 5.80 and 3.55 mAh cm^{-2}, as the IL was varried from [bmim][Tf$_2$N] to [bmim][PF$_6$] and [bmim][I], respectively. The reason behind this result relies on the solibility of reaction gases in IL. The solubility of O_2 and CO_2 in IL calculated by COSMO-SAC method is shown in Figure 4.9. Calculation result reveals that [bmim][Tf$_2$N] has the highest O_2 and CO_2 solubility among three ILs. [bmim][I] has the lowest CO_2 solubility, while its O_2 solubility is insignificantly different from [bmim][PF$_6$]. It can be seen that electrode using IL with high solubility of O_2 and CO_2 provided larger discharge capacity of Li-O_2/CO_2 battery. It is considered that the reaction gases also transport through the ionogel binder and react with lithium ion to form lithium carbonate over the surface of carbon particle. Accordingly, ionogel containing IL with high reaction gases solubility supports the diffusibility of reaction gases through the ionogel binder, resulting in the reduction of activation energy in electrochemical reaction. Another possible reason is contributed to electrostatic repulsive force between anion of IL and O_2^-, CO_4^-, which are the negative intermediates in discharge reaction of Li-O_2/CO_2 battery [116]. Here, the electrochemical reaction proceeds in IL more effectively if that IL contains anion with low electrostatic repulsive force toward the negative intermediates.

The electrode with PVDF binder and cathode with PVDF/[bmim][Tf$_2$N] ionogel binder after discharging in TEGDME electrolyte were investigated by FE-SEM and XRD to observe the morphology and confirm the discharge product. Morphology and XRD results of electrode after discharge are shown in Figure 4.10 and 4.11, respectively. The block shape of discharge products can be seen in both electrodes after discharge process. XRD result reveals that the discharge product in both electrodes were Li$_2$CO$_3$. However, electrode with PVDF/[bmim][Tf$_2$N] ionogel binder shows higher peak intensity of Li$_2$CO$_3$ than electrode with PVDF binder. This indicates that Li$_2$CO$_3$ is formed in cathode with PVDF-[bmim][Tf$_2$N] gel binder in larger amount than in electrode with PVDF binder, which conforms to the result of the initial discharge capacity.
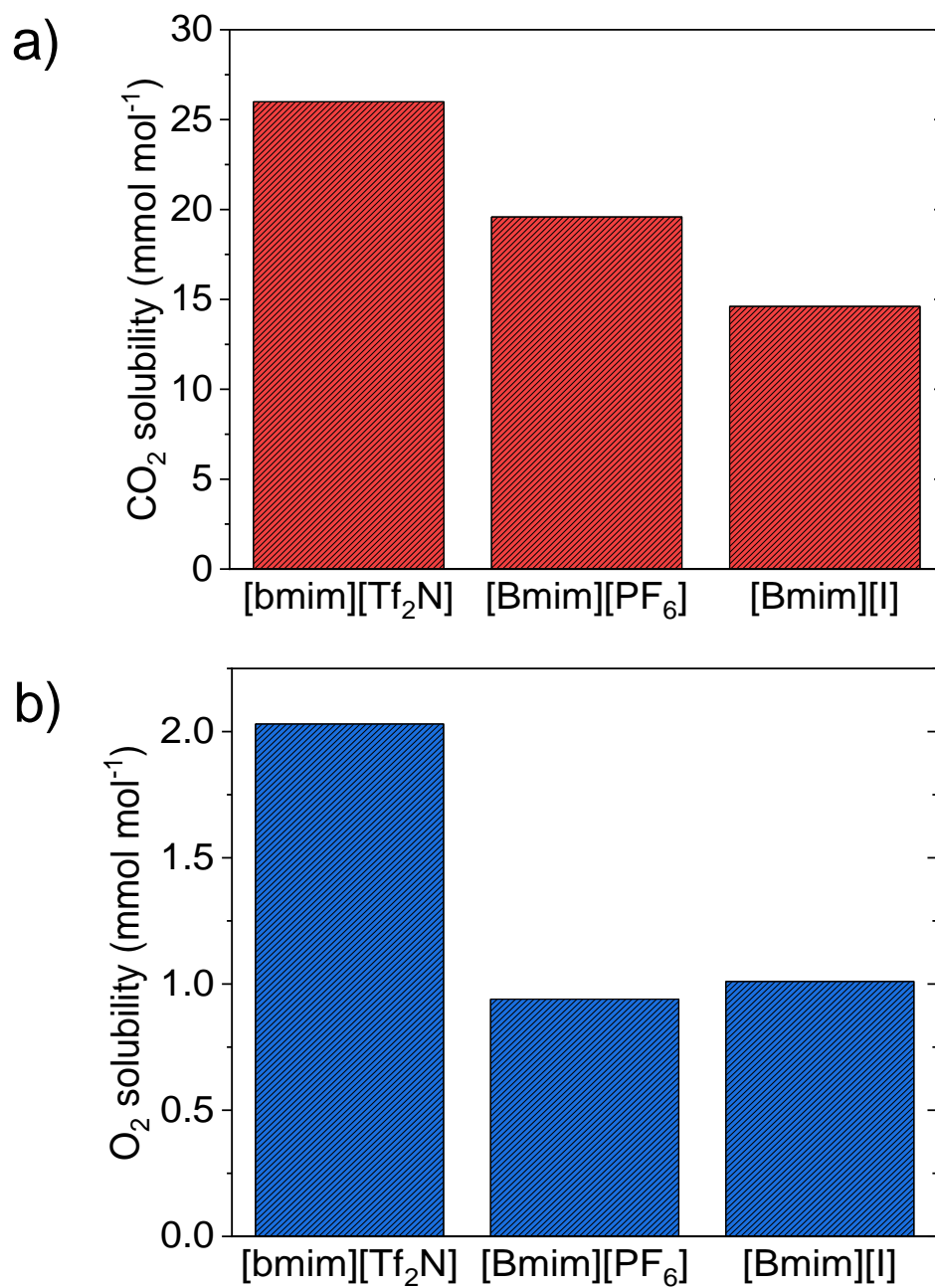
Figure 4.9 Calculated solubility of a) CO_2 and b) O_2 in ionic liquid derived from COSMO-SAC method.
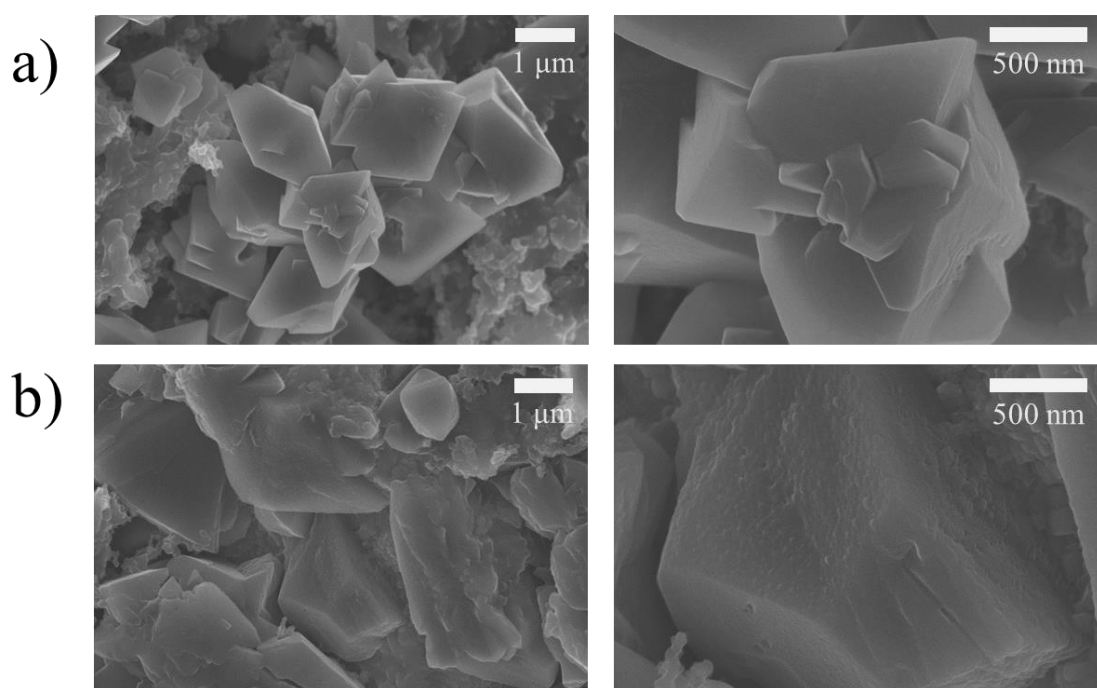
Figure 4.10 Scanning electron microscopy images of electrodes surface of Li-O$_2$/CO$_2$ batteries after initial discharge; a) CFMn_SC-1 electrode and b) CFMn1.0BT_SC-1 electrode.
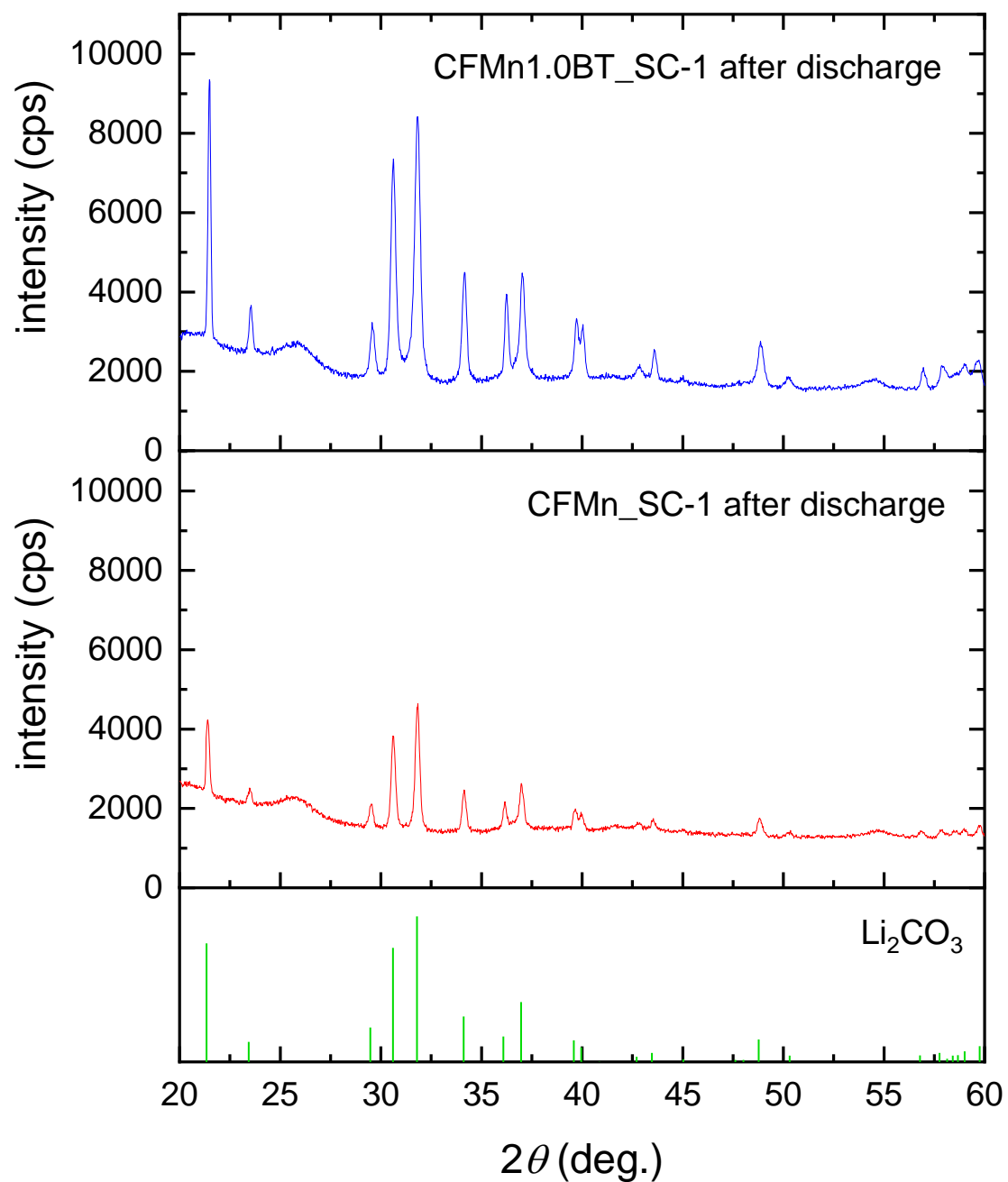
Figure 4.11 X-ray diffraction analysis results of electrodes of Li-O_2/CO_2 batteries after initial discharge.

The difference of discharge mechanism between electrode with PVDF binder and electrode with PVDF/IL ionogel binder is described in Figure 4.12. In term of electrode with PVDF binder, lithium ion and reaction gases are diffused into electrolyte directly reacted over the surface of carbon black. However, lithium ion and reaction gases cannot transfer through the PVDF matrix because of its solidity which limits ionic conductivity and gas permeability. The surface of carbon particle covered by the polymer is inaccessible and considered as void area for discharge reaction. As a result, the discharge product can be formed only over the reaction area. In term of electrode with ionogel binder, part of lithium ion and reaction gases dissolved in electrolyte are directly reacted over the surface of carbon black as same as in PVDF binder. The reaction area in this case is considerably smaller due to the expanding of PVDF/IL ionogel binder complex. Nevertheless, lithium ion and reaction gases can transfer through the gel binder complex and reacted over the surface of carbon particle. The reaction area in this case is considered as both surface of carbon particle which is covered and not covered by the gel binder complex. Correspondingly, electrode with PVDF/IL ionogel binder provides higher discharge capacity than electrode with PVDF binder due to larger reaction area. The higher XRD peak intensity was the evidence that Li_2CO_3 was formed and accumulated over all surface of carbon particle after discharge process.

The cyclabilities of Li-O_2/CO_2 batteries composed of the electrode with PVDF binder and PVDF/[bmim][Tf$_2$N] ionogel binder were investigated. The discharge-charge profile and cyclic performance in DMSO and TEGDME are shown in Figure 4.13. Both electrodes with PVDF binder and PVDF/[bmim][Tf$_2$N] ionogel binder provided 9 maximum cycles. Despite the improvement of the initial discharge capacity, ionogel binder has no catalytic activity on the recharging of Li_2CO_3. DMSO electrolyte system demonstrated unstable discharge-charge profile and provides 4 maximum cycles which is lower than half of the maximum cycles obtained in TEGDME electrolyte system. The instability of cyclic performance in DMSO causes from its instability against lithium metal and the anodic oxidation of DMSO during charging process, forming $DMSO_2$ as the product [117]. This implies that the selectivity of electrolyte is the key to develop the long-life Li-O_2/CO_2 battery.
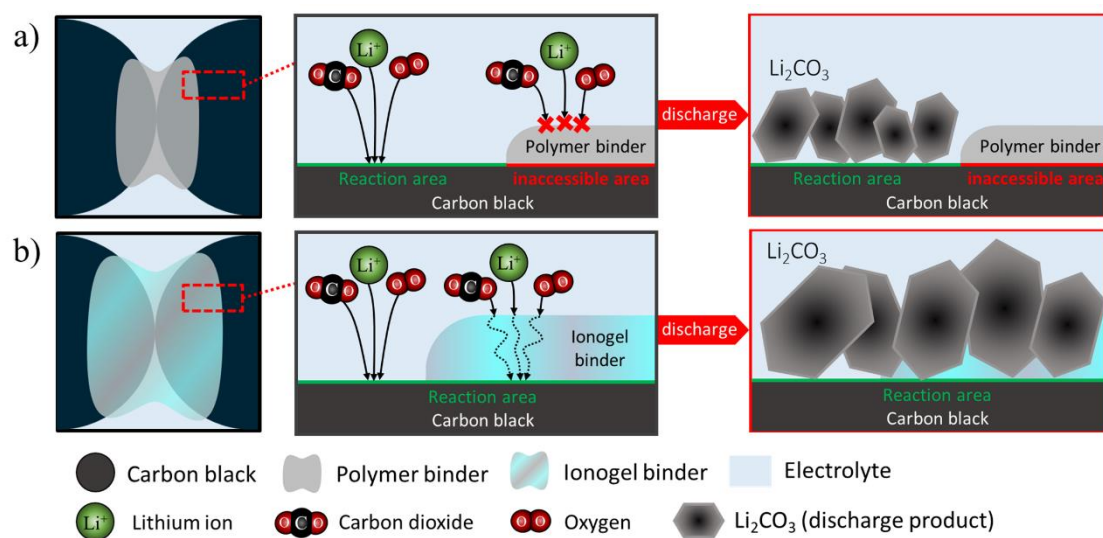
Figure 4.12 Schematic diagram explaining the discharging mechanism of a) electrode with polymer binder and b) electrode with ionogel binder in Li-O$_2$/CO$_2$ battery.
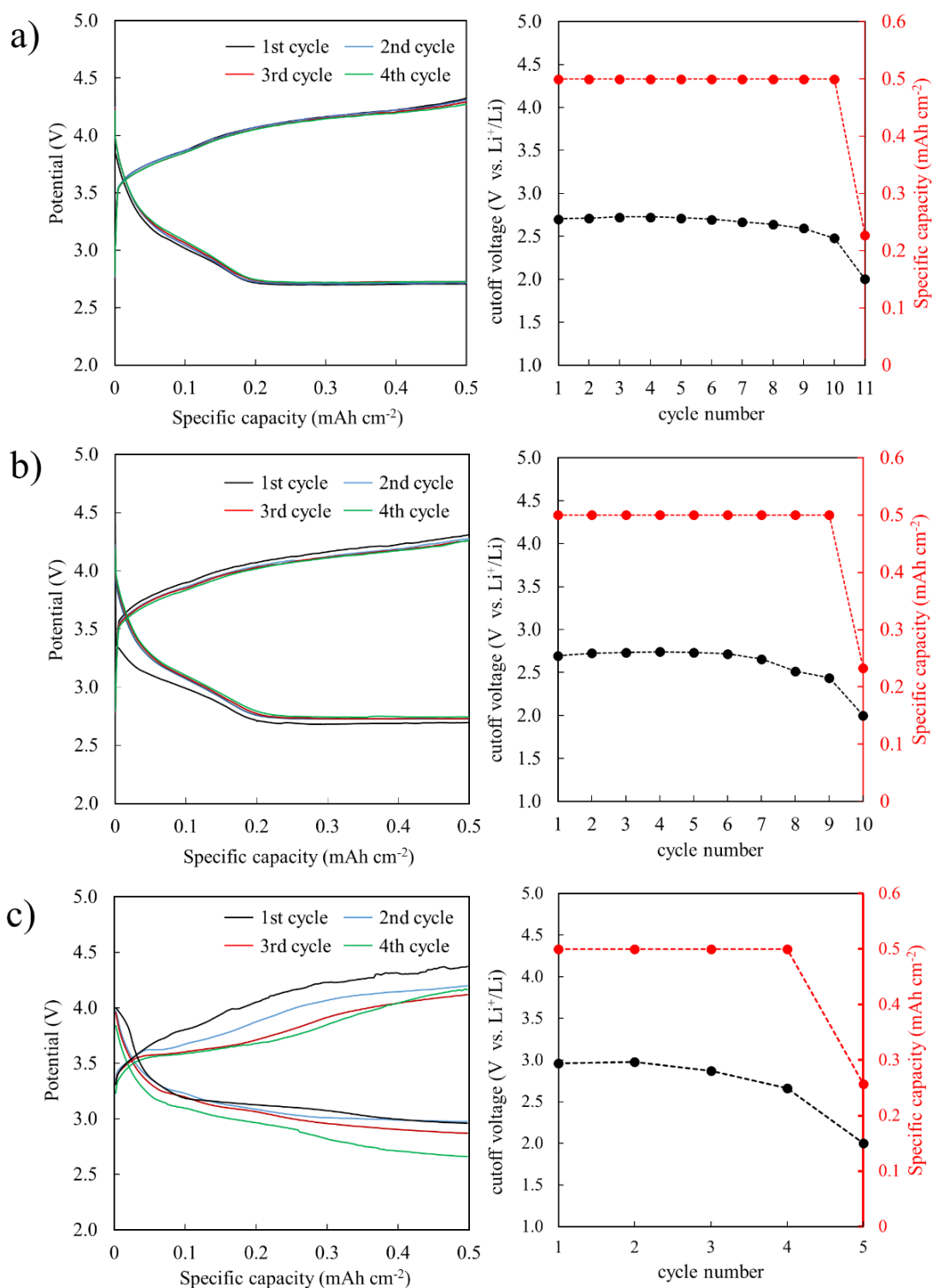
Figure 4.13 Discharge-charge profile of first four cycles and cyclability of Li-O_2/CO_2 batteries using a) CFMn_SC-1 electrode in TEGDME electrolyte, b) CFMn1.0BT_SC-1 electrode in TEGDME electrolyte and c) CFMn1.0BT_SC-1 electrode in DMSO electrolyte.

Chapter 5

Porous carbon electrode with redox mediator-functionalized ionogel binder fabricated in supercritical carbon dioxide

5.1 Statement of problem and objectives

The exhaust gases from combustion of fossil fuel is the main problem which causes the global climate change. This urge us to find the new source of energy with zero emission of greenhouse gases like clean and alternative energy. The demand of new source of energy requires the large capacity of energy storage. Li-O_2 battery is considered as one of the promising energy storages due to its high theoretical energy density, comparable to fossil energy. However, many problems, including pore clogging of discharge product, decomposition of electrolyte and sluggish kinetic on reversibility of discharge product, limit capacity and cyclability of Li-O_2 battery from its theoretical value. Consequently, many researches on development of Li-O_2 battery must be conducted to make Li-O_2 battery more practical.

The highly porous carbon electrode with ionogel binder fabricated by sc-CO_2 fluid are proposed and applied as for cathode of Li-O_2/CO_2 battery in Chapter 4. The porous structure of cathode supports the reaction gases transportation, while ionogel binder improves the ionic conductivity and reaction gases diffusion in binder area, resulting in enhancement of discharge capacity of battery. Although initial discharge capacity was improved by ionogel binder, cyclcability of battery was still limited. In this chapter, IL with redox mediator function was impregnated in ionogel binder of electrode to enhance cyclability of Li-O_2 battery. The cyclability test of electrode with normal binder, ionogel binder and functionalized ionogel binder as cathode of Li-O_2 battery was compared. Moreover, the product after discharging and charging process were investigated to consider the side reaction.

5.2 Experimental

5.2.1 Materials

Carbon dioxide (99.5 %), oxygen (99.7 %) and air were obtained from Fujii-bussan. Acetylene carbon black or CB (99.99 %) with 40 nm diameter was bought from Strem chemicals. Poly(vinylidene fluoride) or PVDF was bought from Fluorochem. 1-methyl-2-pyrrolidone or NMP (99.0 %) and lithium Bis(trifluoromethanesulfonyl)imide or LiTFSI (90.0 %) were purchased from Wako Chemicals. 1-Butyl-3-methylimidazolium bis(trifluoromethylsulfonyl)imide or [bmim][Tf$_2$N] (98.0 %) was bought from Tokyo Chemical Industry. 1-butyl-3-methylimidazolium iodide or [bmim][I] was purchased from Wako. tetraethylene glycol dimethyl ether or TEGDME (98.0 %) was purchased Alfa Aesar.

5.2.2 Fabrication of electrodes

5.2.2.1 Preparation of black viscous slurry

Black viscous slurry was prepared as follows. Initially, PVDF was dissolved into NMP by ultra-sonication at 60 ℃ until polymer was fully dissolved. [bmim][Tf$_2$N] or [bmim][I] was then added in the polymer solution and stirred for 30 min if needed. Then, carbon black was put into the solution and dispersed by ultra-sonication at room temperature for 1 h. The black viscous slurry was finally stirred by magnetic stirrer at room temperature for 12 h. Weight ratio of PVDF to CB, PVDF to NMP were fixed at 1.0 and 13.5, respectively. Weight ratio of IL to PVDf was controlled at 1.0 if black viscous slurry contains IL.

5.2.2.2 Drying of black viscous slurry

1.00 g of black viscous slurry was weighed and put in clean Petri dish (34 mm inner diameter). The Petri dish was tapped to spread out slurry uniformly. NMP in slurry was soon after eliminated by evaporation or sc-CO$_2$ fluid. In term of evaporation, the slurry was brought into thermostat which has temperature controlled at 80 ℃ for 12 h. On the other hands, sc-CO$_2$ fluid was used for solvent elimination and impregnation of

IL. The apparatus used for cathode fabrication by sc-CO_2 fluid is previously shown in Figure 3.1. sc-CO_2 fluid was conducted as the same procedure stated in section 3.2.2.2. Briefly, sc-CO_2 was flowed for 6 h while pressure and temperature of the cell during the process were controlled at 20.0 MPa and 40 °C, respectively. Flowrate of sc-CO_2 was controlled at 6.0 mmol min^{-1}. Finally, Sc-CO_2 was then depressurized for 4 h until pressure reached atmospheric pressure and electrode was brought out of the cell.

5.2.3 Characterization

5.2.3.1 Morphology investigation

Surface morphology of electrodes was investigated by field emission scanning electron microscope (FE-SEM) series JSM-7500F from JEOL located in Technical Department, Ookayama Materials Analysis Division, Tokyo Institute of Technology. Accelerating voltage and beam current were set to 8.0 kV and 10.0 μA, respectively.

5.2.3.2 Porosity measurement

Porosity of electrodes was calculated by equation (3.1). Same method as stated in section 3.2.3.2 was conducted to measure porosity of electrodes.

5.2.3.3 BET surface area

Specific surface area of carbon electrodes was measured from N_2 adsorption isotherms applying Brunauer-Emmett-Teller (BET) method using surface area analyser Gemini VII 2390 series (Micrometric). All electrodes were pre-heated at 200 °C for 1 h prior to the BET analysis to degas and eliminate impurities in the electrode.

5.2.4 Performance of Li-air battery

5.2.4.1 Battery assembly

The same compositions of CR2032 meshed coin cell and coin cell crimping machine as stated in section 3.2.4.1 were employed. The glovebox from Glovebox Japan model GBJV065 was used in this chapter. The difference of this glovebox from the glovebox used in Chapter 3 and 4 was the vacuum function. Initially, the composition for battery assembling was put in the passing cell attached to the glovebox. The main chamber and passing chamber of glovebox were vacuumized until nearly zero pascal. Argon gas then flowed in both chambers after vacuum until pressure reached 1.0 bar. The same procedure for battery assembling as stated in section 3.2.4.1 was conducted. After coin cell assembling, the coin cell battery was passed through passing chamber and brought out from glovebox.

5.2.4.2 Battery performance test

Assembled meshed coin cell battery was locked into coin cell holder which is located inside glass bottle and connected with the the battery cycler. Temperature of this bottle was controlled at 25 ºC by thermostat. Reaction gas was flowed into the box where the outlet flowrate of gas was controlled at 10 ml min^{-1}, 1.0 bar. In case of O_2/CO_2 mixing gases volumetric ratio of O_2 and CO_2 was set to 1.0. Capacity of electrode was then measured by Modulo Bat, battery testing function in the the battery cycler. The current was set as 0.1 mA (0.075 mA cm$^{-2}_{cathode}$) in all measurement. Initial discharge capacity was measured by pre-charging the battery until 4.0 V and then discharge the battery until 2.0 V. The initial discharge capacity was determined by the capacity of battery at the cut-off voltage. Efficiency of discharge capacity was calculated from maximum capacity of Li-air battery employing lithium foil with 1.5 cm diameter and 0.02 cm thickness without consideration of weight of reaction gases. Density of lithium was 0.534 g cm^{-3} and Faraday's constant was 9.6473×10^4 in calculation. As a result, maximum capacity was derived as 72.87 mAh. Full discharge-charge profile of battery was measured by pre-charging the battery until 4.0 V and then discharged of battery until 2.0 V, followed by charging of battery until 4.3 V. the Cyclability of battery was tested by discharging and

charging battery until 1.0 mAh cm^{-2} for many cycles. Range of the cut-off voltage for was set at 2.0 to 5.0 V in all cyclability test. specific capacity was calculated from cathode surface area, which was 1.327 cm^2. Impedance spectroscopy after discharging and charging was measured in frequency range from 10000 Hz to 0.1 Hz at a controlled voltage of 0.01 V by potentio electrochemical impedance spectroscopy function in battery cycler. The schematic diagram for battery test is illustrated in Figure 5.1. The apparatus used for battery test are listed as follows,

- Regulator: Pressure regulator series YR-90 from Yamato Sangyo Co., Ltd.
- Flowmeter: Flowmeter with precision needle valve model RK1200 series from Kojima Instruments Inc. made from SUS316 was used.
- Glass bottle: 100 ml Borosilicate glass bottle from As-one was used as gas chamber.
- Bottle cap: polyprolylene/glass fiber bottle cap (GL45) from As-one was used. The bottle cap has 4 gas channels with valves at the top.
- Battery cycler: Battery cycler series BCS-805 from Biologic was applied. 8 channels of batteries can be tested simultaneously.
- Coin cell holder: CR2032 coin cell holder series BH-2032-25 from Battery Space was employed.
- Thermostat: Automatic oven series EO-300B from AS ONE Corporation was used to controlled temperature of gas chamber.

5.2.4.3 Investigation of electrode after battery test

The same procedure and apparatus as stated in section 4.2.4.3 were used to disassemble the meshed coin cell. Morphology of discharged electrode was investigated by field emission scanning electron microscope (FE-SEM) series JSM-7500F from JEOL located in Technical Department, Ookayama Materials Analysis Division, Tokyo Institute of Technology. Discharged product in electrode was confirmed by benchtop powder X-ray diffraction (XRD) instrument series Mini Flex 600 from Rigaku. XRD was scanned from 20.0 to 60.0 degree at scanning rate of 1 degree min^{-1}.
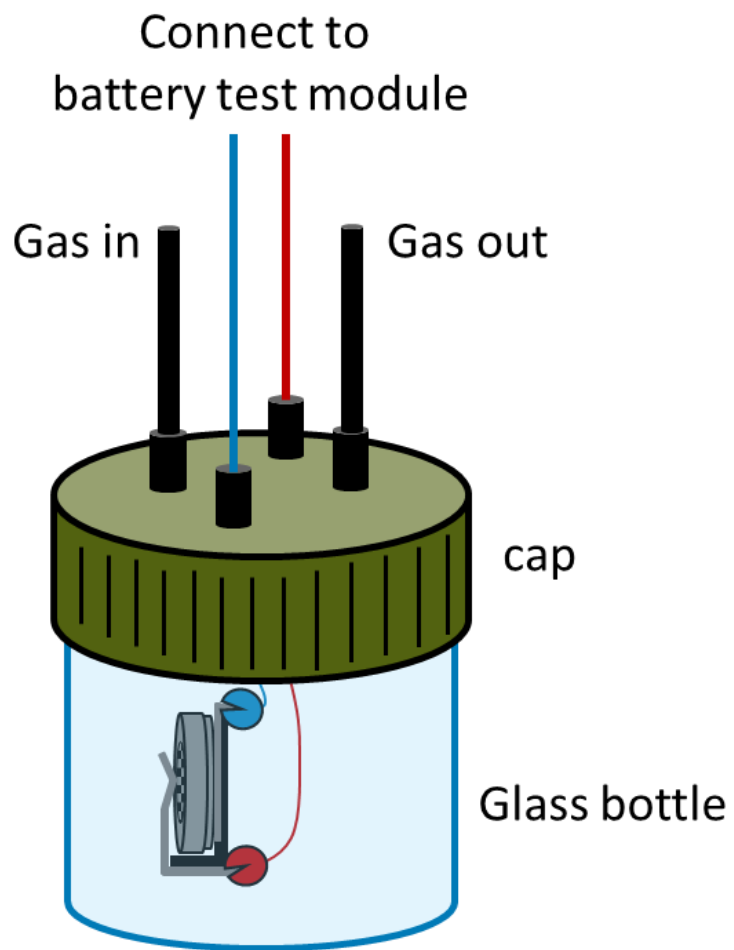
Figure 5.1 Schematic diagram of battery test apparatus.

5.3 Results and discussion

5.3.1 Effect of electrode properties

The composition and properties of electrodes used in this chapter are summarized in Table 5.1. CB/PVDF electrode fabricated from evaporation had porosity of 0.220, while CB/PVDF electrode fabricated from sc-CO_2 fluid provided porosity of 0.935. The difference of porosity is contributed to distinction of the stress on capillary surface between carbon particle and organic solvent during solvent elimination, which is previously stated in section 3.3.1. Porosity and BET surfacea area of the electrode composed of PVDF-IL was reduced, comparing to electrode with only PVDF binder. The reduction of porosity and BET surface area is dedicated to the association of IL in pore of electrode and inside the PVDF matrix.

The surface morphology of electrodes fabricated from sc-CO_2 fluid observed by SEM is shown in Figure 5.2. The morphology of electrode with PVDF binder and electrode with PVDF-IL binder could not be distincguished by SEM images. However, IL is considered to be impregnated into PVDF, forming ionogel complex in the binder of electrode as discussed in section 4.4.1. The CB/PVDF electrode and CB/PVDF/[bmim][Tf$_2$N] electrode fabricated from evaporation and sc-CO_2 fluid were applied as cathode of Li-O_2 battery and tested the capacity. The result of initial discharge capacity measurement of Li-O_2 battery along with impedance of the pisrine battery and the battery after discharge is shown in Figure 5.3. Li-O_2 battery composed of CB/PVDF electrode fabricated from sc-CO_2 fluid provided discharge capacity of 18.4 mAh cm^{-2}, while Li-O_2 battery composed of CB/PVDF/[bmim][Tf$_2$N] electrode fabricated from sc-CO_2 fluid provided discharge capacity of 22.7 mAh cm^{-2}. The enhancement of discharge capacity is dedicated to the improvement of ionic conductivity and oxygen solubility in ionogel binder, enlarging reaction surface area over carbon particle as stated in section 4.4.3. This consideration was further confirmed by impedance after discharge.

Table 5.1 Composition, fabrication method and properties of electrodes.

electrode	Compositions of electrode	Fabrication method	CB:PVDF (weight ratio)	IL:PVDF (weight ratio)	Porosity	BET ($m^2 g^{-1}$)
CF_E	CB/PVDF	evaporation	1.0	-	0.220	21.34
CFBT_E	CB/PVDF/[bmim][Tf$_2$N]	evaporation	1.0	1.0	0.169	5.64
CF_SC	CB/PVDF	sc-CO$_2$	1.0	-	0.935	13.84
CFBT_SC	CB/PVDF/[bmim][Tf$_2$N]	sc-CO$_2$	1.0	1.0	0.841	8.78
CFBI_SC	CB/PVDF/[bmim][I]	sc-CO$_2$	1.0	1.0	0.864	5.87

*porosity was calculated from density of CB = 2.023 g cm^{-3}, PVDF = 1.648 g cm^{-3}, [bmim][Tf$_2$N] = 1.44 g cm^{-3}, [bmim][I] = 1.46 g cm^{-3}
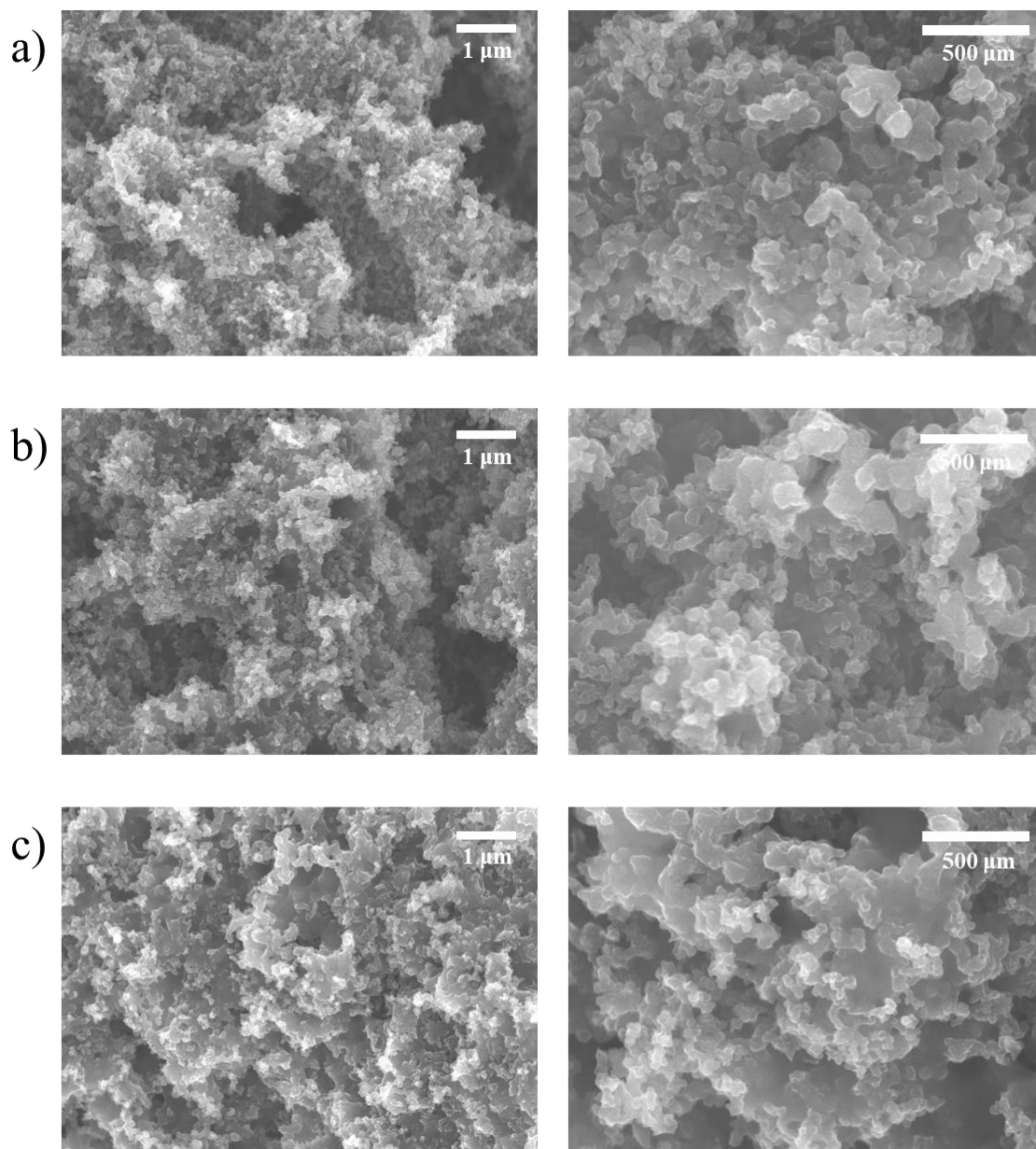
Figure 5.2 Surface morphology of electrode fabricated from sc-CO_2 fluid composed of a) CB/PVDF, b) CB/PVDF/[bmim][Tf_2N] and c) CB/PVDF/[bmim][I].
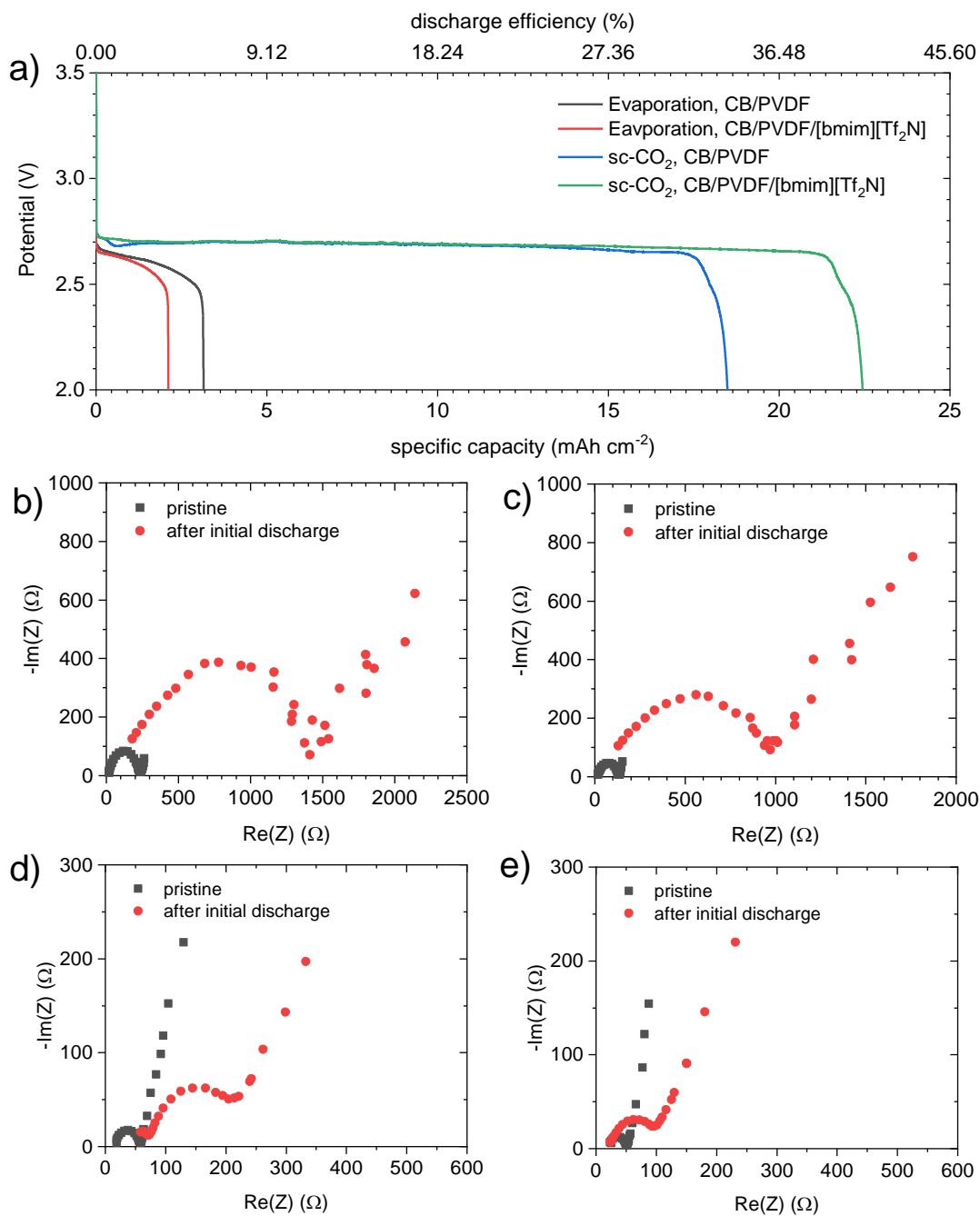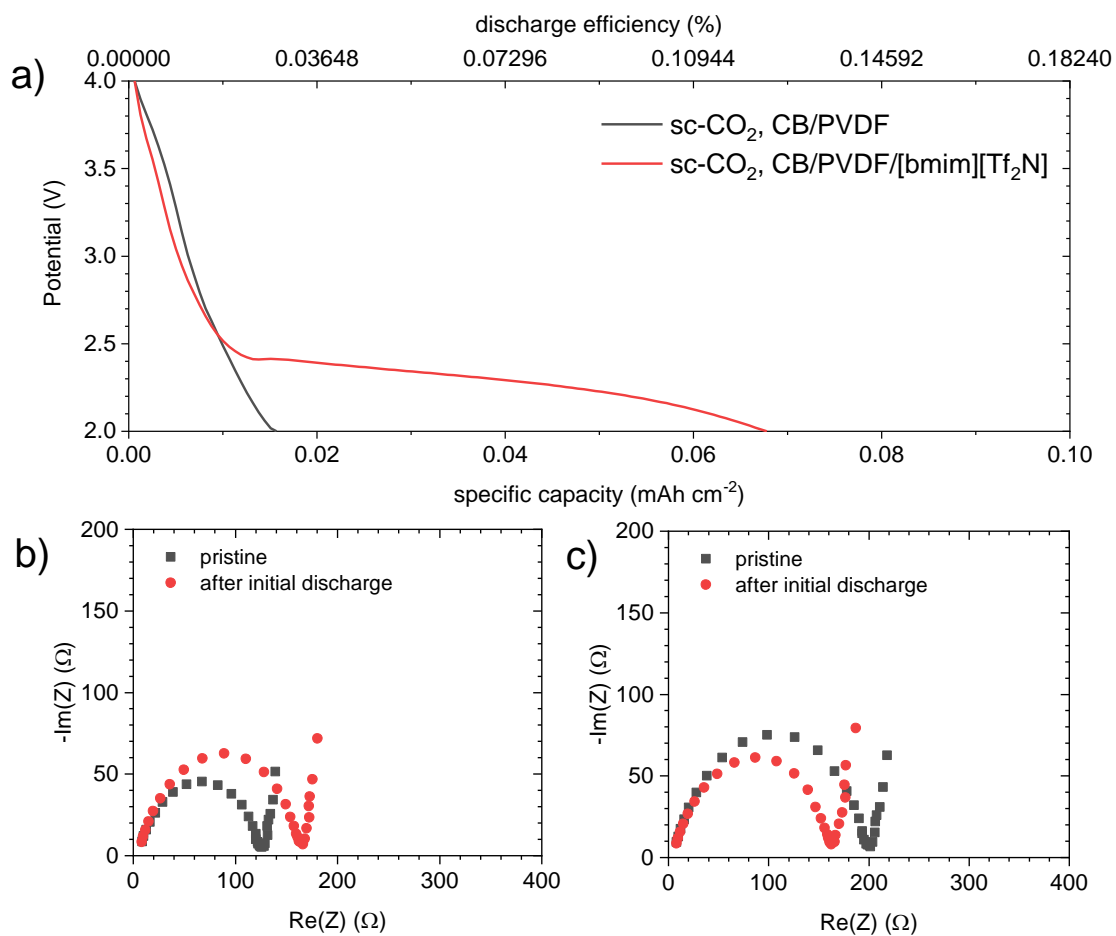
Figure 5.3 Initial discharge capacity (a), impedance spectroscopy of pristine battery and battery after initial discharge in presence of pure O_2; b) CB/PVDF electrode fabricated from sc-CO_2 fluid, c) CB/PVDF/[bmim][Tf$_2$N] electrode fabricated from sc-CO_2 fluid, d) CB/PVDF electrode fabricated from evaporation and e) CB/PVDF/[bmim][Tf$_2$N] electrode fabricated from evaporation.

It can be seen from Figure 5.3b-e that Li-O$_2$ battery with CB/PVDF/[bmim][Tf$_2$N] electrode provided lower charge-transfer resistance after discharge than Li-O$_2$ battery with CB/PVDF electrode. The reduction of charge-transfer resistance implies that larger amount of lithium ion can transfer from electrolyte to react with reaction gases over surface of carbon particle when cathode with ionogel binder was employed. Although IL assisted discharge capacity of electrode fabricated from sc-CO$_2$, electrode fabricated from evaporation showed the contrast result. Li-O$_2$ battery with CB/PVDF/[bmim][Tf$_2$N] electrode fabricated from evaporation provided 2.3 mAh cm^{-2} discharge capacity, which was smaller than Li-O$_2$ battery with CB/PVDF electrode fabricated from evaporation providing 3.4 mAh cm^{-2}. The opposite result is considered from the large difference in BET surface area as seen in Table 5.1. In term of evaporation, CB/PVDF/[bmim][Tf$_2$N] electrode had the lowest porosity at 0.169. Although IL assisted the transportation of lithium ion during discharge process, the drawback from reduction of porosity performs the larger effect due to lacking pore size for gas diffusion and pore volume for discharge product accumulation. Another reason could be considered from difference of evaporation and sc-CO$_2$ fluid on formation of complex of IL and PVDF in ionogel binder. It is considered that sc-CO$_2$ fluid assists the formation of ionogel by the reduction of IL viscosity and PVDF swelling. However, PVDF is crystallized during evaporation of solvent, resulting in the incapability of complex formation between IL and crystalline PVDF. Accordingly, the advantage of IL on enhancement of discharge capacity is limited only to the electrode fabricated from sc-CO$_2$.

5.3.2 Effect of reaction gases

The coin cell batteries composed of CB/PVDF and CB/PVDF/[bmim][Tf$_2$N] were tested with air, oxygen and carbon dioxide mixing gases and pure carbon dioxide to investigate the effect of reaction gases on battery performance. The results of battery and impedance spectroscopy before and after discharge in presence of air, O$_2$/CO$_2$ mixing gases and pure CO$_2$ are shown in Figure 5.4 to 5.6, respectively. It can be seen from the results that CB/PVDF/[bmim][Tf$_2$N] electrode provided larger initial discharge capacity than CB/PVDF electrode in all conditions of reaction gases. This is contributed to the
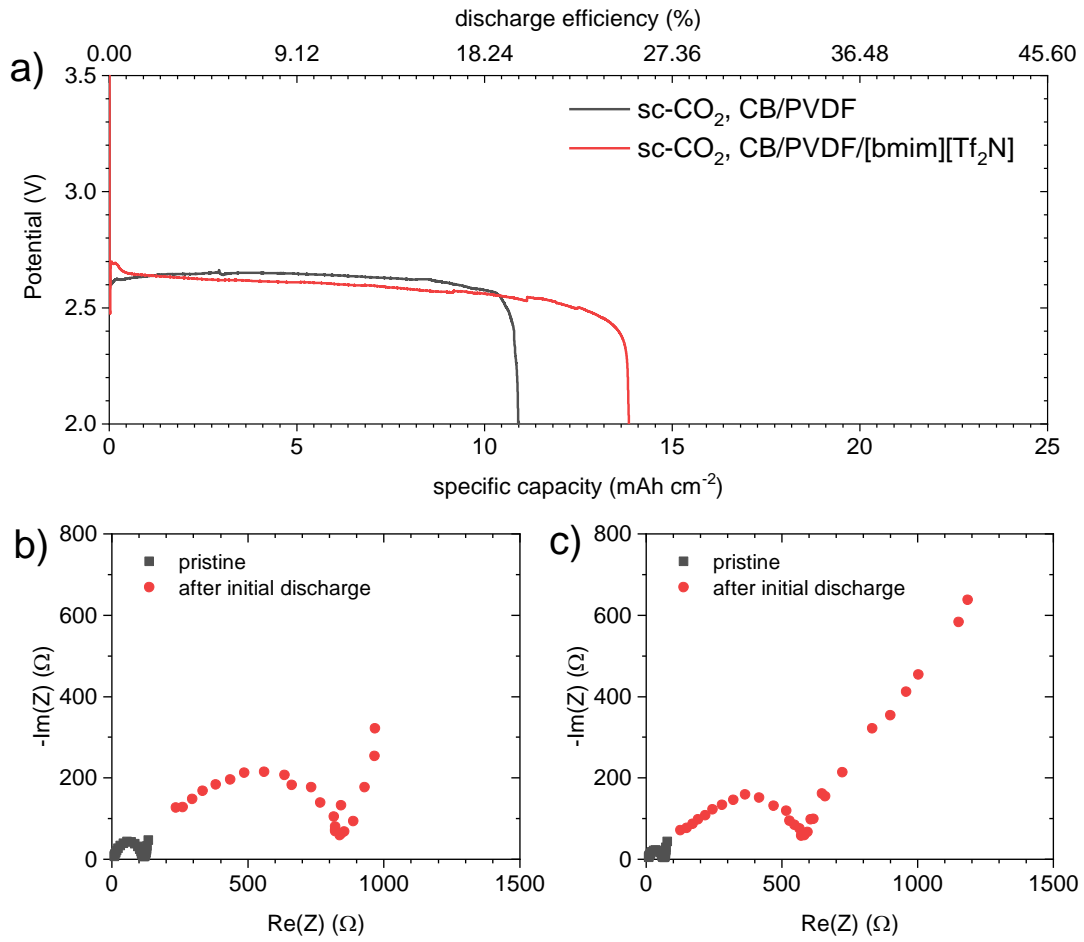
Figure 5.4 Initial discharge capacity (a), impedance spectroscopy of pristine battery and battery after initial discharge in presence of air; b) CB/PVDF electrode fabricated from sc-CO$_2$ fluid and c) CB/PVDF/[bmim][Tf$_2$N] electrode fabricated from sc-CO$_2$ fluid.
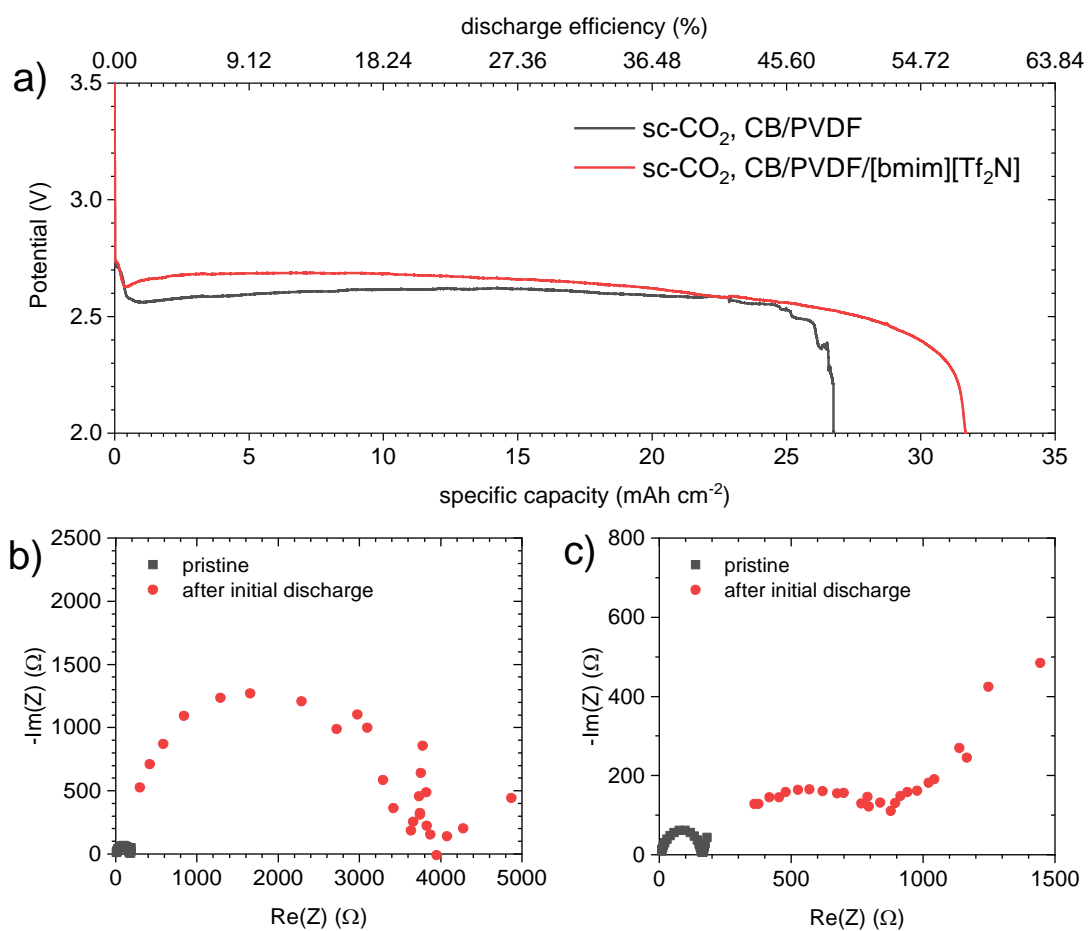
Figure 5.5 Initial discharge capacity (a), impedance spectroscopy of pristine battery and battery after initial discharge in presence of O_2/CO_2 mixing gases (1:1); b) CB/PVDF electrode fabricated from sc-CO_2 fluid and c) CB/PVDF/[bmim][Tf$_2$N] electrode fabricated from sc-CO_2 fluid.

Figure 5.6 Initial discharge capacity (a), impedance spectroscopy of pristine battery and battery after initial discharge in presence of pure CO_2; b) CB/PVDF electrode fabricated from sc-CO_2 fluid and c) CB/PVDF/[bmim][Tf_2N] electrode fabricated from sc-CO_2 fluid.

Reduction of charge-transfer and reaction gases diffusion from ionogel binder. However, the discharge capacity was varied by condition of reaction gases. CB/PVDF electrode and CB/PVDF/[bmim][Tf$_2$N] electrode provided 11.0 and 14.7 mAh cm^{-2} in presence of air, respectively, which was lower than discharge capacity in term of pure oxygen. The reduction of capacity comparing to presence of pure oxygen is considered from the lower oxygen ratio since oxygen occupied only approximately 21 % in air [118]. This limits the discharge reaction due to insufficient of oxygen after large accumulation of discharge product on the surface of carbon particle. The reduction of capacity in air also previously reported in the simulation of discharge capacity comparing Li-O$_2$ battery in presence of air and oxygen [119]. Accordingly, the ratio of reaction gas in feeding gas has large influence on the performance of Li-air battery.

As reaction gas was varied to O$_2$/CO$_2$ mixing gases, CB/PVDF electrode and CB/PVDF/[bmim][Tf$_2$N] electrode provided discharge capacity of 26.9 and 31.8 mAh cm^{-2}, respectively, which were the highest capacity among all conditions of reaction gases. The enhancement of discharge capacity in presence of O$_2$/CO$_2$ mixing gases conforms with previous report [17]. This phenomenon was explained by comparably more stable C$_2$O$_6^{2-}$ intermediate, leading to slower accumulation of discharge product. This allows discharge product to be fully filled in the pore of electrode, resulting in the larger discharge capacity. Although the addition of carbon dioxide in reaction gases prolonged the capacity of battery, electrode provided extremely low discharge capacity nearly zero in presence of pure CO$_2$. This result conforms with previous report that Li-air battery could not be discharged in presence of pure CO$_2$. However, several report contrastly indicated the possibility of Li-air battery in presence of pure CO$_2$ as Li-CO$_2$ battery [18, 19]. The difference of possibility relies on the presence of catalyst and electrode composition, which could enhance the catalytic activity of oxidation reaction with CO$_2$.

The discharge products in electrodes under all conditions of reaction gases were also investigated by XRD analysis and FE-SEM. The results of XRD analysis and FE-SEM images of electrode after discharge are shown in Figure 5.7 and 5.8, respectively. According to the results, Li$_2$O$_2$ and LiOH were accumulated as discharge product when battery was discharged in air and oxygen. It is considered that Li$_2$O$_2$ is generated by the reduction reaction of oxygen, while LiOH is occurred from electrochemical reaction

between H_2O and Li_2O_2 [21]. The presence of water in reaction gas is considered as from the humidity in the gas chamber or from decomposition of TEGDME during discharge process [123]. The peak intensity of LiOH was found to be higher when battery was discharged in air comparing to pure oxygen. Since oxygen is limited in air, humidity in the reaction gas involves in the formation of LiOH greater comparing to case of pure oxygen. This resulted in the larger accumulation of LiOH as the main discharge product. In term of O_2/CO_2 mixing gases, Li_2CO_3 was confirmed as discharge product. Li_2CO_3 is considered to be form through the route of $C_2O_6^{2-}$, which is the intermediate in the discharge reaction of Li-O_2/CO_2 battery. The reaction mechanism of Li-O_2/CO_2 battery is mentioned in section 1.3.1.1 as reactions (1.5) to (1.9).

It can be concluded that Li_2O_2, LiOH and Li_2CO_3 were the main discharge product when battery was discharged in pure oxygen, air and O_2/CO_2 mixing gases, respectively. According to result from XRD analysis, peak intensity of these main discharge product was higher when battery employed CB/PVDF/[bmim][Tf_2N] electrode comparing to CB/PVDF electrode. The enhancement of peak intensity is contributed to the improvement of charge-transfer and reaction gas diffusibility in ionogel binder, providing larger reaction area for discharge reaction. As a result, electrode has capability to accumulate more discharge product, leading to the greater improvement of discharge capacity.

5.3.3 Redox mediator-functionalized ionogel binder for Li-O_2 battery

It is previously stated that ionogel binder assists the discharge capacity of Li-air battery regardless the reaction gases. This supports Li-air battery to be applied more efficiently as the primary battery. However, ionogel binder has defect that it does not assist the cyclic performance of Li-air battery as stated in section 4.4.3. In this section, [bmim][I] was employed as the IL with function of redox mediator. This function is contributed to I^- anion in the IL which was previously reported [45]. The effect of functionalized IL in electrode was investigated and compared with electrode without IL and non-functionalized IL. [bmim][Tf_2N] was used as non-functionalized IL for comparison. The full discharge-charge profile of Li-O_2 battery using CB/PVDF,
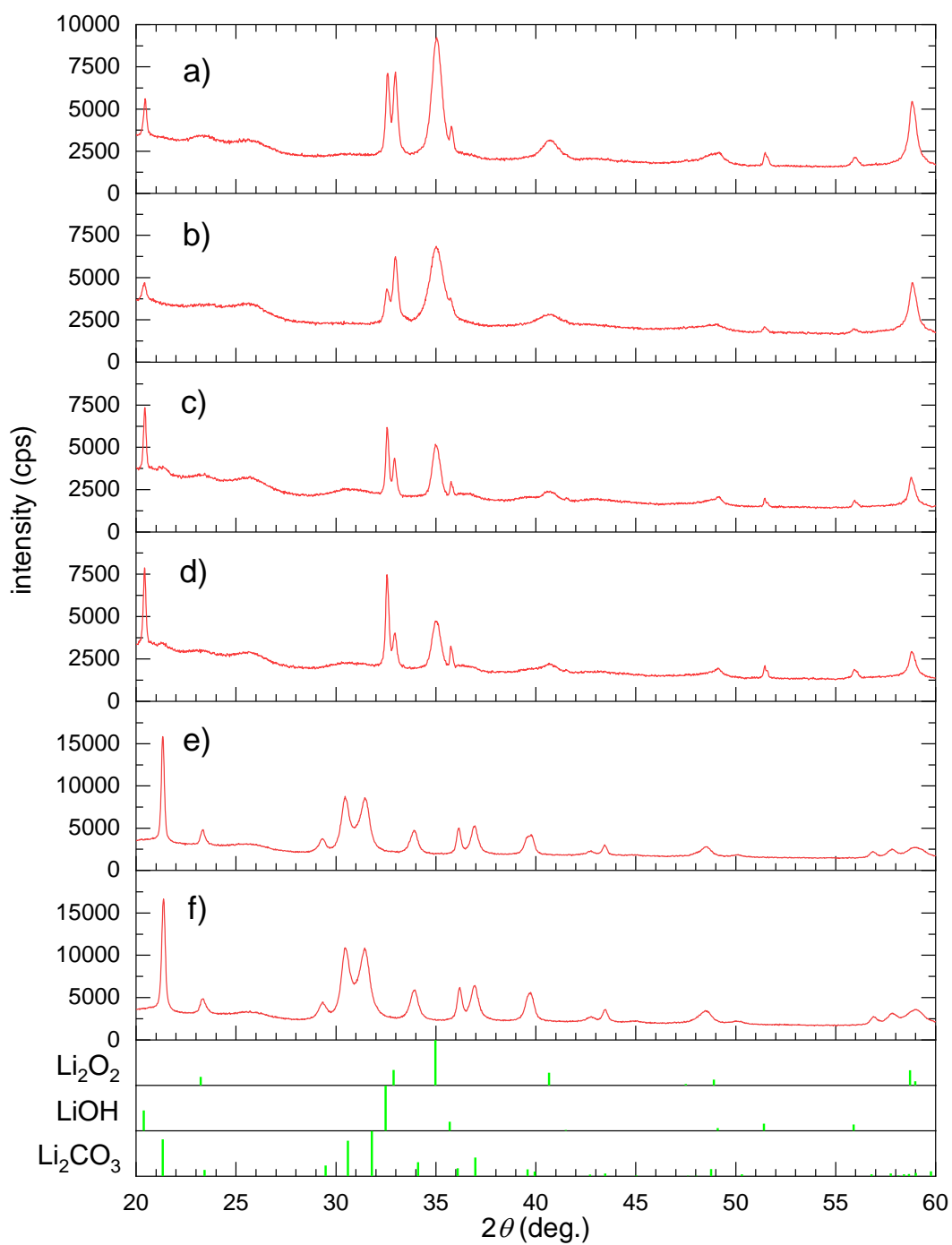
Figure 5.7 X-ray diffraction analysis of electrode after discharge; a) CB/PVDF electrode and b) CB/PVDF/[bmim][Tf$_2$N] electrode in presence of pure oxygen, c) CB/PVDF electrode and d) CB/PVDF/[bmim][Tf$_2$N] electrode in presence of air, e) CB/PVDF electrode and f) CB/PVDF/[bmim][Tf$_2$N] electrode in presence of O$_2$/CO$_2$ mixing gases.
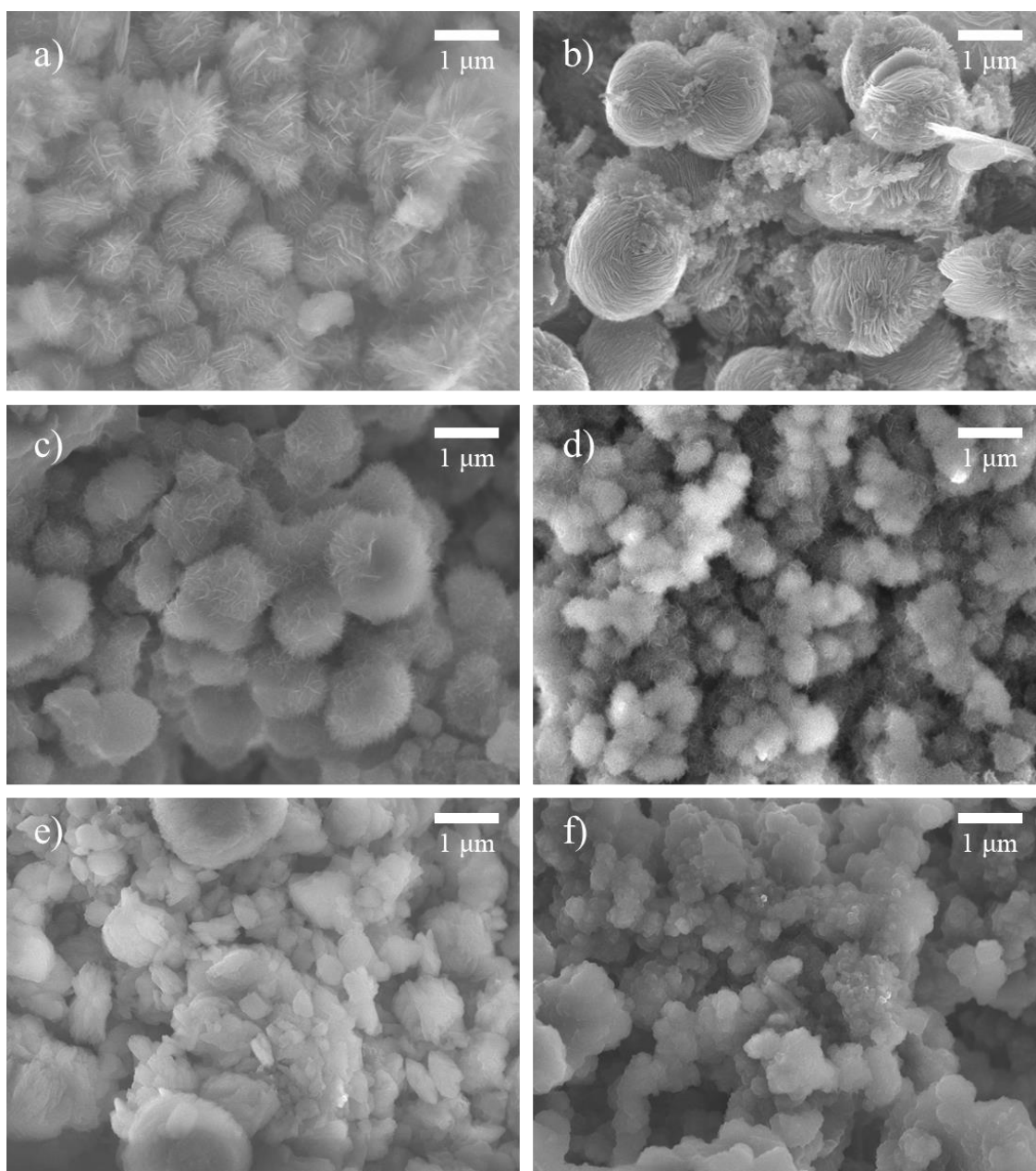
Figure 5.8 Morphology of electrode surface after discharge; a) CB/PVDF electrode and b) CB/PVDF/[bmim][Tf$_2$N] electrode in presence of pure oxygen, c) CB/PVDF electrode and d) CB/PVDF/[bmim][Tf$_2$N] electrode in presence of air, e) CB/PVDF electrode and f) CB/PVDF/[bmim][Tf$_2$N] electrode in presence of O$_2$/CO$_2$ mixing gases.

CB/PVDF/[bmim][Tf_2N] and CB/PVDF/[bmim][I] electrode fabricated from sc-CO_2 fluid are shown in Figure 5.9. 1.0 M of LiTFSI in TEGDME was used as electrolyte. The discharge capacity of battery using CB/PVDF/[bmim][I] electrode provided lowest discharge capacity at 17.7 mAh cm^{-2}. The reduction of discharge capacity is considered from low solubility of oxygen in [bmim][I] comparing to [bmim][Tf_2N] and dropping of porosity as seen in Figure 4.9 and Table 5.1, respectively. All electrodes provided the same discharge plateau around 2.7 V, indicating that [bmim][I] has no catalytic activity on discharge reaction. However, the battery with CB/PVDF/[bmim][I] electrode provided average charging potential at 3.76 V, while battery with CB/PVDF electrode and battery with CB/PVDF/[bmim][Tf_2N] electrode showed average charging potential at 4.15 V and 4.16 V, respectively. The suppression of charging potential conforms with the previous report which employ LiI in the electrolyte as redox mediator [45]. The reduction of overpotential was explained from charging reaction via electrochemical route of I^-.

To further investigate the discharging and charging mechanism of Li-O_2 batteries, XRD analysis and SEM observation of electrodes after discharge and charge were conducted. The results of XRD analysis and morphology from SEM images are shown in Figure 5.10 and 5.11, respectively. XRD results show that Li_2CO_3 was accumulated in the CB/PVDF electrode, while Li_2CO_3 and LiCOOH·H_2O were accumulated in the electrode after full charge of battery. Although many researches reported about high stability of glyme-based electrolyte in Li-O_2 battery, the formation of lithium carbonate and carboxilate are considered from the decomposition of TEGDME electrolyte during charging process [120]. Another reason for the accumulation of carbonate species is contributed to the corrosion of carbon electrode by Li_2O_2 [121, 122]. Moreover, several report indicated that lithium carbonate was possibly formed during discharge process of Li-O_2 battery due to the decomposition of glyme-based electrolyte [123, 124]. Although Li_2O_2 and LiOH were formed after discharge process of Li-O_2 battery using CB/PVDF and CB/PVDF/[bmim][Tf_2N] electrode, Figure 5.10e indicates that LiOH and LiOH·H_2O were the main discharge product in Li-O_2 battery using CB/PVDF/[bmim][I] electrode, while XRD peak of Li_2O_2 could not be detected. This result is contrary to previous report using LiI as redox mediator, that Li_2O_2 was the main product after discharge reaction [45].
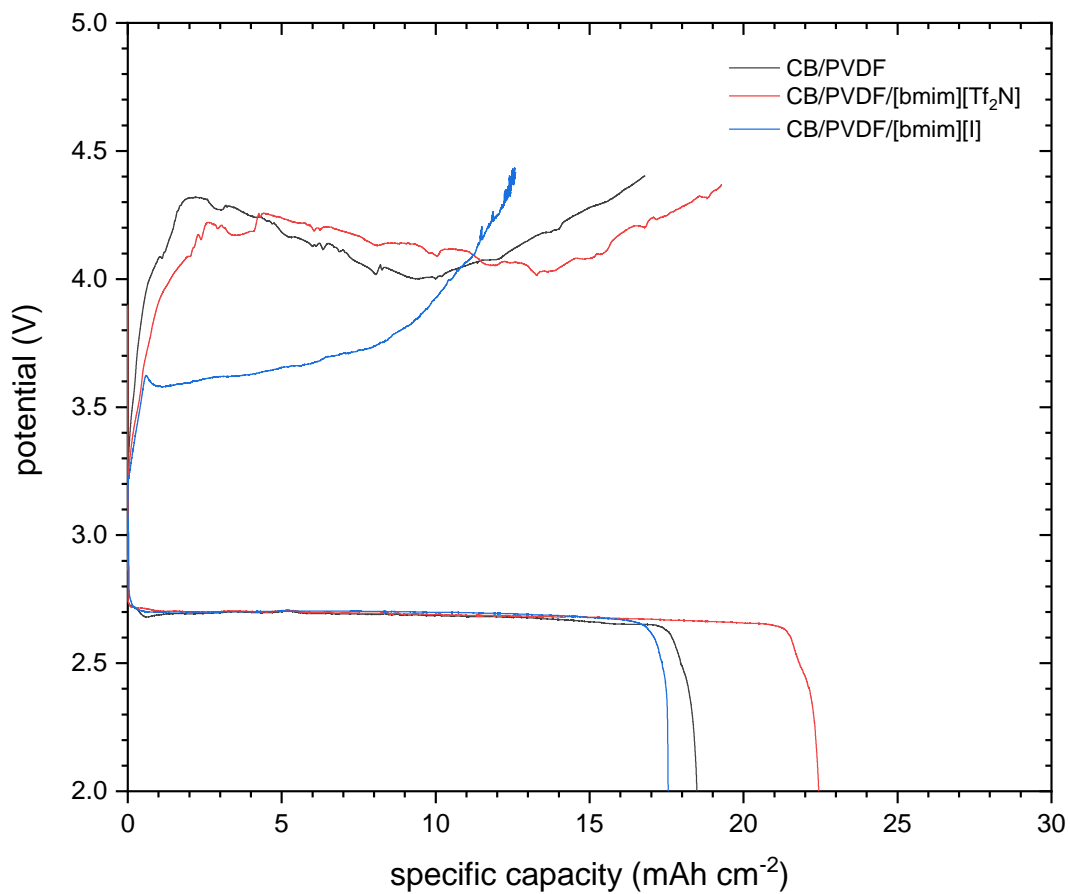
Figure 5.9 Full discharge-charge profile of Li-O$_2$ battery using CB/PVDF electrode, CB/PVDF/[bmim][Tf$_2$N] and CB/PVDF/[bmim][I] electrode fabricated from sc-CO$_2$ fluid. Pure O$_2$ was used as feeding gas. 1.0 M of LiTFSI in TEGDME was used as electrolyte, while current density was 0.075 mAh cm^{-2}.
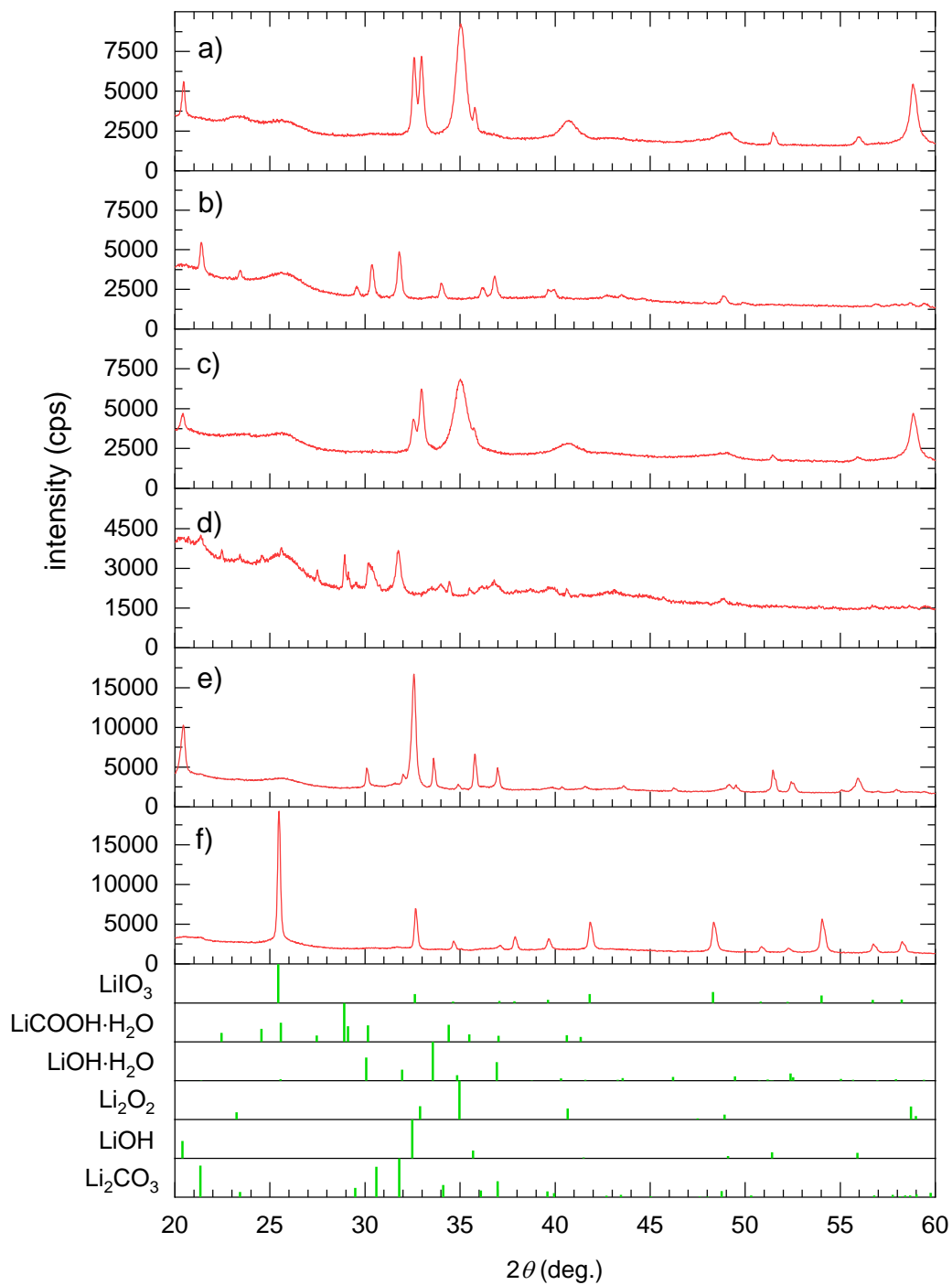
Figure 5.10 X-ray diffraction analysis of a) CB/PVDF electrode after full discharge, b) CB/PVDF electrode after full charge after charge, c) CB/PVDF/[bmim][Tf$_2$N] electrode after discharge, d) CB/PVDF/[bmim][Tf$_2$N] electrode after full charge, e) CB/PVDF/[bmim][I] electrode after full discharge and f) CB/PVDF/[bmim][I] electrode after full charge.
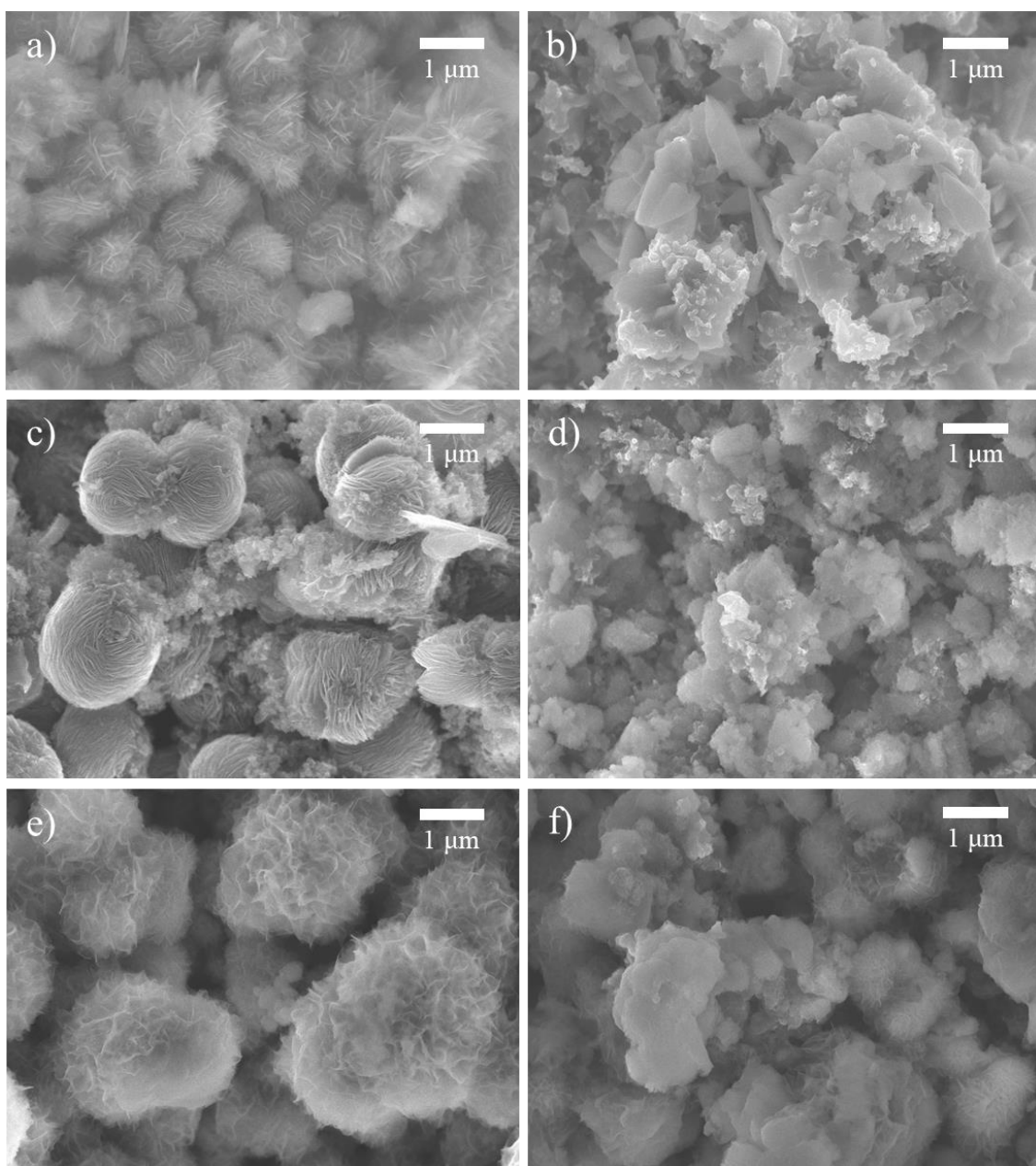
Figure 5.11 Scanning electron microscopy images of a) CB/PVDF electrode after full discharge, b) CB/PVDF electrode after full charge after charge, c) CB/PVDF/[bmim][Tf$_2$N] electrode after discharge, d) CB/PVDF/[bmim][Tf$_2$N] electrode after full charge, e) CB/PVDF/[bmim][I] electrode after full discharge and f) CB/PVDF/[bmim][I] electrode after full charge.

The formation of hydroxide species is considered from several possible routes. The first route is contributed to the association of water from humidity in feeding gas. However, I^- in the IL also performs the catalytic activity to further promote the reaction between water and Li_2O_2 from oxygen reduction, forming hydroxide species at the end of discharge process. The reaction route can be listed as follows [125, 126],

Route 1: $Li_2O_2 + 2H_2O \rightarrow 2LiOH + H_2O_2$ (5.1)

$H_2O_2 + 3I^- + 2Li^+ \rightarrow 2LiOH + I_3^-$ (5.2)

Route 2: $Li_2O_2 + 3H_2O \rightarrow LiOOH \cdot H_2O + LiOH \cdot H_2O$ (5.3)

$LiOOH \cdot H_2O \rightarrow 2LiOH \cdot H_2O + O_2$ (5.4)
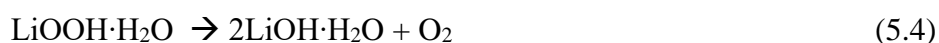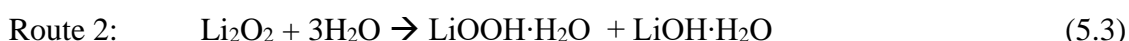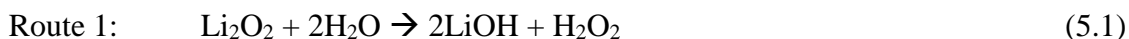
Another possible route for the formation of LiOH during discharge process is contributed to the catalytic activity of iodide ion as electron donor to hydroperoxide produced from decomposition of electrolyte. The electrochemical reactions of this route can be expressed as follows [127, 128],

Route 3: $TEGDME + O_2^- \rightarrow$ radical of $TEGDME + HO_2^-$ (5.5)

$HO_2^- + I^- + Li^+ \rightarrow IO^- + LiOH$ (5.6)

$IO^- + HO_2^- + Li^+ \rightarrow O_2 + I^- + LiOH$ (5.7)
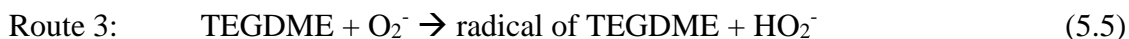
Upon full charging of CB/PVDF/[bmim][I] electrode, the main product was dominated by $LiIO_3$ as seen in Figure 5.10f. This indicated that hydroxide species formed after discharge are reversible. However, hydroxide species transform into lithium iodate instead of complete decomposition. The electrochemical reaction during charging is considered as follows [129],

$2I^- \leftrightarrow 3I_2 + 2e^-$ (redox shuttle reaction)   (5.8)

$3I_2 + 6LiOH \rightarrow LiIO_3 + 5\ LiI + 3H_2O$ (5.9)

$2LiI + 3O_2 \rightarrow 2LiIO_3$ (5.10)

The formation of $LiIO_3$ after charging process is considered as non-reversible since I_2 is consumed and transformed. This leads to the accumulation of $LiIO_3$ after charge reaction.

It can be seen that electrochemical mechanism of electrode with PVDF-[bmim][I] ionogel binder is different from normal electrode without function of redox mediator. To further investigate the possibility of redox mediator-functionalized ionogel binder, cyclic performance of battery was tested by fixing discharge-charge capacity. The cyclic performance test of Li-O$_2$ battery using CB/PVDF, CB/PVDF/[bmim][Tf$_2$N] and CB/PVDF/[bmim][I] electrode fabricated from sc-CO$_2$ fluid are shown in Figure 5.12, while the potential at the cut-off capacity in each cycles are plotted and shown in Figure 5.13. cyclic performance results show that CB/PVDF and CB/PVDF/[bmim][Tf$_2$N] performed stable discharge-charge profile until 16th cycle, while the overpotential was constant as 1.5 V until 15th cycle. Since both electrodes shows the same cyclic performance, non-functionalized ionogel binder as PVDF-[bmim][Tf$_2$N] has no catalytic activity in decomposition of discharge product. On the other hand, CB/PVDF/[bmim][I] provided low overpotential, in which the cut-off charging voltage in the initial cycle was 3.4 V. The suppress of overpotential is dedicated to catalytic activity of iodide ion, which is stated in reaction (5.8). However, cut-off voltage of Li-O$_2$ battery using CB/PVDF/[bmim][I] electrode after charge increased with cycle number. The expansion of charging cut-off voltage is dedicated to the accumulation of LiIO$_3$ after charging process, resulting in the polarization of electrode. Despite the escalation of charging potential, of Li-O$_2$ battery employing CB/PVDF/[bmim][I] electrode provided the best cyclic performance among three batteries for 18 cycles. The cyclic performance of Li-O$_2$ batteries was further investigated by measuring the impedance spectroscopy of batteries after discharge and charge in each cycle. The results of impedance spectroscopy of each batteries are summarized in Figure 5.14. Results of impedance spectroscopy were fitted with equivalent circuit shown in Figure 4.2b. The bulk resistance R_b and charge-transfer resistance R_{ct} of batteries in each cycles derived from curve fitting with equivalent circuit are plotted in Figure 5.15. It can be seen that three batteries provided similar impedance spectroscopy profile prior to the cyclic performance test. As cycle number increased, bulk resistance of all batteries increased. The reduction of bulk resistance is contributed to decomposition of electrolyte, resulting in harder transportation of lithium ion.
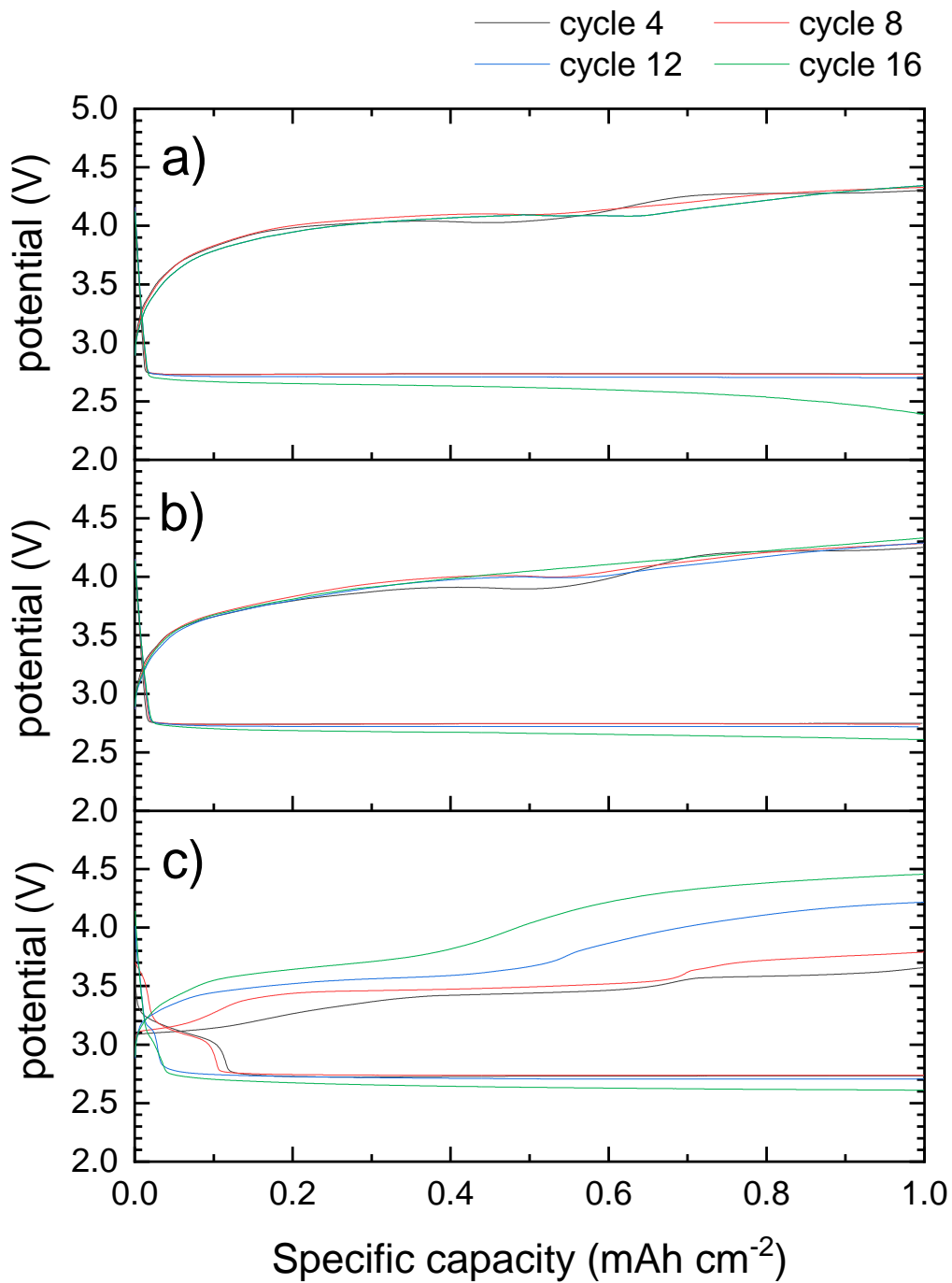
Figure 5.12 Cyclic performance test of Li-O$_2$ battery using a) CB/PVDF electrode, b) CB/PVDF/[bmim][Tf$_2$N] electrode and c) CB/PVDF/[bmim][I] electrode.
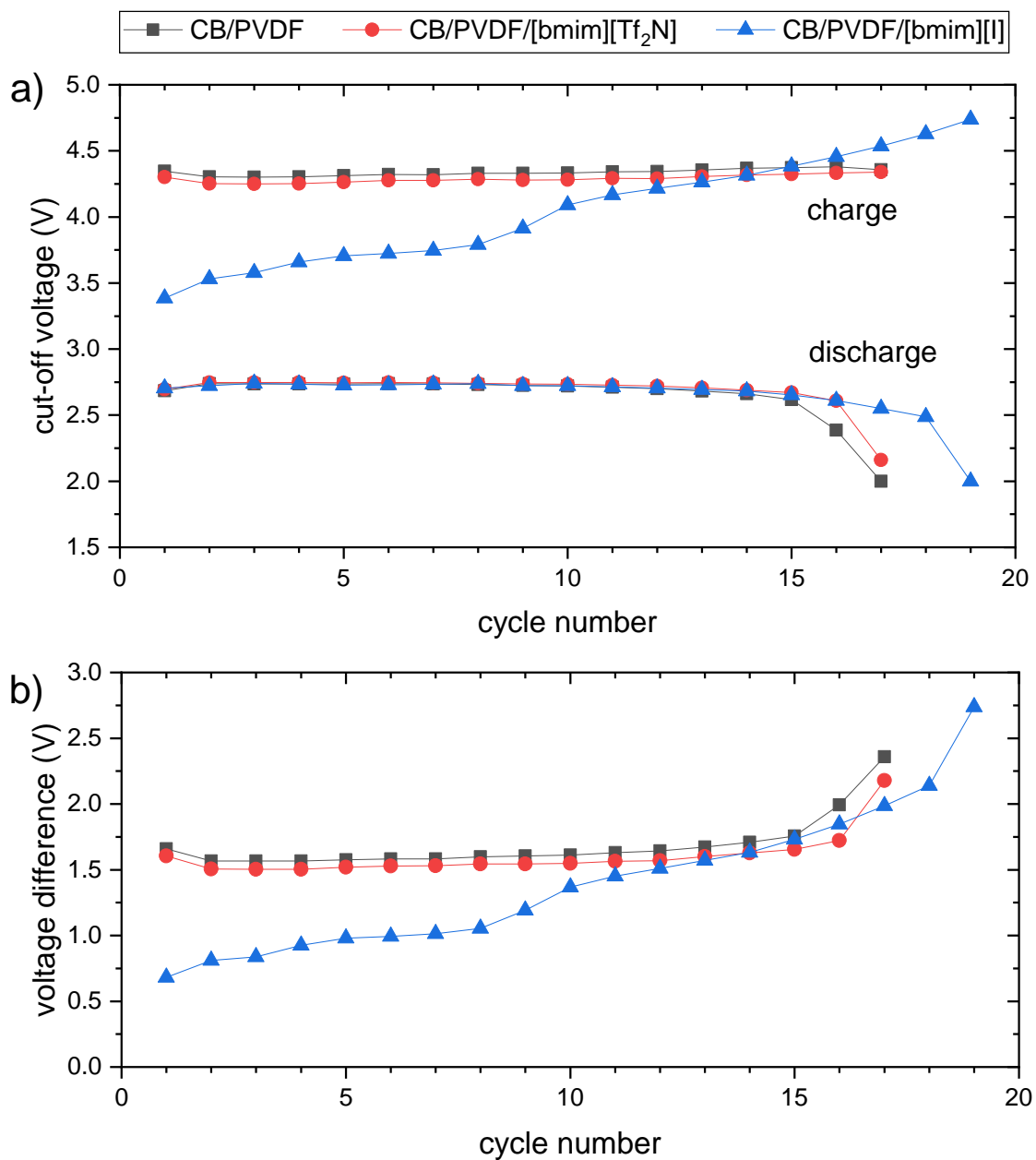
Figure 5.13 Cyclic performance of Li-air batteries; a) potential at the cut-off capacity (1.0 mAh cm^{-2}) after charge (upper line) and discharge (lower line) and b) difference between cut-off voltage of discharge and charge in each cycles.
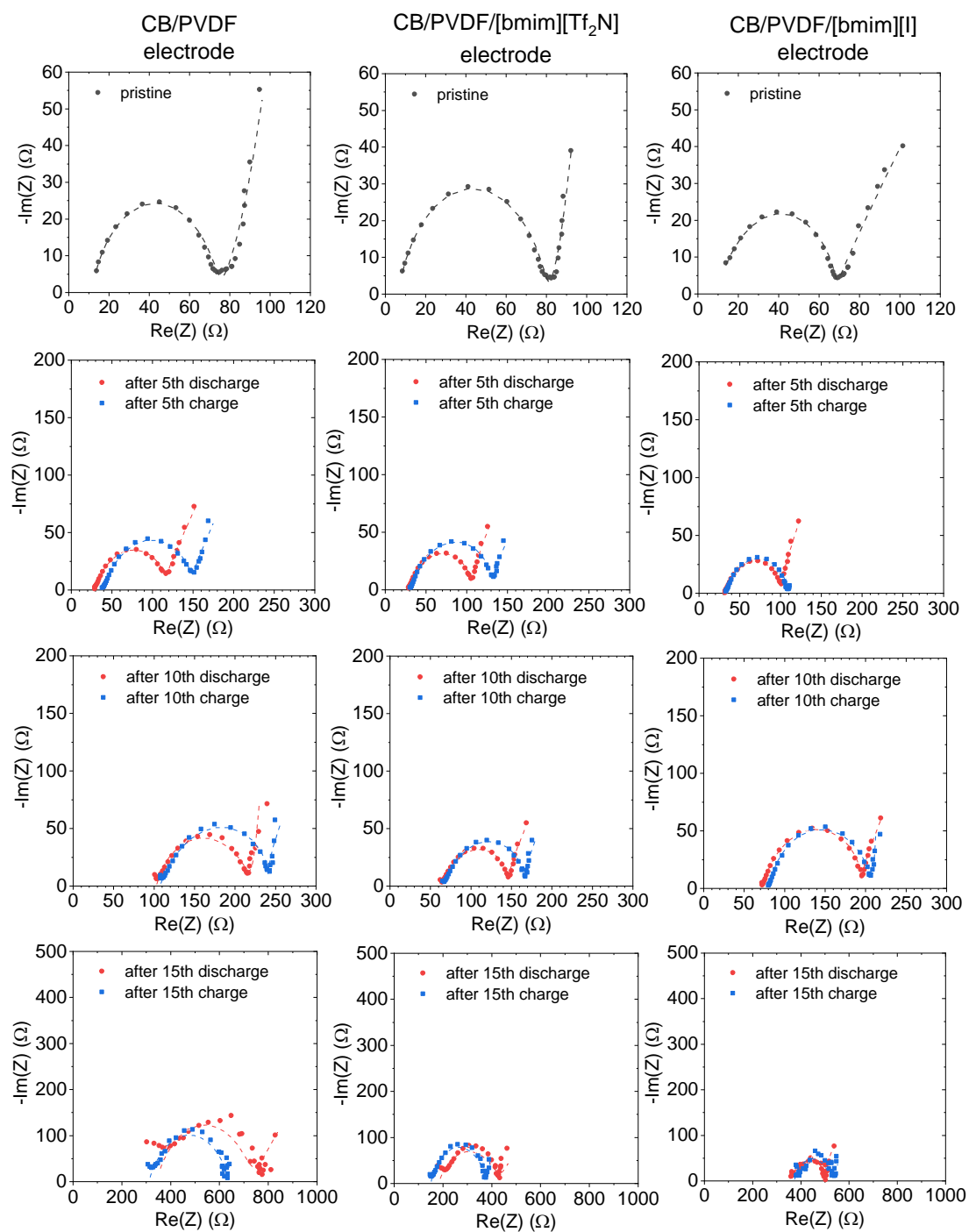
Figure 5.14 Impedance spectroscopy (dot) and curve-fitting results with equivalent circuit (dashed line) of pristine battery, battery in 5th cycle, battery in 10th cycle and battery in 15th cycle.
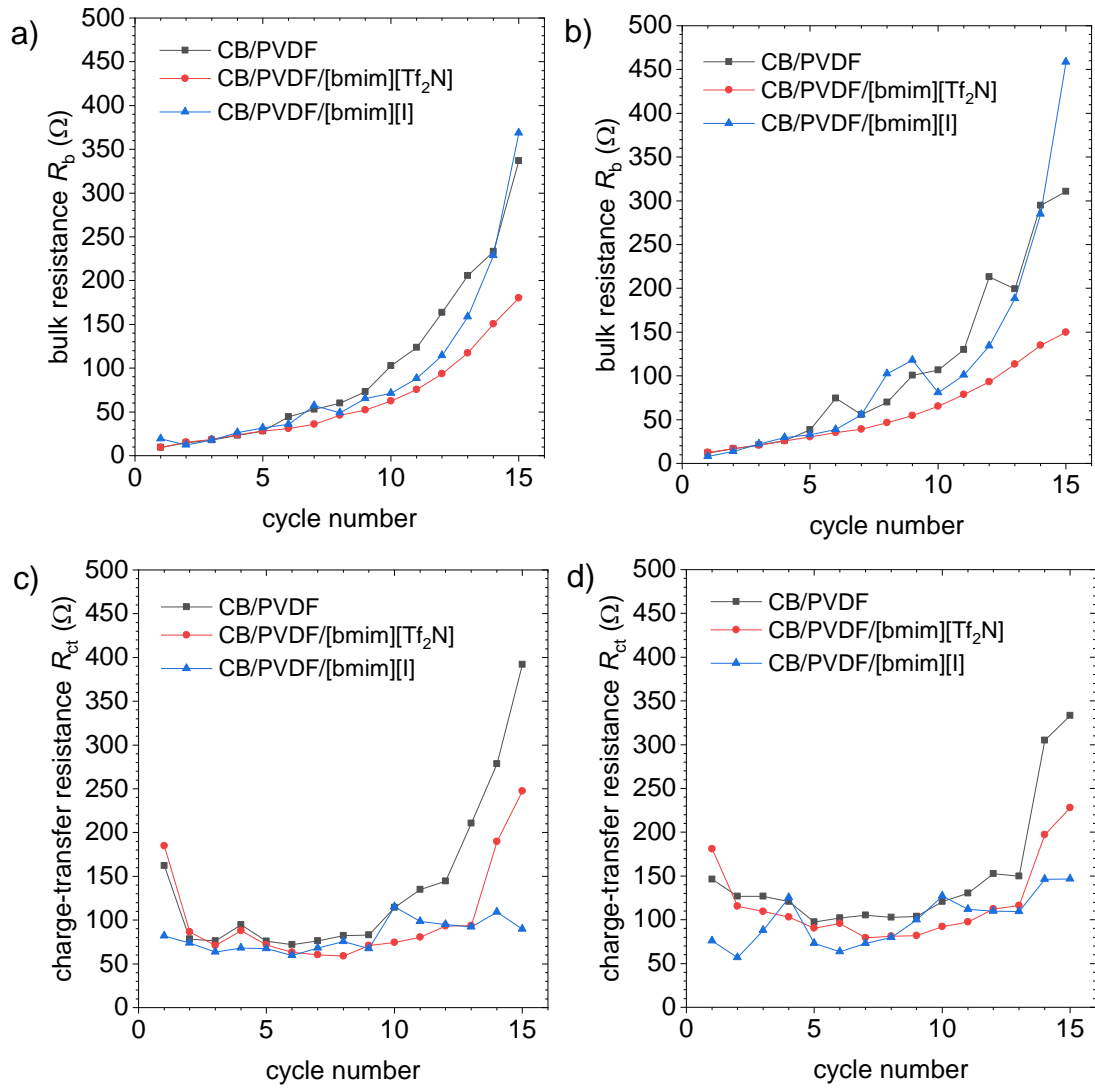
Figure 5.15 Bulk resistance of Li-O₂ battery after a) discharge and b) charge and charge-transfere resistance of Li-O₂ battery after c) discharge and d) charge in each cycle. Resistance values were derived from curve fitting with equivalent circuit.

Although CB/PVDF/[bmim][I] electrode provided the highest bulk resistance in the 15th cycle, charge-transfer resistance of battery using CB/PVDF/[bmim][I] electrode was suppressed below 150 Ω until 15th cycle. On the other hand, charge-transfer resistance of battery with CB/PVDF electrode and CB/PVDF/[bmim][Tf$_2$N] electrode was above 300 Ω and 200 Ω, respectively. This implies that [bmim][I] still performs the redox shuttle reaction regarding to the discharge product decomposition, improving the cyclic performance of Li-O$_2$ battery. Accordingly, suppression of charge-transfer resistance is considered as one of the main keys for development of rechargeable Li-O$_2$ battery.

electrodes in Li-O$_2$ batteries after reaching their limits were investigated to consider the effect of product on battery life. The XRD results of each electrode are summarized in Figure 5.16. The products accumulated in CB/PVDF electrode and CB/PVDF/[bmim][Tf$_2$N] electrode was Li$_2$CO$_3$ and LiCOOH·H$_2$O, while LiIO$_3$ was accumulated in the CB/PVDF/[bmim][I] at the ending of batteries' life. This indicated that Li$_2$CO$_3$ and LiCOOH·H$_2$O generated from decomposition of TEGDME are non-reversible product, which limited the cyclic performance of Li-O$_2$ battery. In term of CB/PVDF/[bmim][I] electrode, LiIO$_3$ is non-reversible product and accumulated after charging process, shortening the life of Li-O$_2$ battery. This result implies that electrolyte and humidity control are the main keys in development of long-life Li-O$_2$ battery. Accordingly, research to develop the stable electrolyte which has ability to withstand the attack by superoxide ion and simultaneously prevent the association of water is indispensable.
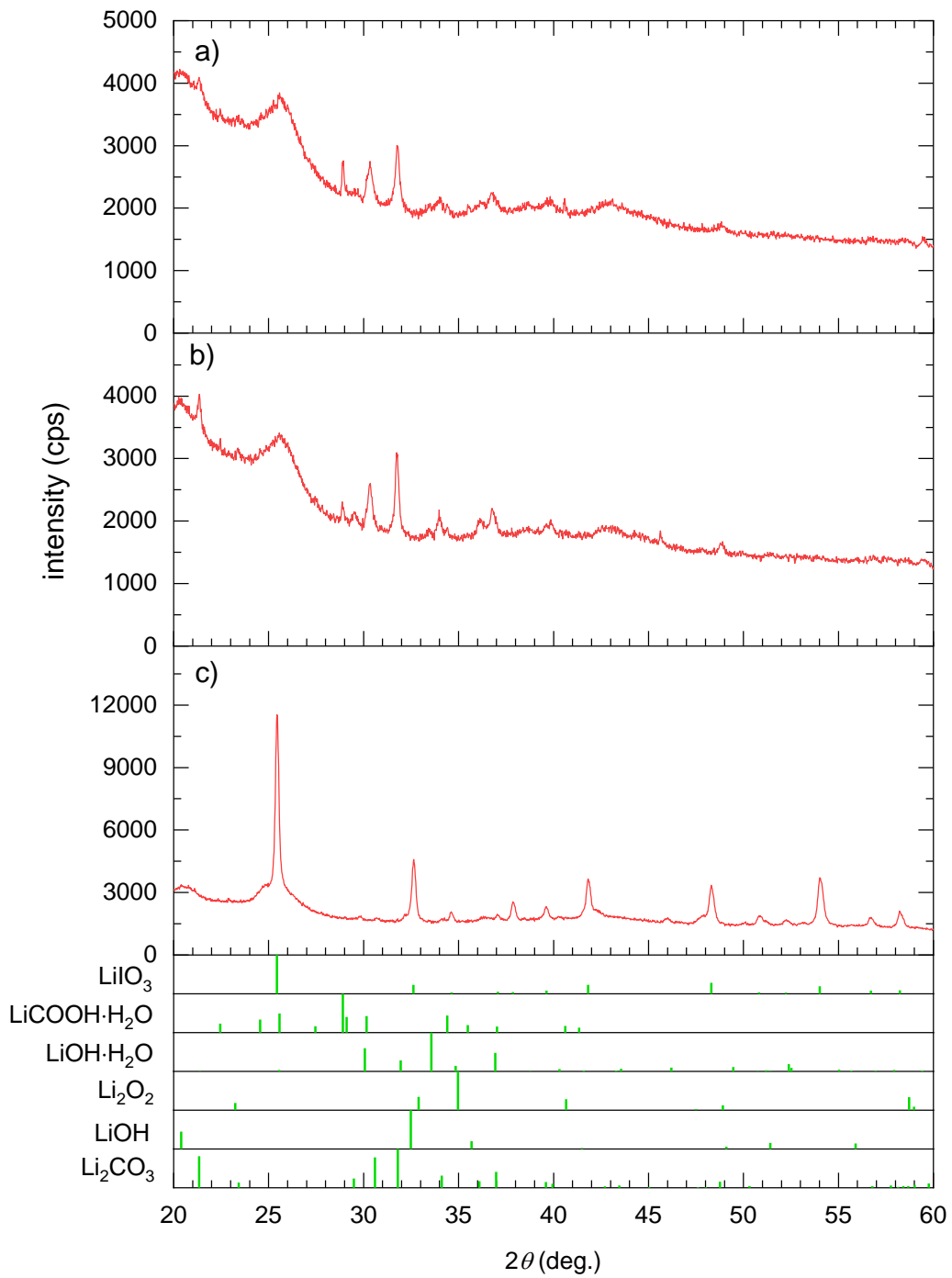
Figure 5.16 X-ray diffraction analysis results of a) CB/PVDF electrode after 17th cycle, b) CB/PVDF/[bmim][Tf$_2$N] electrode after 17th cycle and c) CB/PVDF/[bmim][I] electrode after 19th cycle.

Chapter 6
Conclusion

6.1 Summary of this work

In this doctoral dissertation, the novel method for fabricating of highly porous carbon composite by sc-CO_2 fluid was proposed. The composite was applied as cathode compartment of Li-air battery, leading to the improvement of battery performance.

Chapter 1 states the introduction of this research, including background, objective and literature review. The recent researches on development of Li-air battery on the viewpoint of effect of reaction gases and humidity, cathodic compartment, electrolyte, anode compartment and battery design together with the fabrication of porous materials by sc-CO_2 were reviewed.

Chapter 2 introduces the fundamental study using view chamber observation. The phase behavior of organic compound and polymer dispersed solution, together with carbon particle and polymer dispersed solution were studied. The following points are concluded,

- Homogeneous phase formation time of organic compounds in sc-CO_2 varied and had dependence on type of organic compounds.
- Homogeneous phase formation time can be predicted by viscosity of organic compounds, molecular interaction and mole fraction of CO_2 in system
- PVDF/NMP solution required longer time to form homogeneous phase in sc-CO_2 fluid than pure NMP. Thin film was formed at the end of process.
- Phase behavior of CB/PVDF/NMP solution was observed. Unlike PVDF/NMP solution, the structure was preserved until the end of process. This indicates the high potential of porous composite fabrication using sc-CO_2 fluid.

Chapter 3 presents the fabrication of porous carbon electrode composite composed of carbon black and PVDF by sc-CO_2 fluid. The composite was applied as cathode of Li-air battery. The following points can be concluded,

- CB/PVDF electrode composites fabricated from sc-CO_2 had porosity higher than 90 %, This value is 1.5 folds larger than composites fabricated from evaporation.
- Porosity of carbon composite increased with elevation of sc-CO_2 pressure.

- Capacity of Li-air battery increased as porosity of electrode increased. The optimization of polymer content in carbon electrode is important to improve durability of electrode during discharge reaction of Li-air battery.

Chapter 4 discusses the PVDF-IL ionogel as the binder of carbon electrode, aiming for the development of cathode compartment of Li-O_2/CO_2 battery. The following points are concluded.

- Electrode with ionogel binder provided smaller charge-transfer resistance between electrolyte and surface of electrode due to the improvement of lithium ion transfer in ionogel binder.

- Li-O_2/CO_2 battery composed of electrode with PVDF-IL ionogel binder provided larger discharge capacity than electrode with only PVDF binder.

- Electrode with ionogel binder using IL with higher solubility of O_2 and CO_2 provided larger discharge capacity of Li-O_2/CO_2 battery.

- Ionogel binder improves the ion transfer and reaction gases solubility in binder area, resulting in the enlargement of reaction area.

Chapter 5 discusses the effect of reaction gases on discharge capacity of Li-air batrtery. Moreover, the electrode with ionogel binder with redox mediator function is introduced. the functionalized ionogel binder is developed to improve the cyclic performance of Li-O_2 battery. The following points can be concluded.

- Li-air battery provided high capacity when discharged in presence of following gases: O_2/CO_2 > pure O_2 > air > pure CO_2. The discharge product was Li_2CO_3 after battery was discharge in O_2/CO_2 mixing gases, while both Li_2O_2 and LiOH were formed after discharging in pure O_2 and air. Li-air battery could not be discharge in pure CO_2.

- Battery composed of electrode with PVDF-[bmim][Tf_2N] ionogel binder gave larger discharge capacity than electrode with only PVDF binder when discharge in all presence of reaction gases. Approximately 58 % of discharge efficiency was achieved.

- Electrode with PVDF-[bmim][I] ionogel binder suppressed the charging overpotential, considered as carbon electrode with redox mediator-functionalized ionogel binder.

- Electrode with PVDF-[bmim][I] ionogel binder provided the highest cyclic performance of Li-O_2 battery for 18 cycles, while electrode with PVDF binder and PVDF-[bmim][Tf_2N] binder gave only 16 cycles.

6.2 Future outlook of sc-CO$_2$ for development of Li-air battery

Electrode fabricated from sc-CO$_2$ can provide the following advanteages,

- Electrode composite fabricated by sc-CO$_2$ is free-standing and has porosity higher than 90 %. This reduces the utilization of casting material and decreases the pore cloggage in cathode during discharge.
- The cost of expensive carbon material for cathode compartment can be reduced since cheap also material can also provide high porosity.
- Increase discharge capacity of Li-O$_2$/CO$_2$ battery, providing more energy and reducing greenhouse gas simultaneously.
- Increase cyclability of Li-O$_2$ battery, providing better performance as energy storage.

The advantages of high porosity with low cost of material can benefit the application of primary Li-O$_2$/CO$_2$ battery as energy source and CO$_2$ fixation. Larger energy density could be achieved by better designing of practical battery. This could lead us to the new energy source which uses the greenhouse gas as a fuel to produce energy comparable to energy density of conventional fossil fuel. In term of secondary Li-O$_2$ or Li-air battery, other aspects regarding the stability of electrolyte, dendrite formation in lithium anode and selectivity of reaction gas must be developed apart form cathode compartment to improve cyclability of Li-O$_2$ battery. The development of secondary Li-O$_2$ battery could guid us to the novel energy storage with larger capacity than conventional lithium ion battery. This encourages the replacement of gasoline engine vehicles into electrical vehicle, reducing the carbon dioxide from exhaust gas.

References

1   Paul Albertus, Roel S. Sanchez-Carrera, Timm Lohmann, Boris Kozinsky, Ralf Liedtke, Jasim Ahmed, Aleksandar Kojic, A critical review of Li-air batteries, Journal of the electrochemical society 159 (2012) 1-30.

2   G. Girishkumar, B. McCloskey, A. C. Luntz, S. Swanson, W. Wilcke, Lithium-air battery: Promise and challenges, The Journal of Physical Chemistry Letters (2010) 2193-2203.

3   Xiang Li, Jing Huang, Amir Faghri, A critical review of macroscopic modeling studies on LiO_2 and Li-air batteries using organic electrolyte: Challenges and opportunities, Journal of Power Sources 332 (2016) 420-446.

4   N. Imanishi, A. C. Luntz, P. Bruce. The Lithium air battery: Fundamentals. Springer (2014).

5   Alexander Kraytsberg, Yair Ein-Eli, Review on Li-air batteries-Opportunities, limitations and perspective, Journal of Power Sources 196 (2011) 886-893.

6   C. A. Garcia-Gonzalez, M. C. Camino-Rey, M. Alnaief, C. Zetzl, I. Smirnova, Supercritical drying of aerogels using CO_2: Effect of extraction time on the end material textural properties, Journal of supercritical fluids 66 (2012) 297-306.

7   M. J. Song, I. T. Kim, Y. B. Kim, M. W. Shin, Self-standing, binding-free elctrospun Co3O4/carbon nanofiber composites for non-aqueous Li-air batteries, Electrochimica Acta 182 (2015) 289-296.

8   Andrew I. Cooper, Porous materials and supercritical fluids. Advanced Materials 15 (2003) 1049-1059.

9   E. Reverchon, R. Adami, Nanomaterials and supercritical fluids, J. of supercritical fluids 37 (2006) 1-22.

10 S. Khalloufi, C. Almeida-Rivera, P. Bongers, Supercritical-CO_2 drying of foodstuffs in packed beds: Experimental validation of a mathematical model and sensitive analysis, Journal of Food Engineering 96 (2010) 141-150.

11 G. Laurenczy, P. J. Dyson, Determination of the viscosity of the ILs [bmim][PF_6] and [Bmim][TF_2N] under high CO_2 gas pressure using sapphire NMR Tubes. Zeitschrift für Naturforschung B 63 (2008) 681–684.

12 B. Bonavoglia, G. Storti, M. Morbidelli, Modeling of the sorption and swelling behavior of semicrystalline polymers in supercritical CO_2. Ind. Eng. Chem. Res. 45 (2006) 1183–1200.

13 Binod Kumar, Jitendra Kumar, Robert Leese, Joseph P. Fellner, Stanley J. Rodrigues, K. M. Abraham, A solid-state, rechargeable, long cycle life lithium-air battery, Journal of The Electrochemical Society 157 (2010) A50-A54.

14 X. B. Zhu, T. S. Zhao, Z. H. Wei, P. Tan, L. An, A high-rate and long cycle life solid-state lithium–air battery, Energy and Environmental Science 8 (2015) 3745-3754.

15   K. M. Abraham, Z. Jiang, A polymer electrolyte-based rechargeable lithium/oxygen battery, J. of electrochemical Society 143 (1996) 1-5.

16   D. Capsoni, M. Bini, S. Ferrari, E. Quartarone, P. Mustarelli, Recents advances in the development of Li-air batteries, Journal of Power sources 220 (2012) 253-263.

17   K. Takechi, T. Shiga, T. Asaoka, A Li-O_2/CO_2 battery, Chem. Commun. 47 (2011) 3463-3465.

18   S. Xu, S. K. Das, L. A. Archer, The Li-CO_2 battery: a novel method for CO_2 capture and utilization, RSC advances 3 (2013) 6656-6660.

19   Y. Qiao, J. Yi, S. Wu, Y. Liu, S. Yang, P. He, H. Zhou, Li-CO_2 electrochemistry: a new strategy for CO_2 fixation and energy storage, Joule 1 (2017) 1-12

20   P. Tan, W. Shyy, T. S. Zhao, R. H. Zhang, X. B. Zhu, Effect of moist air on the cycling performance of non-aqueous lithium-air battery, Applied Energy 182 (2016) 569-575.

21   Z. Guo, X. Dong, S. Yuan, Y. Wang, Y. Xia, Humidity effect on electrochemical performance of Li-O_2 batteries, J. of Power Sources 264 (2014) 1-7.

22   S. Yang, P. He, H. Zhou, Research progresses on materials and electrode design towards key challenges of Li-air batteries, Energy Storage Materials 13 (2018) 29-48.

23   X. Yang, P. He, Y. Xia, Preparation of mesocellular carbon foam and its application for lithium/oxygen battery, Electrochemistry Communications 11 (2019) 1127-1130.

24   S. Liu, Z. Wang, C. Yu, Z. Zhao, X. Fan, Z. Ling, J. Qiu, Free-standing, hierarchically porous carbon nanotube film as a binder-free electrode for high-energy Li-O_2 batteries, J. of Materials Chemistry A 1 (2013) 12033-12037.

25   F. Wang, Y. Xu, Z. Luo, Y, Pang, Q. Wu, C. Liang, J. Chen, D. Liu, X. Zhang, A dual pore carbon aerogel based air cathode for a highly rechargeable lithium-air battery, J. of Power Sources 272 (2014) 1061-1071.

26   J. Kang, O. L. Li, N. Saito, Hierarchical meso-macro structure porous carbon black as electrode materials in Li-air battery, J. of Power Sources 261 (2014) 156-161.

27   M. J. Song, I. T. Kim, Y. B. Kim, M. W. Shin, Self-standing, binder-free electroscpun Co_3O_4/carbon nanofiber composites for non-aqueous Li-air batteries, Electrochimica Acta 182 (2015) 289-296.

28   Z. Zhang, Q. Zhang, Y. Chen, J. Bao, X. Zhou, Z. Xie, J. Wei, Z. Zhou, The first introduction of graphene to rechargeable Li-CO_2 batteries, Angewandte Communications 54 (2015) 6550-6553.

29   R. Yu, W. Fan, X. Guo, S. Dong, Highly ordered and ultra-long carbon nanotube arrays as air cathodes for high-energy-efficiency Li-oxygen batteries, J. of Power Sources 306 (2016) 402-407.

30   Y. Li, Y. Huang, Z. Zhang, D. Duan, X. Hao, S. Lui, Preparation and structural evolution of well aligned-carbon nanotube arrays onto conductive carbon-black layer/carbon paper substrate with

enhanced discharge capacity for Li-air batteries, Chemical Engineering Journal 283 (2016) 911-921.

31   J. Jiang, P. He, S. Tong, M. Zheng, Z. Lin, X. Zhang, Y. Shi, H. Zhou, Ruthenium functionalized graphene aerogels with hierarchical and three-dimensional porosity as a free-standing cathode for rechargeable lithium-oxygen batteries, NPG Asia Materials 8 (2018) 239-245.

32   J. Zhang, B. Sun, A. M. McDonagh, Y. Zhao, K. Kretschmer, X. Guo, G. Wang, A multi-functional gel co-polymer bridging liquid electrolyte and solid cathode nanoparticles: An efficient route to Li-O_2 batteries with improved performance, Energy Storage Materials 7 (2017) 1-7.

33   X. Ren, B. Liao, Y. Li, P. Zhang, L. Deng, Y. Gao, Facile synthesis of PdSnCo/nitrogen-doped reduced graphene as a highly active catalyst for lithium-air batteries, Electrochimica Acta 228 (2017) 36-44.

34   H. Kim, H. Lee, M. Kim, Y. Bae, W. Baek, K. Park, S. Park, T. Kim, H. Kwon, W. Choi, K. Kang, S. Kwon, D. Im, Flexible free-standing air electrode with bimodal pore architecture for long cycling Li-O_2 batteries. Carbon 117 (2017) 454-461.

35   X. Lu, G.-P. Hao, X. Sun, S. Kaskel, O. G. Schmidt, Highly dispersed metal and oxide nanoparticles on ultra-polar carbon as efficient cathode materials for Li-O_2 batteries. J. of Materials Chemistry A 5 (2017) 6284-6291.

36   Q. C. Zhu, S. M. Xu, Z.-P. Cai, M. M. Harris, K.-X. Wang, J.-S. Chen, Toward real Li-air batteries: A binder-free cathode with high electrochemical performance in CO_2 and O_2, Energy Storage Materials 7 (2017) 209-215.

37   X. Zhang, C. Wang, H. Li, X.-G.- Wang, Y.-N. Chen, Z. Xie, Z. Zhou, High performance Li-CO_2 batteries with NiO-CNT cathodes, J. of Materials chemistry A 6 (2018) 2792-2796.

38   Z. Zhang, Z. Zhang, P. Lui, Y. Xie, K. Cao, Z. Zhou, Identification of cathode stability in Li-CO_2 batteries with Cu nanoparticles highly dispersed on N-doped graphene, J. of Materials Chemistry A 6 (2018) 3218-3223.

39   Y. Lui, W. Y. Lyu, H. Li, L. Chen, Rechargeable Li-CO_2-O_2 (2:1) battery and Li/CO_2 battery, Energy and Environmental Science 7 (2014) 677-681.

40   J. K. Papp, J. D. Forster, C. M. Burke, H. W. Kim, A. C. Luntz, R. M. Shelby, J. J. Urban, B. D. McCloskey, Poly(vinylidene fluoride) (PVDF) binder degradation in Li-O_2 batteries: a consideration for the characterization of lithium superoxide, J. of Physical Chemistry Letters 8 (2017) 1169-1174.

41   Qi Li, Juner Chen, Lei Fan, Xueqian Kong, Yingying Lu, Progress in electrolytes for rechargeable Li-based batteries and beyond, Green Energy and Environment 1 (2016) 18-42.

42   Jinqiang Zhang, Bing Sun, Xiuquiang Xie, Katja Kretschmer, Guoxiu Wang, Enhancement of stability for lithium oxygen batteries by employing electrolytes gelled by Poly(vinylidene

fluoride-co-hexafluoropropylene) and tetraethylene glycol dimethyl ether, Electrochemica Acta 183 (2015) 56-62.

43 Hyung-Kyu Lim, Hee-Dae Lim, Kyu-Young Park, Dong-Hwa Seo, Hyeojo Gwon, Jihyun Hong, William A. Goddard, Hyungjun Kim, Kisuk Kang, Toward a lithium "air" battery: the effect of CO_2 on the chemistry of a lithium-oxygen cell, Journal of the American Chemical Society 135 (2013) 9733-9742.

44 Mahbuba Ara, Tiejun Meng, Gholam-Abbas Nazri, Steven O. Salley and K.Y. Simon Ng, Ternary imidazolium-pyrrolidinium-based IL electrolytes for rechargeable $Li-O_2$ batteries, Journal of the Electrochemical Society 161 (2014) A1-A7.

45 D. S. Kim, Y. J. Park, Effect of multi-catalysts on rechargeable Li-air batteries, Journal of Alloys and Compounds 591 (2014) 164-169.

46 Z. Liang, Y.-C. Lu, Critical role of redox mediator in suppressing charging instabilities of lithium-oxygen batteries, J. Am. Chem. Soc. 138 (2016) 7574-7583.

47 Y. Chen, S. A. Freunberger, Z. Peng, O. Fontaine, P. G. Bruce, Charging a $Li-O_2$ battery using a redox mediator, Nature chemistry 5 (2013) 489-494.

48 D. Kundu, R. Black, B. Adams, L.F. Nazar, A Highly Active Low Voltage Redox Mediator for Enhanced Rechargeability of Lithium − Oxygen Batteries, ACS Cent. Sci. 1 (2015) 510-515.

49 B.J. Bergner, A. Schu, K. Peppler, A. Garsuch, J. Janek, TEMPO: A Mobile Catalyst for Rechargeable $Li-O_2$ Batteries, J. Am. Chem. Soc. 136 (2014) 15054–15064.

50 N. Feng, X. Mu, X. Zhang, P. He, H. Zhou, Intensive Study on the Catalytical Behavior of N-Methylphenothiazine as a Soluble Mediator to Oxidize the Li_2O_2 Cathode of the $Li-O_2$ Battery, ACS Appl. Mater. Interfaces. 9 (2017) 3733–3739.

51 D. Sun, Y. Shen, W. Zhang, L. Yu, Z. Yi, W. Yin, D. Wang, Y. Huang, J. Wang, D. Wang, J.B. Goodenough, A Solution-Phase Bifunctional Catalyst for Lithium − Oxygen Batteries, J. Am. Chem. Soc. 136 (2014) 8941–8946.

52 Y.G. Zhu, X. Wang, C. Jia, J. Yang, Q. Wang, Redox-Mediated ORR and OER Reactions: Redox Flow Lithium Oxygen Batteries Enabled with a Pair of Soluble Redox Catalysts, ACS Catal. 6 (2016) 6191–6197.

53 J. Zhang, B. Sun, Y. Zhao, A. Tkacheva, Z. Liu, K. Yan, X. Guo, A.M. Mcdonagh, D. Shanmukaraj, C. Wang, M. Armand, Z. Peng, G. Wang, batteries, Nat. Commun. 10 (2019) 1–10.

54 Wu Xu, Jiulin Wang, Fei Ding, Xilin Chen, Eduard Nasybulin, Yaohui Zhang, Ji-Guang Zhang, Environmental Science, Energy Environ. Sci. 7 (2014) 513–537.

55 H. Lee, D.J. Lee, J.N. Lee, J. Song, Y. Lee, M.H. Ryou, J.K. Park, Y.M. Lee, Chemical aspect of oxygen dissolved in a dimethyl sulfoxide-based electrolyte on lithium metal, Electrochim. Acta. 123 (2014) 419–425.

56   R.S. Assary, J. Lu, P. Du, X. Luo, X. Zhang, Y. Ren, The Effect of Oxygen Crossover on the Anode of a Li–O$_2$ Battery using an Ether-Based Solvent: Insights from Experimental and Computational Studies, Chemsuschem Commun. (2013) 51–55.

57   J. Hassoun, H. Jung, D. Lee, J. Park, K. Amine, Y. Sun, B. Scrosati, A Metal-Free, Lithium-Ion Oxygen Battery: A Step Forward to Safety in Lithium-Air Batteries, Nano Lett. 12 (2012) 5775–5779.

58   S. Wu, K. Zhu, J. Tang, K. Liao, S. Bai, J. Yi, Y. Yamauchi, M. Ishida, H. Zhou, Environmental Science on commercial silicon particles as the anode †, Energy Environ. Sci. 9 (2016) 3262–3271.

59   H. Deng, F. Qiu, X. Li, H. Qin, S. Zhao, P. He, H. Zhou, Electrochemistry Communications A Li-ion oxygen battery with Li-Si alloy anode prepared by a mechanical method, Electrochem. Commun. 78 (2017) 11–15.

60   D. Jin, H. Lee, J. Song, M. Ryou, Y. Min, H. Kim, J. Park, Electrochemistry Communications Composite protective layer for Li metal anode in high-performance lithium – oxygen batteries, Electrochem. Commun. 40 (2014) 45–48.

61   X. Zhang, Q. Zhang, X.G. Wang, C. Wang, Y.N. Chen, Z. Xie, Z. Zhou, An Extremely Simple Method for Protecting Lithium Anodes in Li-O$_2$ Batteries, Angew. Chemie - Int. Ed. 57 (2018) 12814–12818.

62   J.O. Park, M. Kim, J.H. Kim, K.H. Choi, H.C. Lee, W. Choi, S.B. Ma, D. Im, A 1000 Wh kg^{-1} Li–Air battery: Cell design and performance, J. Power Sources. 419 (2019) 112–118.

63   X. Li, J. Huang, A. Faghri, A critical review of macroscopic modeling studies on Li O$_2$ and Li–air batteries using organic electrolyte: Challenges and opportunities, J. Power Sources. 332 (2016) 420–446.

64   P. Tan, W. Kong, Z. Shao, M. Liu, M. Ni, Advances in modeling and simulation of Li–air batteries, Prog. Energy Combust. Sci. 62 (2017) 155–189.

65   A. V Sergeev, A. V Chertovich, D.M. Itkis, Modeling of the lithium-air battery cathodes with broad pore size distribution, Chem. Phys. Lett. 660 (2016) 149–154.

66   P. Tan, W. Shyy, T. Zhao, What is the ideal distribution of electrolyte inside cathode pores of non-aqueous lithium–air batteries?, Sci. Bull. 60 (2015) 975–976.

67   G. Gwak, H. Ju, Three-dimensional transient modeling of a non-aqueous electrolyte lithium-air battery, Electrochim. Acta. 201 (2016) 395–409.

68   X. Zhang, S. Heinonen, E. Levänen, Applications of supercritical carbon dioxide in materials processing and synthesis, RSC Adv. 4 (2014) 61137–61152.

69   R.P.F.F. da Silva, T.A.P. Rocha-Santos, A.C. Duarte, Supercritical fluid extraction of bioactive compounds, TrAC - Trends Anal. Chem. 76 (2016) 40–51.

70   I. De Marco, S. Riemma, R. Iannone, Supercritical carbon dioxide decaffeination process: A Life Cycle Assessment study, Chem. Eng. Trans. 57 (2017) 1699–1704.

71   M. Yousefi, M. Rahimi-Nasrabadi, S.M. Pourmortazavi, M. Wysokowski, T. Jesionowski, H. Ehrlich, S. Mirsadeghi, Supercritical fluid extraction of essential oils, TrAC - Trends Anal. Chem. 118 (2019) 182–193.

72   X. Ding, Q. Liu, X. Hou, T. Fang, Supercritical Fluid Extraction of Metal Chelate: A Review, Crit. Rev. Anal. Chem. 47 (2017) 99–118.

73   E. Reverchon, R. Adami, Nanomaterials and supercritical fluids, J. Supercrit. Fluids. 37 (2006) 1–22.

74   C.A. García-González, M.C. Camino-Rey, M. Alnaief, C. Zetzl, I. Smirnova, Supercritical drying of aerogels using CO_2: Effect of extraction time on the end material textural properties, J. Supercrit. Fluids. 66 (2012) 297–306.

75   M. Kinoshita, Y. Shimoyama, Photocatalytic activity of mixed-phase titanium oxide synthesized by supercritical sol-gel reaction, J. Supercrit. Fluids. 138 (2018) 29–35.

76   H.Y. Tian, C.E. Buckley, M. Paskevicius, S.B. Wang, Carbon aerogels from acetic acid catalysed resorcinol-furfural using supercritical drying for hydrogen storage, J. Supercrit. Fluids. 55 (2011) 1115–1117.

77   M.J. Bradshaw, S. Bhattacharyya, N. Venna, J.F. Cahill, Neurologic Manifestations of Systemic Rheumatologic Diseases, Curr. Clin. Neurol. (2020) 321–342.

78   M. Villegas, A.L. Oliveira, R.C. Bazito, P. Vidinha, Development of an integrated one-pot process for the production and impregnation of starch aerogels in supercritical carbon dioxide, J. Supercrit. Fluids. 154 (2019) 104592.

79   C. Darpentigny, G. Nonglaton, J. Bras, B. Jean, Highly Absorbent Cellulose Nanofibrils Aerogels Prepared by Supercritical Drying Cl´ementine, Sensors Actuators B. Chem. 229 (2019) 127065.

80   P. Franco, E. Pessolano, R. Belvedere, A. Petrella, I. De Marco, Supercritical impregnation of mesoglycan into calcium alginate aerogel for wound healing, J. Supercrit. Fluids. 157 (2020) 104711.

81   Cooper, Porous Materials and Supercritical Fluids, Adv. Mater. 15 (2003) 1049–1059.

82   A.I. Cooper, Polymer synthesis and processing using supercritical carbon dioxide, J. Mater. Chem. 10 (2000) 207–234.

83   H.H. Winter, G. Gappert, H. Ito, Rigid pore structure from highly swollen polymer gels, Macromolecules. 35 (2002) 3325–3327.

84   H. Matsuyama, H. Yano, T. Maki, M. Teramoto, K. Mishima, K. Matsuyama, Formation of porous flat membrane by phase separation with supercritical CO2, J. Memb. Sci. 194 (2001) 157–163.

85　R. Rajasingam, L. Lioe, Q.T. Pham, F.P. Lucien, Solubility of carbon dioxide in dimethylsulfoxide and N-methyl-2-pyrrolidone at elevated pressure, J. Supercrit. Fluids. 31 (2004) 227–234.

86　M.R. Bohloul, A. Vatani, S.M. Peyghambarzadeh, Experimental and theoretical study of CO2 solubility in N-methyl-2-pyrrolidone (NMP), Fluid Phase Equilib. 365 (2014) 106–111.

87　M.J. Lazzaroni, D. Bush, J.S. Brown, C.A. Eckert, High-pressure vapor-liquid equilbria of some carbon dioxide + organic binary systems, J. Chem. Eng. Data. 50 (2005) 60–65.

88　L.M. Sanz-Moral, M. Rueda, R. Mato, Á. Martín, View cell investigation of silica aerogels during supercritical drying: Analysis of size variation and mass transfer mechanisms, J. Supercrit. Fluids. 92 (2014) 24–30.

89　J. Sakabe, H. Uchida, Y. Shimoyama, Modeling of drug solubility in supercritical carbon dioxide using equation of state based on hole theory with molecular surface charge density, Chem. Eng. Res. Des. 92 (2014) 2970-2976.

90　Shiang-Tai Lin and Stanley I. Sandler, A priori phase equilibrium prediction from a segment contribution solvation model, Ind. Eng. Chem. Res. 41 (2002) 899-913.

91　J. R. Langan, G.A. Salmon, Physical properties of N-methylpyrrolidinone as funcsions of temperature, Journal of Chemical and Engineering data 32 (1987) 422-425.

92　P. S. Nikam, L. N. Shirsat, M. Hasan, Density and viscosity studies of binary mixtures of acetonitrile with methanol, ethanol, propan-1-ol, propan-2-ol, butan-1-ol, 2-methylpropan-1-ol, and 2-methylpropan-2-ol at (298.15, 303.15, 308.15 and 313.15) K, J. Chem. Eng. Data 43 (1998) 732-737.

93　I. S. Khattab, F. Bandarkar, M. A. A. Fakhree, A. Jouyban, Density, viscosity and surface tension of water+ethanol mixtures from 193 to 323 K, Korean J. Chem. Eng. 29 (2012) 812-817.

94　M. K. Patwari, R. K. Bachu, S. Boodida, S. Nallani, Densities, Viscosities, and Speeds of Sound of Binary Liquid Mixtures of Sulfolane with Ethyl Acetate, n-Propyl Acetate, and n-Butyl Acetate at Temperature of (303.15, 308.15, and 313.15) K, J. Chem. Eng. Data 54 (2009) 1069-1072.

95　L. P. Yang, T. L. Luo, H. L. Lian, G. J. Liu, Density and Viscosity of (2,2-Dichloro-N,N-di-2-propenylacetamide + Acetone) and (2,2-Dichloro-N,N-di-2-propenylacetamide + Ethanol) at T = (278.15 to 313.15) K, J. Chem. Eng. Data 55 (2010) 1364-1367.

96　M. J. Davila, A. Cabanas, C. Pando, Excess molar enthalpies for binary mixtures related to supercritical antisolvent precipitation: Carbon dioxide + N-methyl-2-pyrrolidone, J. Supercrit. Fluids. 42 (2007) 172-179.

97　F. M. Smits, measurement of sheet resistivities with the four-point probe, The Bell System Technical Journal (1957), 711-718.

98   Y.J. Kim, C.H. Ahn, M.B. Lee, M.S. Choi, Characteristics of electrospun PVDF/SiO2 composite nanofiber membranes as polymer electrolyte, Mater. Chem. Phys. 127 (2011) 137–142.

99   P. K. Mahato, A. Seal, S. Garain and S. Sen, Effect of fabrication technique on the crystalline phase and electrical properties of PVDF films, Materials Science-Poland 33 (2015) 157–162.

100   S. Wolff, S. Beuermann, M. Turk, Impact of rapid expansion of supercritical solution process conditions on the crystallinity of poly(vinylidene fluoride) nanoparticles, The Journal of Supercritical Fluids 117 (2016) 18-25.

101   L. Li, Mingqiu Zhang, Rong, Wenhong Ruan, Studies on the transformation process of PVDF from α to β phase by stretching, RSC Adv. 4 (2014) 3938–3943.

102   B. Bonavoglia, G. Storti, M. Morbidelli, Modeling of the sorption and swelling behavior of semicrystalline polymers in supercritical CO_2, Ind. Eng. Chem. Res. 45 (2006) 1183–1200.

103   S. Doroudiani, C.B. Park, M.T. Kortschot, Effect of the crystallinity and morphology on the microcellular foam structure of semi-crystallines polymer, Polym. Eng. Sci. 36 (1996) 2645–2662.

104   S. Martial, F. Jacques, C. Audrey, N. Clemence, R. Elisabeth, New challenges in polymer foaming: a review of extrusion processes assisted by supercritical carbon dioxide, Prog. Polym. Sci. 36 (2011) 740–766.

105   S. Huang, G. Wu, S. Chen, Preparation of microporous poly(vinylidene fluoride) membranes via phase inversion in supercritical CO_2, J. Membr. Sci. 293 (2007) 100–110.

106   J. S. Chiou, J.W. Barlow, D.R. Paul, Polymer crystallization induced by sorption of CO2 gas, J. Appl. Polym. Sci. 30 (1985) 3911–3924.

107   Y. Shimoyama, A. Ito, Predictions of cation and anion effects on solubilities, selectivities and permeabilities for CO_2 in IL using COSMO based activity coefficient model, Fluid Phase Equilibria 297 (2010) 178-182.

108   J. Jacquemin, P. Husson, V. Majer, M. F. C. Gomes, Low-pressure solubilities and thermodynamics of solvation of eight gases in 1-butyl-3-methylimidazolium hexafluorophosphate, Fluid Phase Equilibria 240 (2006) 87-95.

109   A. Staverman, The entropy of high polymer solutions.Generalization of formula, Rec. Trav. Chim. 69 (1950) 163–174.

110   E.A. Guggenheim, R.H. Fowler, Statistical thermodynamics of mixtures with zero energies of mixing, Proc. R. Soc. London Ser. A:Math. Phys. Sci. 183 (1944) 203–212.

111   Shalu, S. K. Chaurasia, R. K. Singh, S. Chandra, Thermal stability, complexing behavior, and ionic transport of polymeric gel membranes based on polymer PVdF-HFP and IL, [BMIM][BF4], J. Phys. Chem. B 117 (2013) 897-906.

112   N. Chen, H. Zhang, L. Li, R. Chen, S. Guo, Ionogel Electrolytes for High-Performance Lithium Batteries: A Review, Adv. Energy Mater. 8 (2018) 1702675.

113 N. Ogihara, S. Kawauchi, C. Okuda, Y. Itou, Y. Takeuchi, Y. Ukyo, Theoretical and experimental analysis of porous electrodes for lithium-Ion batteries by electrochemical impedance spectroscopy using a symmetric cell, J. Electrochem. Soc 159 (2012) A1034-A1039.

114 D. Sharon, M. Afri, M. Noked, A. Garsuch, A.A. Frimer, D. Aurbach, Oxidation of dimethyl sulfoxide solutions by electrochemical reduction of oxygen, J. Phys. Chem. Lett. 4 (2013) 3115–3119.

115 H. Lee, D.J. Lee, J.N. Lee, J. Song, Y. Lee, M.H. Ryou, J.K. Park, Y.M. Lee, Chemical aspect of oxygen dissolved in a dimethyl sulfoxide-based electrolyte on lithium metal, Electrochim. Acta. 123 (2014) 419–425.

116 C.J. Allen, S. Mukerjee, E.J. Plichta, M.A. Hendrickson, K.M. Abraham, Oxygen Electrode Rechargeability in an IL for the Li–Air Battery, J. Phys. Chem. Lett. 2 (2011) 2420–2424.

117 M. Christy, A. Arul, A. Zahoor, K.U. Moon, M.Y. Oh, A.M. Stephan, K.S. Nahm, Role of solvents on the oxygen reduction and evolution of rechargeable Li-O_2 battery, J. Power Sources. 342 (2017) 825–835.

118 E. Glueckauf, the composition of atmospheric air, Compendium of Meteorology (1951) 3-10.

119 U. Sahapatsombut, H. Cheng, K. Scott, Modelling of operation of a lithium-air battery with ambient air and oxygen-selective membrane, J. Power Sources. 249 (2014) 418–430.

120 M.M. Ottakam Thotiyl, S.A. Freunberger, Z. Peng, P.G. Bruce, The carbon electrode in nonaqueous Li-O_2 cells, J. Am. Chem. Soc. 135 (2013) 494–500.

121 B.D. McCloskey, A. Speidel, R. Scheffler, D.C. Miller, V. Viswanathan, J.S. Hummelshøj, J.K. Nørskov, A.C. Luntz, Twin problems of interfacial carbonate formation in nonaqueous Li-O_2 batteries, J. Phys. Chem. Lett. 3 (2012) 997–1001.

122 M. Leskes, A.J. Moore, G.R. Goward, C.P. Grey, Monitoring the electrochemical processes in the lithium-air battery by solid state NMR spectroscopy, J. Phys. Chem. C. 117 (2013) 26929–26939.

123 S.A. Freunberger, Y. Chen, N.E. Drewett, L.J. Hardwick, F. Bardé, P.G. Bruce, The lithium-oxygen battery with ether-based electrolytes, Angew. Chemie - Int. Ed. 50 (2011) 8609–8613.

124 B.D. Adams, R. Black, Z. Williams, R. Fernandes, M. Cuisinier, E.J. Berg, P. Novak, G.K. Murphy, L.F. Nazar, Towards a stable organic electrolyte for the lithium oxygen battery, Adv. Energy Mater. 5 (2015) 1–11.

125 C. Change, C. Cycle, S. River, Cycling Li-O2 batteries via LiOH formation and decomposition, Encycl. Soils Environ. 350 (2004) 170–175.

126 M. Tułodziecki, G.M. Leverick, C. V. Amanchukwu, Y. Katayama, D.G. Kwabi, F. Bardé, P.T. Hammond, Y. Shao-Horn, The role of iodide in the formation of lithium hydroxide in lithium-oxygen batteries, Energy Environ. Sci. 10 (2017) 1828–1842.

127 W. Kwak, D. Hirshberg, D. Sharon, H. Shin, M. Afri, J. Park, A. Garsuch, F. Chesneau, A.A. Frimer, Understanding the behavior of Li – oxygen cells containing LiI, J. Mater. Chem. A. (2015) 8855–8864.

128 Y. Qiao, S. Wu, Y. Sun, S. Guo, J. Yi, P. He, H. Zhou, Unraveling the complex role of iodide additives in Li-O_2 batteries, ACS Energy Lett. 2 (2017) 1869–1878.

129 C.M. Burke, R. Black, I.R. Kochetkov, V. Giordani, D. Addison, L.F. Nazar, B.D. Mccloskey, Implications of 4 e$^-$ Oxygen Reduction via Iodide Redox Mediation in Li−O_2 Batteries, ACS Energy Lett. 1 (2016) 747–756.

Abbreviation for chemicals

[bmim][Tf$_2$N]	1-Butyl-3-methylimidazolium bis(trifluoromethylsulfonyl)imide
[bmim][PF$_6$]	1-Butyl-3-methylimidazolium hexafluorophosphate
[bmim][I]	1-Butyl-3-methylimidazolium iodide
NMP	1-Methyl-2-pyrrolidone
BuOH	Butanol
CB	Carbon black
CO$_2$	Carbon dioxide
DMSO	Dimethyl sulfoxide
EtOH	Ethanol
EA	Ethyl acetate
IL	IL
Li	Lithium
Li$_2$CO$_3$	Lithium carbonate
LiCOOH·H$_2$O	Lithium formate monohydrate
LiOH	Lithium hydroxide
LiOH·H$_2$O	Lithium hydroxide monohydrate
LiIO$_3$	Lithium iodate
Li$_2$O$_2$	Lithium peroxide
O$_2$	Oxygen
PVDF	Polyvinylidene fluoride
RM	Redox mediator
sc-CO$_2$	Supercritical carbon dioxide
TEGDME	Tetraethylene glycol dimethyl ether

Nomenclature

a_{eff}	Surface area of standard segment	Å^2
A_i	Surface area of molecule i	Å^2
$A_i(\sigma_m)$	Surface area of charge segment σ_m in molecule i	Å^2
A_{st}	Standard surface area	Å^2
A_{top}	Top area of electrode	cm^2
c_{hb}	constant for interaction of hydrogen bonding	kcal Å^4 mol^{-1} e^{-2}
$E(\sigma_m, \sigma_n)$	Misfit energy	kcal Å^4 mol^{-1} e^{-2}
f_i^{ref}	Fugacity of molecule i in standard state	bar
h_{av}	Average thickness of electrode	cm
$P_i(\sigma_m)$	Molecule surface charge density of segment σ_m in molecule i	
$P_s(\sigma_m)$	Molecule surface charge density of segment σ_m in mixture	
P_{tot}	Total pressure	bar
R	Resistance	Ω
R_b	Bulk resistance	Ω
R_{ct}	Charge-transfer resistance	Ω
s	Length between probe in 4-point probe measurement	cm
t_{initial}	Initial time that pressure reached desired pressure	min
$t_{99.90\%}$	Initial time that normalized mean grayscale is above 99.90%	min
T	Temperature	K
u_{ij}	Molecular interaction energy between molecule i and j	kJ mol^{-1}
u_{11}	Molecular interaction energy between organic compound itself	kJ mol^{-1}
u_{12}	Molecular interaction energy between organic compound and CO_2	kJ mol^{-1}
V_{st}	Standard volume	Å^3
V_{total}	Total volume of electrode	cm^3
V_{void}	Void volume of electrode	cm^3
$w_{\text{solid,liquid}}$	Weight of solid or liquid component in electrode	g
w_T	Weight at temperature T	mg
w_0	Initial weight	mg
$\Delta W(\sigma_m, \sigma_n)$	Exchange energy	kcal Å^2 mol^{-1} e^{-1}
x_i	Mole fraction of component i	
y_{CO2}	Mole fraction of CO_2	
z	Coordination number	

γ_i	Activity coefficient of component i in mixture	
$\Gamma_i^0(\sigma_m)$	Segment activity coefficient of pure component i in segment σ_m	
$\Gamma_s(\sigma_m)$	Segment activity coefficient of mixture in segment σ_m	
ε_0	Permittivity of free space	$e^2 \text{ mol kcal}^{-1} \text{ Å}^{-1}$
μ	Dynamic viscosity	mPa s
$\rho_{\text{solid,liquid}}$	Density of solid or liquid component in electrode	g cm^{-3}
σ_{acc}	Acceptor charge segment	$e \text{ Å}^{-2}$
σ_{don}	Donor charge segment	$e \text{ Å}^{-2}$
σ_{hb}	Cut-off value for hydrogen bonding interaction	$e \text{ Å}^{-2}$
σ_{m}	Charge segment	$e \text{ Å}^{-2}$
τ	Homogeneous phase formation time	min
τ'	Homogeneous phase formation time constant	min

List of figures

List of tables

Acknowledgement